CATALYSIS, INHIBITION, AND SIGNAL TRANSDUCTION BY

MENAQUINOL:FUMARATE OXIDOREDUCTASE

By

Thomas M. Tomasiak

Dissertation

Submitted to the Faculty of the

Graduate School of Vanderbilt University

in partial fulfillment of the requirements for the degree of

DOCTOR OF PHILOSOPHY

in

Pharmacology

May, 2011

Nashville, Tennessee

Approved:

H. Alex Brown

Tina Iverson

Heidi Hamm

Hassane Mchauorab

Jens Meiler

To my parents, Zofia and Janusz, who taught me the courage to follow my life's

ambitions.

ACKNOWLEDGEMENTS

TABLE OF CONTENTS

Chapter

LIST OF TABLES

TABLE OF FIGURES

LIST OF ABBREVIATIONS

QFR – Menaquinol:fumarate oxidoreductase

SQR – Succinate:ubiquinone oxidoreductase

FAD – Flavin adenine dinucleotide

3-NP – 3-nitropropionate

OAA – Oxaloacetate

CT-Charge-transfer

MQ – Menaquinone

UQ – Ubiquinone

UQ-4 - Ubiquinone-4

HQNO – heptyl quinoline n-oxide

DDM = B-dodecyl maltoside

DM = decyl maltoside

CHAPTER I

INTRODUCTION[1]

Respiration

In respiration, organisms catalyze diverse oxidation-reduction reactions, first, to establish a transmembrane electrochemical gradient, and second, to use this energy to form ATP with the ATP synthase (77). Aerobic respiration uses O_2 as the terminal electron acceptor (Fig. 1a) and is the most energy-efficient respiration pathway (108). Anaerobic respiration can use a variety of small inorganic and organic molecules as terminal electron acceptors, although these pathways result in lowered ATP levels for the cell. Compounds utilized include sulfate (13), nitrate (39, 40), nitrite (53), and organic acceptors such as fumarate (Fig. 1b) (113). In *Escherichia coli,* aerobic and anaerobic respiration converge on the chemical interconversion of succinate and fumarate. Anaerobic respiration can use a variety of small inorganic and organic molecules as terminal electron acceptors, although these pathways result in lowered ATP levels for the cell. Compounds utilized

include sulfate (13), nitrate (39, 40), nitrite (53), and organic acceptors such as fumarate (Fig. 1b) (113). In *Escherichia coli,* aerobic and anaerobic respiration converge on the chemical interconversion of succinate and fumarate.

(a)　　Aerobic respiratory chain

succinate →
fumarate

O$_2$ →
H$_2$O

NADH →
NAD$^+$ + H$^+$

4H$^+$

4H$^+$

cytoplasmic

Q ⇌ QH$_2$

QH$_2$ ⇌ Q

periplasmic

4H$^+$

4H$^+$

SQR

Cytochrome *bo*$_3$
ubiquinol oxidase

NADH
dehydrogenase I

(b)　　Anaerobic respiratory chain

glycerol-3-
phosphate →

dihydroxy-
acetone phosphate
+ H$^+$

H$_2$ →
2H$^+$

fumarate →
succinate

cytoplasmic

Q ⇌ QH$_2$

QH$_2$ ⇌ Q

periplasmic

Hydrogenase-2

QFR

Glycerol-3-phosphate
dehydrogenase
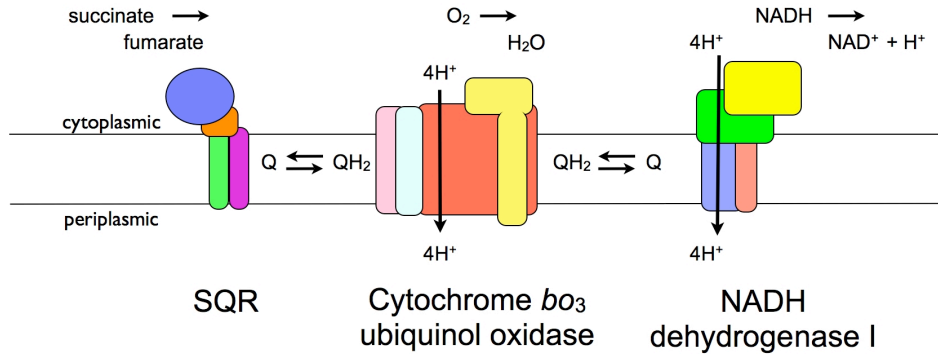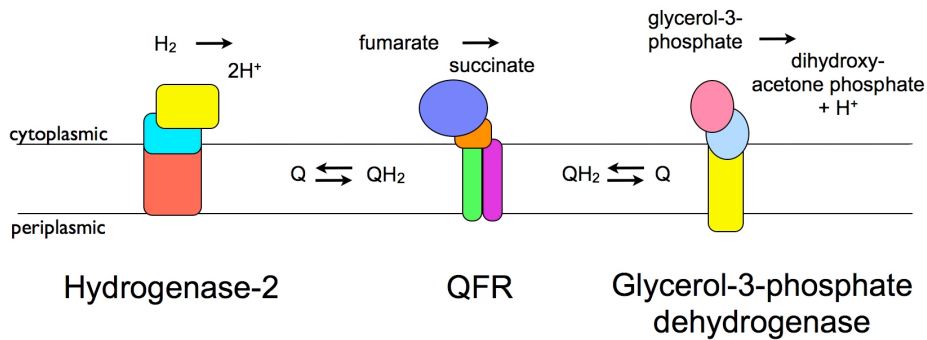
Figure 1. The aerobic and anaerobic respiratory chains. (a) Aerobic respiratory chain. In aerobic respiration, reduced ubiquinol passes electrons from upstream reductases such as SQR and NADH oxidase I (98, 115) to cytochrome *bo*$_3$ oxidase and ultimately to oxygen (1, 18, 91). Cytochrome *bd* oxidase, omitted for clarity, is expressed at levels similar to those of cytochrome *bo*$_3$ oxidase under microaerophilic conditions (30). NDH-I also participates in anaerobic respiration (110). (b) Anaerobic respiratory chain. In anaerobic respiration, reduced menaquinol passes electrons from hydrogenase-2 (73, 97) and anaerobic 3-phosphate dehydrogenase (21, 41) to terminal oxidases such as QFR. Succinate (Fig. 2a) is used as an electron donor during aerobic respiration (by oxidation to fumarate), while fumarate (Fig. 2b) is reduced to succinate during anaerobic respiration as a terminal electron acceptor (35, 108).

(a)   (b)

Succinate   Fumarate
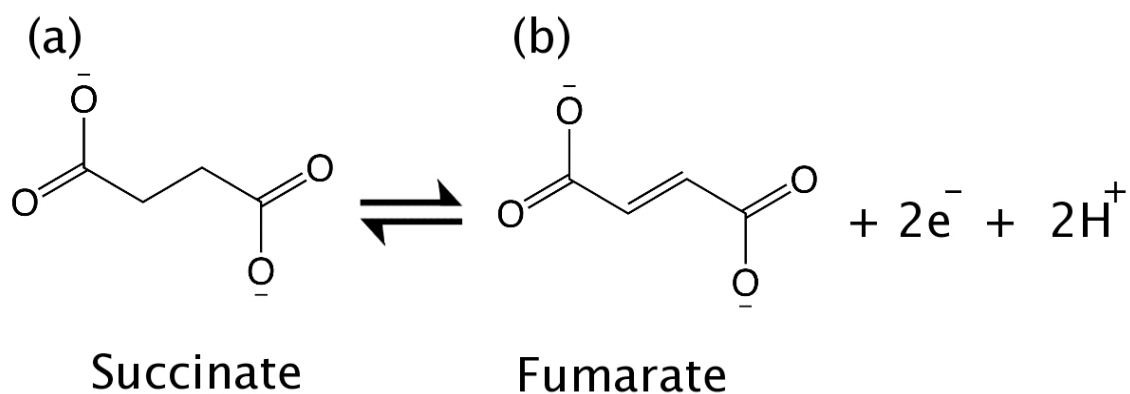
Figure 2. Succinate (a) and fumarate (b). Succinate and fumarate are sterically similar dicarboxylate molecules that are interconverted through a two-proton, two-electron transition.

In *E. coli* the oxido-reduction of fumarate and succinate is linked to a second oxidation-reduction reaction of the membrane-soluble small molecule quinones (Fig. 3). Since quinones are membrane embedded, the respiratory complexes coupling succinate-fumarate interconversion to quinone-quinol interconversion are integral membrane proteins. It was previously demonstrated that two distinct enzymes interconvert fumarate and succinate in *E. coli* (35).
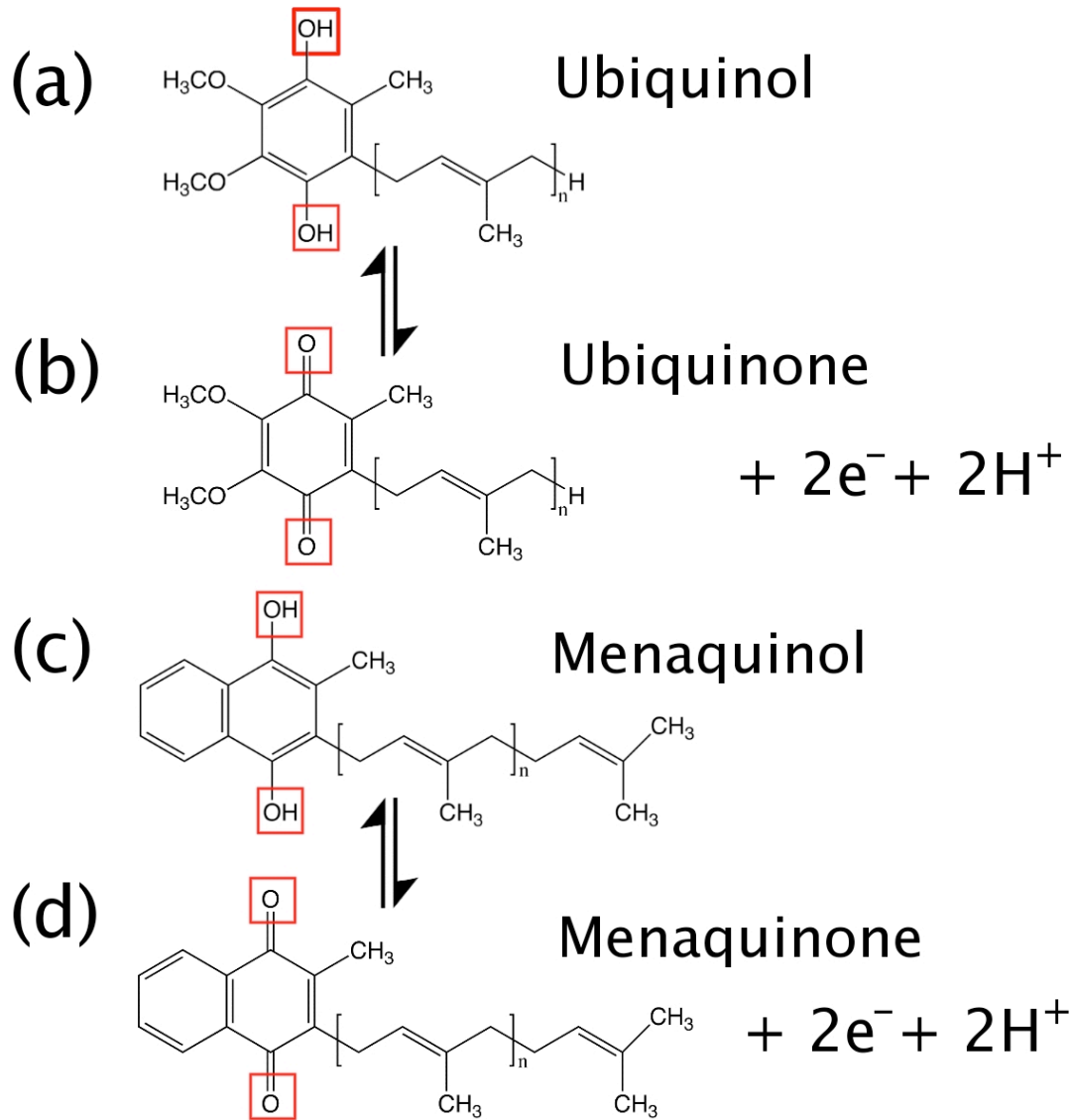
Figure 3. Menaquinol and ubiquinol. Like succinate and fumarate, quinol (a and c) and quinone (b and d) are interconverted with a two-proton, two-electron transition, making the coupling of succinate/fumarate to quinol/quinone energetically well matched. Specifically, interconversion between quinol and quinone occurs at the hydroxyl/carbonyl, highlighted in red. (a and b) Ubiquinol and ubiquinone interconversion. (c and d) Menaquinol and menaquinone interconversion.

Succinate:quinone oxidoreductase (SQR, also termed succinate dehydrogenase or

Complex II in mitochondria) is an essential component of the tricarboxylic acid cycle

in aerobically grown prokaryotic and eukaryotic cells, in which it oxidizes succinate to

fumarate coupled to the reduction of ubiquinone. The enzyme is encoded by the

sdhCDAB operon (Fig. 4). During anaerobic respiration, in many

prokaryotes and lower eukaryotes, the structurally related enzyme quinol:fumarate

reductase (QFR, also termed fumarate reductase) oxidizes menaquinol in the

membrane domain and reduces fumarate to succinate in the cytoplasm. QFR is also

encoded by a compact operon, but the gene order is *frdABCD* (Fig. 4).
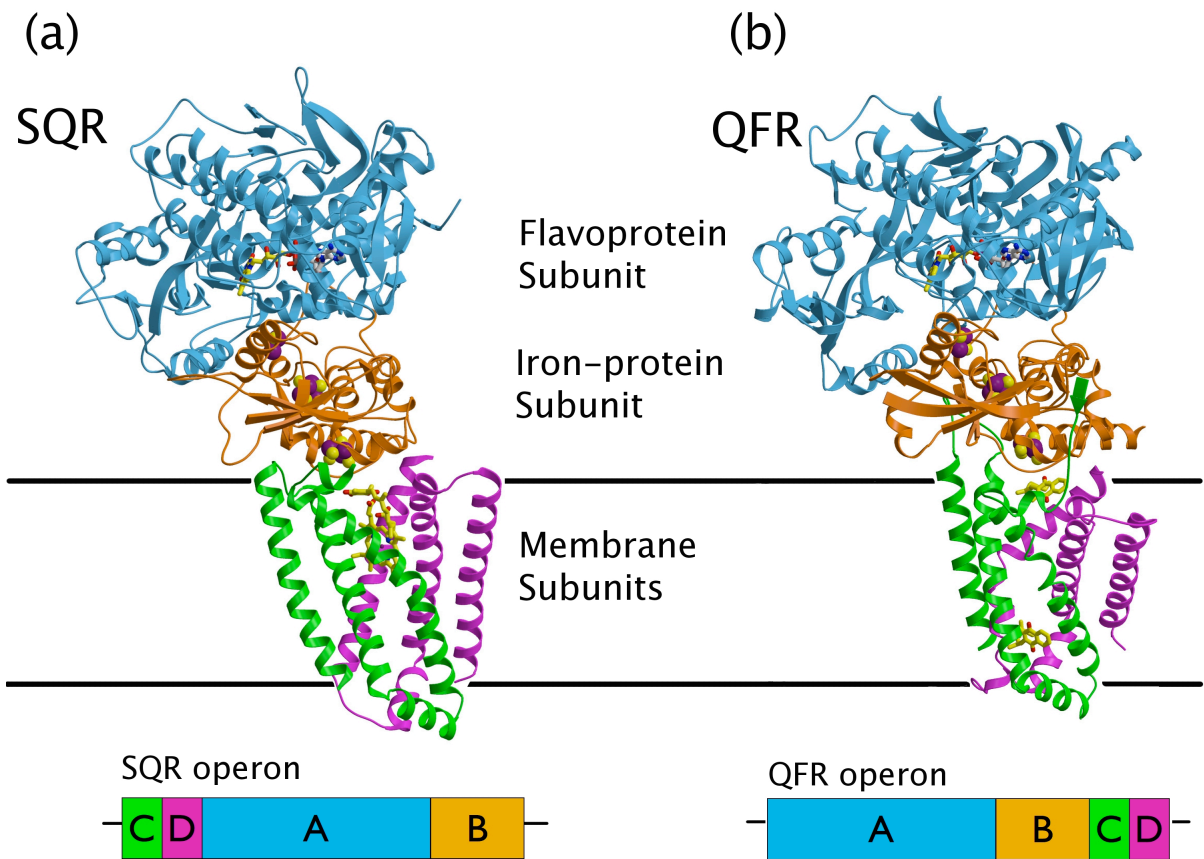
Figure 4. Comparison of SQR and QFR structures. Both SQR (a) and QFR (b) comprise four polypeptide subunits: a flavoprotein subunit (blue: *sdhA*, SQR; *frdA*, QFR), an iron protein subunit (orange: *sdhB*, SQR; *frdB*, QFR), and two transmembrane subunits (green [*sdhC*, SQR; *frdC*, QFR] and purple [*sdhD*, SQR; *frdD*, QFR]). The respective genes of QFR and SQR comprise two distinct operons with different gene order. The genes are shown in the same color scheme as the structures. Standard nomenclature uses the chain name in addition to the residue number in identifying an amino acid.

Respiratory Roles of QFR and SQR

E. coli, as a facultative anaerobe, grows readily in aerobic, microaerophilic, or anaerobic environments. To accomplish this feat, the organism has developed an elaborate mechanism to control expression of metabolic enzymes used in catabolic and anabolic pathways, mainly at the transcriptional level (95, 96, 100). The

7

transcription of both the SQR and QFR respiratory complexes is controlled by the availability of O_2 (42, 49, 61). SQR is highly expressed in the presence of O_2, whereas QFR is expressed under anaerobic or microaerophilic conditions. As a result, the level of one enzyme is usually predominant, depending on growth conditions. SQR levels rise in the presence of oxygen due to deactivation of the repressor ArcB (42) by the oxygen-sensitive kinase ArcA (43) (see chapter 3.2.10). In contrast, the fumarate-nitrate reductase regulator (FNR) controls QFR levels (56) by forming a dimer (61) that activates transcription when oxygen levels fall (see chapters 3.2.10 and 3.4.5).

During aerobic respiration, SQR oxidizes succinate to fumarate (succinate/fumarate couple E_{m7}= +30 mV [32]) and transfers two electrons and two protons to ubiquinone (E_{m7} UQ/UQH$_2$ = +90 mV [84]), reducing it to ubiquinol (UQH$_2$). Both ubiquinone and ubiquinol are freely diffusible within the membrane. After dissociation of UQH$_2$ from SQR, the quinol is transferred to downstream oxidases (12, 91) (see chapter 3.2.5 for more details), where reoxidation of quinol by the cytochrome *bd* or *bo$_3$* quinol oxidases provides input electrons for further downstream reactions. Transmembrane oxido-reduction of quinones is also a general mechanism of generating a transmembrane electrochemical potential (77); however, the oxidation of succinate by SQR does not result in any charge separation across the membrane, and so SQR is not a proton pump and enzyme activity is not affected by membrane potential (Fig. 5). It has been suggested that this is the case in both *E. coli* and mitochondrial SQR because the electron transfer reactions are not sufficiently exergonic to promote proton translocation (102). There are cases of

di-heme SQRs, such as that from *Bacillus subtilis*, which use menaquinone as a substrate and do not undergo endergonic electron transport that responds to the membrane proton or electrochemical potential (99). These di-heme SQRs are found in gram-positive bacteria, are succinate-menaquinone oxidoreductases, and are classified differently than *E. coli* SQR. Their properties have been reviewed elsewhere (32, 57, 65).

(a)

$QH_2 \longrightarrow Q + 2H^+ + 2\bar{e}$

Net 2 H$^+$

$Q + 2H^+ + 2\bar{e} \longrightarrow QH_2$

(b)

succinate $\longrightarrow$ fumarate $+ 2H^+ + 2\bar{e}$

$MQ + 2H^+ + 2e^- \longrightarrow MQH_2$

Net 0 H$^+$

SQR
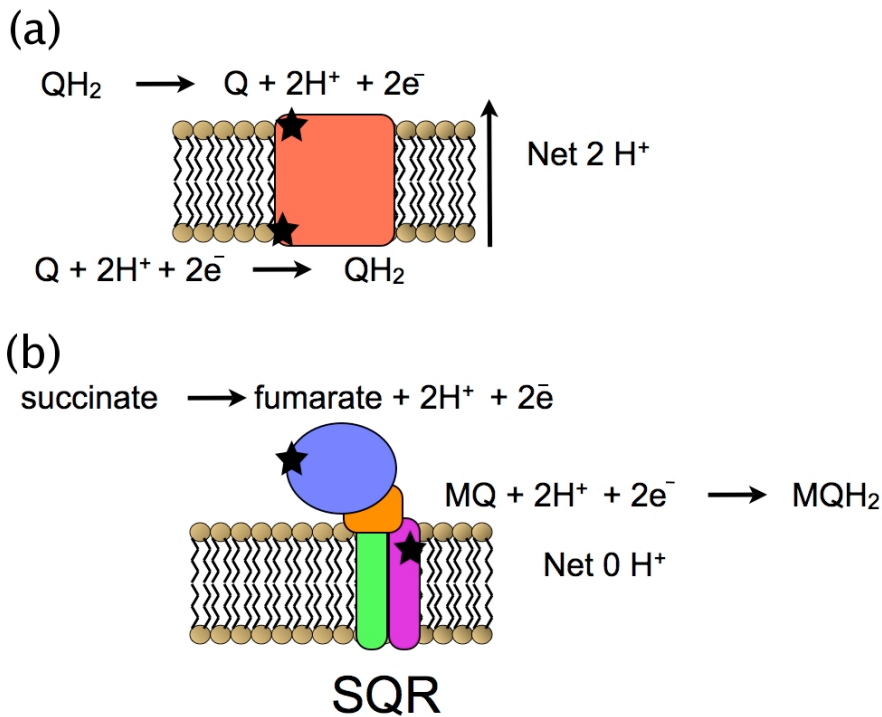
Figure 5. Comparison of Q-cycle-like proton gradient formation and the electro-neutral reactions of SQR. (a) Mitchellian loop and proton gradient formation. Two coupled reactions on opposite sides of the membrane (labeled with stars)—uptake protons on one side of the membrane and release protons on the other. This results in a net separation of two protons and establishment of a proton gradient. (b) Non-Mitchellian loop in SQR. SQR and QFR catalyze two reactions with proton release and uptake on the same side of the membrane, resulting in no net charge displacement.

QFR catalyzes the reverse reaction of SQR, namely, the reduction of fumarate to succinate (succinate/fumarate couple E_{m7} = +30 mV [32]) coupled to menaquinol (E_{m7} MQ/MQH$_2$ = –74 mV) oxidation (108, 113). This reaction is the final step in anaerobic respiration with fumarate. During anaerobic respiration with fumarate, the transmembrane proton gradient is established by respiratory complexes upstream of

QFR, such as formate dehydrogenase (120), hydrogenase (50), and glycerol-3-phosphate dehydrogenase (55, 76) (see chapters 3.2.2 and 3.2.7). The contribution that QFR makes to the transmembrane gradient is thus indirect since it couples the reoxidation of MQH_2 to MQ to fumarate reduction (35, 55). This generates oxidizing equivalents for other respiratory complexes (59). As for *E. coli* SQR, this is most easily explained by the fact that the fumarate reduction site is in the cytoplasm and the menaquinol oxidation site is at the membrane cytoplasmic interface. Thus, protons released by menaquinol oxidation and fumarate reduction balance each other and remain in the cytoplasm and no net proton gradient is produced. The *E. coli* QFR is different in this aspect from di-heme-containing QFRs, such as those from *Wolinella succinogenes*, as discussed in a series of interesting articles from the Lancaster laboratory (55, 57, 65).

Subunit architecture and function

Despite opposite catalytic directions under normal physiological conditions, QFR and SQR have similar molecular weights (20, 22, 24, 63, 119) and architecture (44, 121), contain nearly identical sets of cofactors, can catalyze succinate-fumarate interconversion bi-directionally in vitro (Table 1), and can functionally replace one another in vivo (31, 66). SQR and QFR contain four nonidentical subunits, and the enzymes can be divided into hydrophilic and hydrophobic domains (Fig. 4). The hydrophilic subunits A and B of both enzymes are sufficient for the succino-oxidase/ fumarate reductase activities of the enzymes with artificial electron acceptors. These

11

domains are often referred to as the succinate dehydrogenase and fumarate reductase portions of SQR and QFR, respectively. The hydrophobic membrane anchor domain subunits C and D are necessary to confer the quinone oxidoreductase activity to both SQR and QFR. Although both enzymes are bi-directional in that they readily oxidize succinate or reduce fumarate, they are poised to function differently in vivo. As is shown in Table 1, SQR—in catalytic assays using artificial electron donors/acceptors —is 50-fold more efficient as a succino-oxidase than it is as a fumarate reductase.

Enzyme	Succinate oxidation			Fumarate reduction		Catalytic efficiency (k_{cat}/k_m)	
	k_{cat} (succinate /s^{-1})	k_m^{suc} (µM)	k_i^{OAA} (µM)	k_{cat} (fumarate /s^{-1})	k_m^{fum} (µM)	Succinate oxidase	Fumarate reductase
SQR	110	110	0.07	2	100	1,000	20
QFR	30	550	0.3	250	20	54	232

Table 1. Catalytic parameters for succinate oxidase and fumarate reductase reactions catalyzed by *E. coli* SQR and QFR[a]

[a]Enzyme activity was determined on purified enzymes as described in reference 69. Enzyme activity was measured by established procedures at 30°C, pH 8.0. For succinate oxidase activity of either SQR or QFR, the activity was measured as the decrease in absorbance at 600 nm in the presence of succinate, 1.5 mM phenazine ethosulfate (PES), and 50 µM 2,6-dichloroindophenol (DCIP) (ε_{600} = 21.8 mM^{-1} cm^{-1}) and 20 mM succinate. Fumarate reductase activity with the low-potential donor benzylviologen (BV) (E_{m7} = −359 mV) was performed in a cuvette continuously flushed with argon, and the BV was reduced by the addition of a stoichiometric amount of sodium dithionite so that the initial OD$_{602}$ was approximately 1.8. To maintain anaerobiosis prior to initiating the reaction, 10 mM glucose, glucose oxidase, and catalase were added to the assay cuvette. The reaction was initiated by adding either enzyme or 10 mM fumarate to the assay cuvette. Progress of the assay was followed by monitoring the decrease in absorbance at 602 nm (ε_{602} = 9.6 mM^{-1} cm^{-1}) in a UV/VIS spectrophotometer equipped with a temperature-controlled cuvette.

Conversely, QFR is only fivefold more efficient as a fumarate reductase than it is as a succino-oxidase. The enzymes are, however, physiologically quinone oxidoreductases, but the situation is a little more complicated in trying to directly compare catalytic activity for the enzymes with quinones (67). Nevertheless, SQR is more efficient at reducing ubiquinone than is QFR, whereas QFR is much more efficient at oxidizing menaquinol than is SQR (15, 67). Thus, not surprisingly, the enzymes appear to have evolved to function best in their proper ecological niche.

Both SQR and QFR from *E. coli* are hetero-tetrameric membrane proteins with two subunits (*sdhA*, *frdA*, flavoprotein subunits; *sdhB*, *frdB*, iron-sulfur proteins) forming

an extra-membrane domain and two subunits (*sdhC*, cyt b$_L$ [SQR] *frdC*; and *sdhD*, cyt b$_S$ [SQR], *frdD*) forming an integral-membrane domain (residue numbers retain the chain name to prevent confusion). This architecture is optimally designed to couple the oxido-reduction of a water-soluble dicarboxylate to a membrane-soluble quinone. Spectroscopic and structural studies have revealed the presence of four covalently attached cofactors in each complex: a flavin adenine dinucleotide (FAD) (51) covalently linked to a histidyl residue, and three iron-sulfur (Fe:S) clusters. The covalent linkage of the FAD cofactor to the mammalian mitochondrial SQR was the first example of such a linkage to any protein (114), and it was subsequently shown that *E. coli* QFR contained a similar linkage (116). After many years of controversy in the 1980s it became clear that three distinct types of iron-sulfur clusters are present in both mammalian and prokaryotic SQR and QFR. The history of this controversy is elegantly reviewed by Beinert (5), and this article includes many of the primary references for determination of the Fe:S composition of SQR and QFR. In the case of eukaryotic and *E. coli* SQR and QFR the Fe:S clusters include a [2Fe:2S] 2+,1+ cluster, a [4Fe:4S]$^{2+,1+}$ cluster, and a [3Fe:4S]$^{1+,0}$ cluster (Fig. 6). It is gratifying that the initial crystal structures of the *E. coli* enzymes (44, 121) confirmed that the assignments for the Fe:S clusters were correct.

(a)   (b)
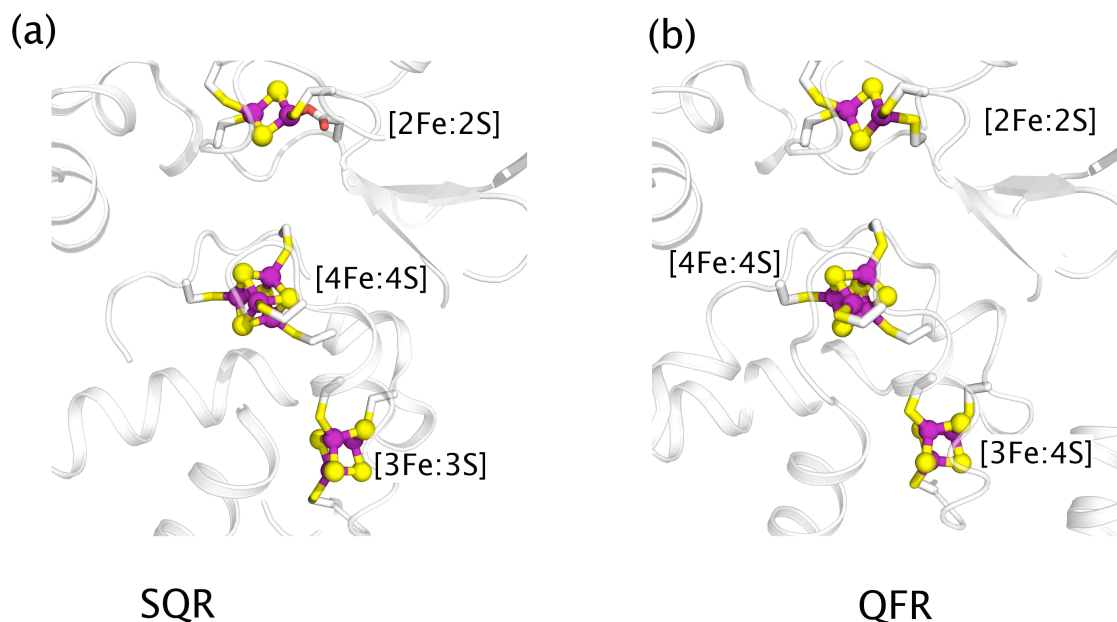
Figure 6. Representations of the SQR (a) and QFR (b) Fe:S clusters. (a) SQR Fe:S clusters. Note the unique ligation of the [2Fe:2S] cluster in SQR due to the replacement of a cysteine ligand with Asp-B63. Other iron-ligating residues include Cys-B55, Cys-B60, and Cys-B75 to the [2Fe:2S] cluster; Cys-B149, Cys-B152, Cys-B155, and Cys-B216 to the [4Fe:4S] cluster; and Cys-B159, Cys-B212, and Cys-B206 to the [3Fe:4S] cluster. (b) QFR Fe:S clusters. Iron-ligating residues include Cys-B57, Cys-B62, Cys-B55, and Cys-B77 to the [2Fe:2S] cluster; Cys-B148, Cys-B151, Cys-B154, and Cys-B214 to the [4Fe:4S] cluster; and Cys-B158, Cys-B204, and Cys-B210 to the [3Fe:4S] cluster. For both clusters, iron atoms are purple and sulfur atoms are yellow. The main-chain ribbon and side-chain carbon atoms are white.

In addition to the covalent flavin and Fe:S centers, SQR (but not *E. coli* QFR) contains a noncovalently bound *b*-type heme in the membrane-spanning region (52).

In both enzymes, the FAD located in subunit A is part of the active site for dicarboxylate interconversion, and an active site for the interconversion of Q and QH_2 lies at the cytoplasmic side of the membrane interface and is composed of residues from the B, C, and D subunits (44, 121). Analyses of the X-ray structures

(Fig. 4) also indicated that the cofactors were arranged linearly with intercofactor distances <14 Å (Fig. 7) within the physiological limit of electron transfer reactions (86).

As shown in Fig. 4, the structures also confirm other results from spectroscopic and enzymatic studies, notably the overall similarity between SQR and QFR. As anticipated, SQR and QFR each adopt similar folds in the soluble domain. Structural alignment of the flavoprotein subunit of *E. coli* SQR and QFR shows a root mean square (rms) deviation of 1.44 Å for 535 C_α atoms, while structural alignment of the iron-sulfur protein reveals an rms deviation of 1.256 Å for 221 C_α atoms.
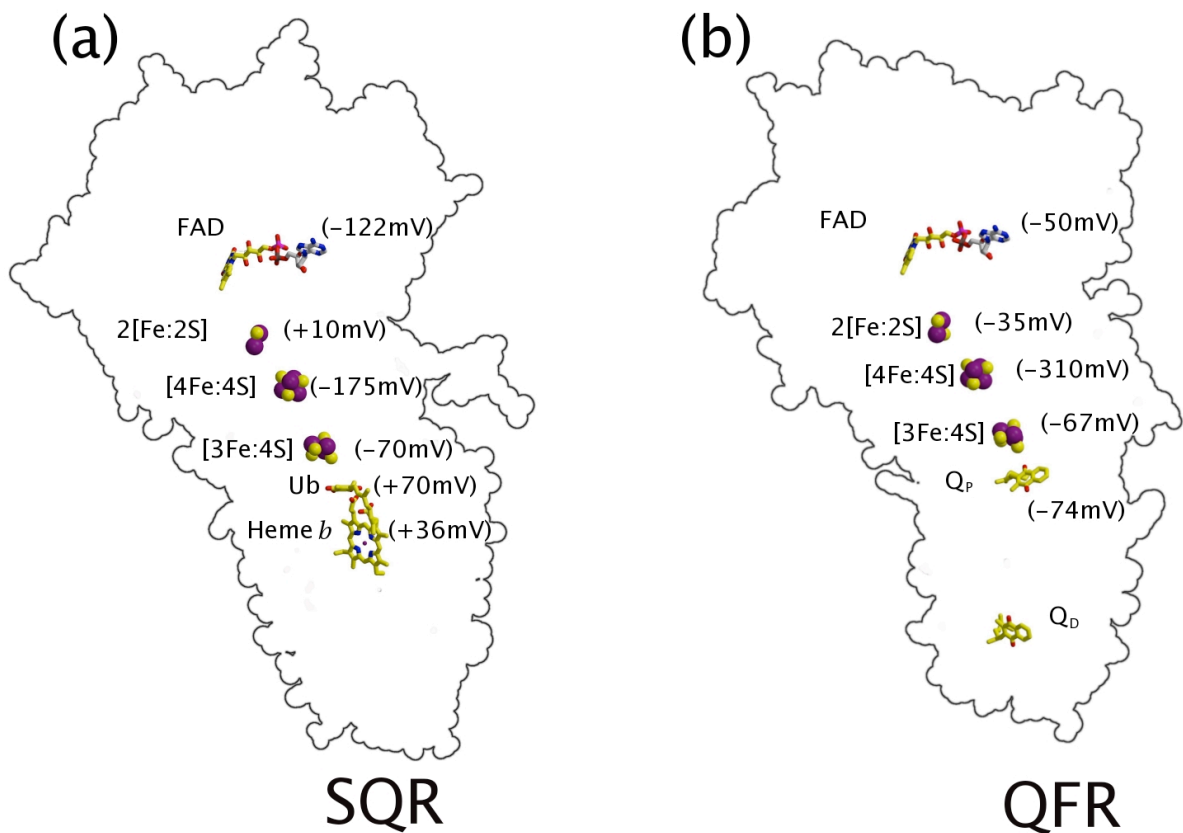
Figure 7. Comparison of cofactor arrangements in SQR and QFR. Each cofactor is labeled with its respective midpoint (pH 7) reduction potential, and distances are represented as lines. (a) SQR cofactor arrangements in relation to the entire complex. (b) QFR cofactor composition in relation to the entire complex. FAD, ubiquinone, and heme *b* are yellow, oxygen is red, nitrogen is blue, phosphate is magenta, and iron is purple. Additionally, the FAD adenine ring carbon atoms are gray to distinguish them from flavin. Sulfur is yellow and iron is purple in three Fe:S clusters.

Subunit A: The Flavoprotein

The flavoprotein is the largest subunit in each enzyme: 64 kDa in SQR and 67 kDa in QFR (20, 119). Of the four subunits in SQR and QFR, the flavoprotein exhibits the highest sequence identity between the two enzymes (41% identity and 58% similarity). The flavoprotein contains a covalently linked FAD (114, 116, 121),

which is at the active site for dicarboxylate interconversion. This covalent linkage is formed between the Nε atom of an absolutely conserved histidine (His-A45, SQR; His-A44, QFR) and the C8 atom of the FAD (Fig. 8) (114, 116).
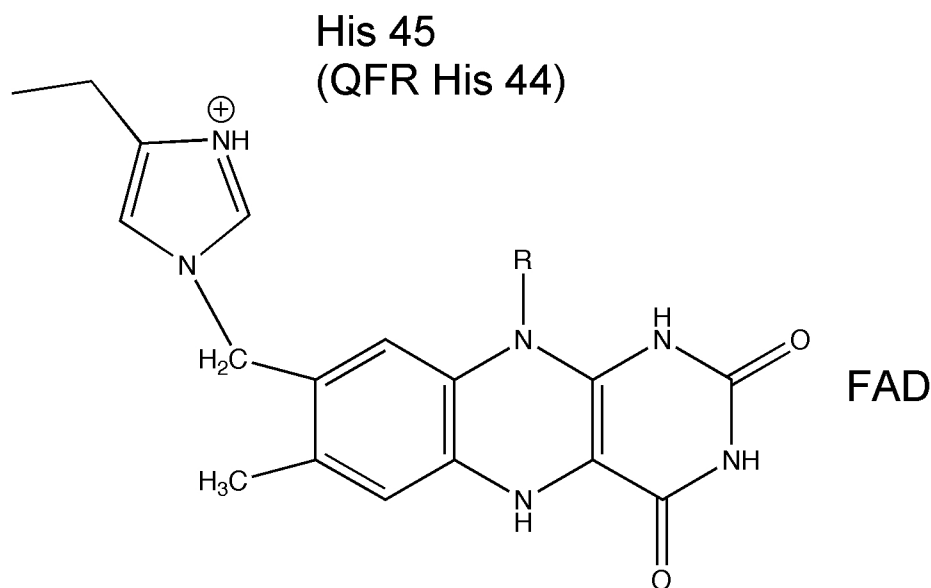
Figure 8. FAD 8α to His Nε covalent bond. The covalent bond between the 8α carbon of FAD and the Nε of histidine is shown. This is *shdA* His45 in SQR and *frdA* His44 in QFR.

Formation of the histidyl-FAD bond presumably is autocatalytic in SQR and QFR but requires catalytic turnover of the enzyme to complete the covalent linkage. Proposed mechanisms for the covalent attachment of flavins to proteins have been reviewed in detail (75), and the architecture of the FAD binding site in SQR and QFR is consistent with the autocatalytic iminoquinone methide attachment (27, 28).

Thus, mutation of side-chain amino acids that affect binding of dicarboxylate substrates to the active site often results in loss of covalent linkage to FAD, as was initially shown with QFR (10). Mutations that affect the covalent FAD linkage in human SQR have been linked to late-onset neurodegenerative disease (9), and the equivalent mutations in the *E. coli* enzymes (*sdhA* Arg399 or *frdA* Arg390) are also known to result in enzyme containing noncovalent FAD (16). Covalent attachment of FAD is one factor, along with the protein environment, that results in a dramatic increase in the reduction potential of the covalent FAD compared with free FAD (E_{m7} = –220 mV) to ~–70 mV in SQR and ~–55 mV in QFR (2, 10, 26, 89). The rise in reduction potential along with other electronic factors affecting the flavin becomes crucial for succinate oxidation (10, 26, 75). Site-directed mutants of either SQR or QFR that lose covalent linkage to FAD can no longer oxidize succinate but retain fumarate reductase ability (10). Soluble homologs of the flavoprotein subunit exist in several obligate anaerobes (79, 88); these fumarate reductase enzymes contain a noncovalent FAD with a lower reduction potential (79, 92) and are essentially unable to oxidize succinate (92). The evolutionary retention of a covalently attached FAD in QFR may reflect the in vivo requirement for QFR to oxidize succinate when *E. coli* is switching between anaerobic and aerobic respiration.

The mechanism of succinate-fumarate interconversion in SQR and QFR

The interconversion of succinate and fumarate occurs at the dicarboxylate binding site of SQR and QFR, as described below. Initial studies of succinate oxidation used preparations of succinate dehydrogenase that were not pure, and it

was not initially recognized that the complete SQR enzyme was membrane bound. Nevertheless, it was shown that mammalian succinate dehydrogenase was a reversible enzyme capable of both succino-oxidase and fumarate reductase activities (71). Succinate dehydrogenase or fumarate reductase activity is most conveniently measured using artificial electron acceptor/donors of appropriate redox potential (3, 69, 88). Succinate oxidation by both succinate dehydrogenase and fumarate reductase can be spectrophotometrically assayed using primary electron acceptors such as phenazine ethosulfate (or phenazine

methosulfate) (3) coupled with the reduction of 2,6-dichlorophenolindophenol. Fumarate reduction by either enzyme can be assayed using reduced viologen dyes such as benzyl or methyl viologen (3). Note that, as isolated, succinate dehydrogenase and fumarate reductase contain tightly bound inhibitory oxaloacetate (OAA) at their dicarboxylate binding site (3). The OAA binds more tightly to the oxidized forms of the enzyme than it does to the reduced enzymes

(2, 3). Thus, to accurately measure the initial rate of succinate oxidation the OAA must be removed from the dicarboxylate binding site by "activating" the enzyme in the presence of succinate or other weaker binding dicarboxylates, such as malonate (2, 3). Since the OAA binds much more weakly to reduced succinate dehydrogenase and/or fumarate reductase, it is not necessary to activate the enzymes to measure fumarate reduction.
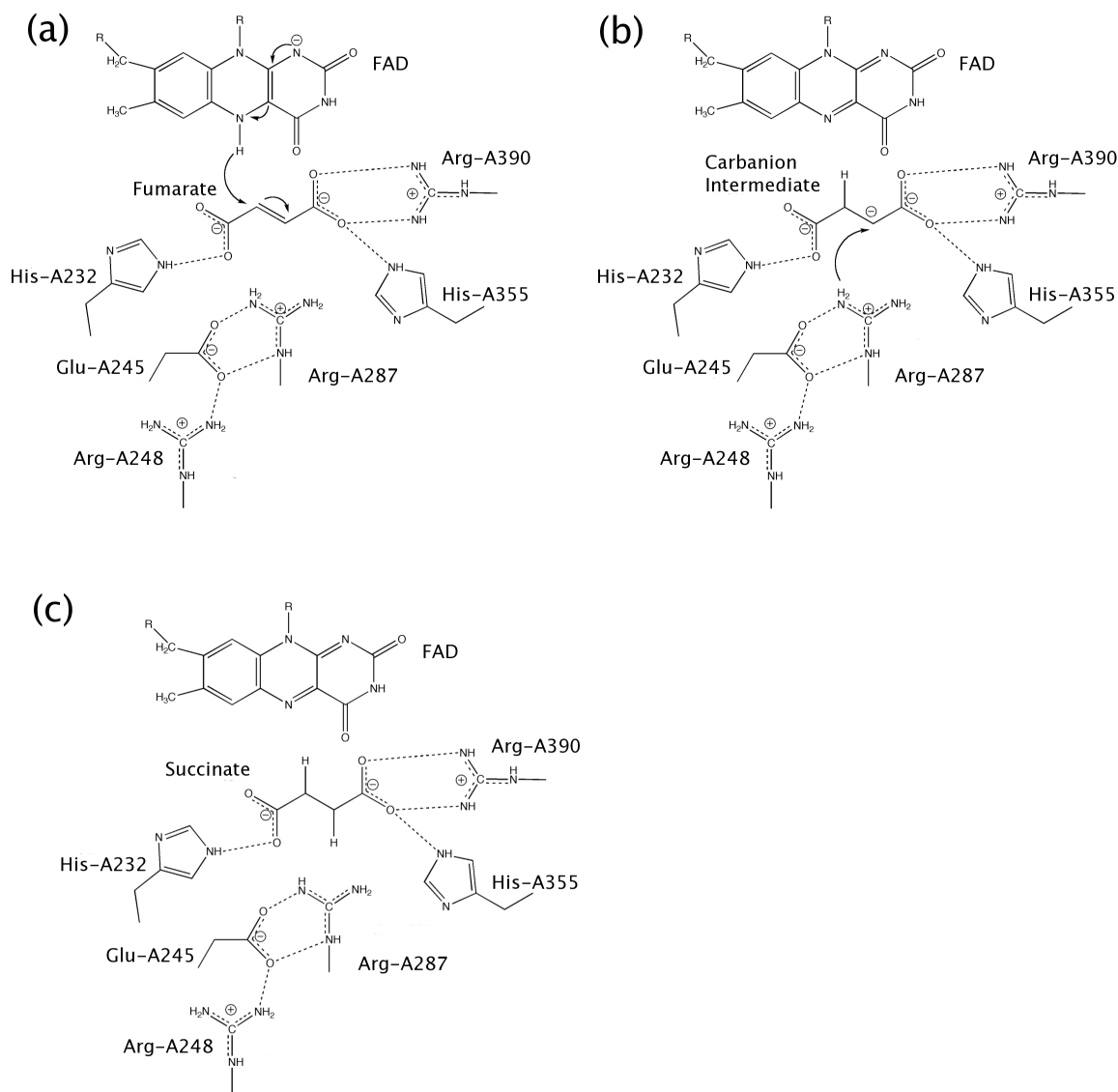
Figure 9. Fumarate reduction mechanism. (a) Hydride transfer to fumarate by FAD. Bound fumarate forms hydrogen bonds to the side chains of His-A232, His-A355, and Arg-A390. Reduced FAD transfers a hydride to the C-2 carbon on fumarate in a single step. (b) Proton transfer to the carbanion intermediate by Arg-A287 to yield succinate. (c) Regeneration of catalytically competent protein. Arg-A287 is reprotonated through a proton shuttle consisting of Glu-A245 and Arg-A248. FAD is re-reduced by electrons that are transferred from quinol through the Fe:S clusters. How FAD is reprotonated has not been determined.

The dicarboxylate-interconversion reaction mechanism has been best studied in the fumarate reduction direction by using soluble homologs of fumarate reductase from *Shewanella* spp. (80, 92). In *E. coli* QFR, as in its soluble homologs, fumarate reduction proceeds in two steps (Fig. 9). In the first step, the reduced FAD transfers a hydride to the double bond of fumarate, forming a carbanion intermediate. The hydride transfer is likely to be the rate-determining step (64). In the second step, the carbanion intermediate accepts a proton from Arg-A287 (Fig. 9).

Several highly conserved residues, including His A-242 (SQR)/His-A232 (QFR), Glu-A255 (SQR)/Glu-A245 (QFR), Arg A-286 (SQR)/Arg-A287 (QFR), His A-354 (SQR)/His-A355 (QFR), and Arg A-399 (SQR)/Arg-A390 (QFR), line the active site (Fig. 10).

(a)

QFR
flavoprotein subunit

(b)

Arg-A287

Arg-A248

His-A355

Arg-A390

His-A232

Glu-A245

fumarate

FAD
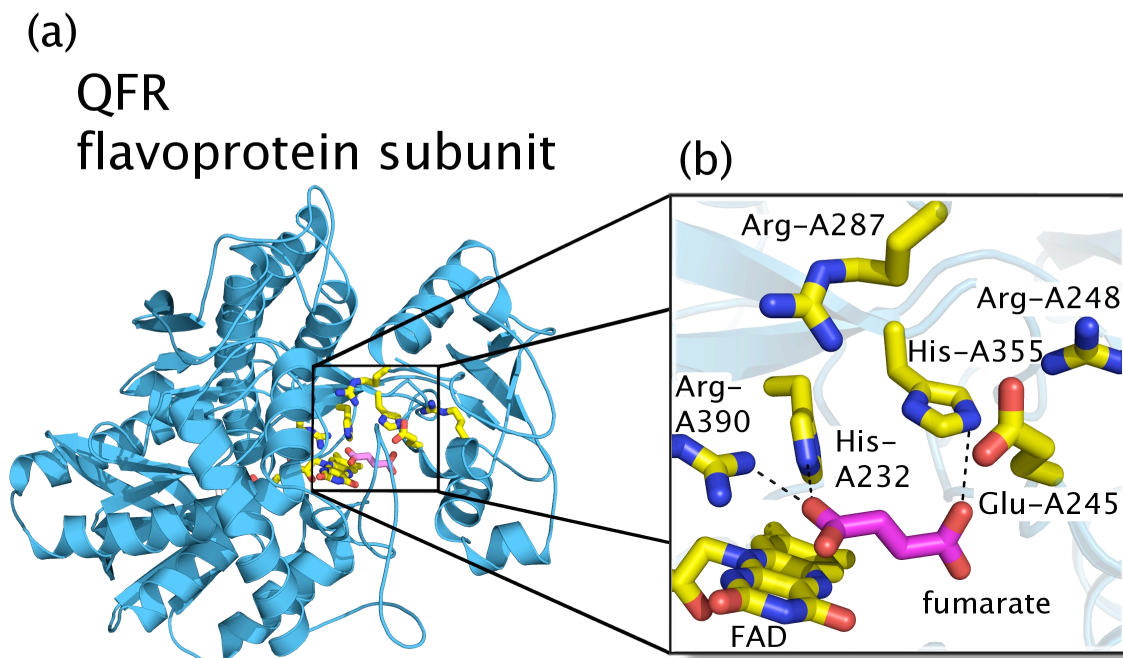
Figure 10. The QFR flavoprotein subunit (*sdhA*, SQR; *frdA*, QFR) and a close-up of the active site. (a) The fumarate binding site in relation to the rest of the flavoprotein. (b) Close-up of fumarate active site. Fumarate carbon atoms are magenta, and oxygen atoms are red. Carbon atoms of catalytically relevant residues and FAD are yellow, with oxygen atoms being red and nitrogen atoms being blue. Hydrogen bonds are represented as dashed lines.

An elegant combination of site-directed mutagenesis (25, 80, 87, 112) and crystallography (107) in the soluble fumarate reductase homologs assigned Arg-A287 (QFR) as the proton shuttle for the second step of the reaction, while the remaining conserved residues are likely responsible for binding of the substrate. A number of secondary proton shuttles may provide a pathway for protons between the active site and the cytoplasm (Fig. 9) (112).

The local active-site environment facilitates fumarate reduction in many ways. First,

hydrogen bonds from Arg-A390 and His-A355 to fumarate create a dipole along the

fumarate double bond (92). The electrostatic effect induces a δ+ charge on the C3

carbon of the fumarate double bond, making fumarate more susceptible to hydride

transfer at this position. Second, twisting of the fumarate double bond (Fig. 11) by

the protein environment may destabilize π-π overlap

and raise the fumarate free energy.
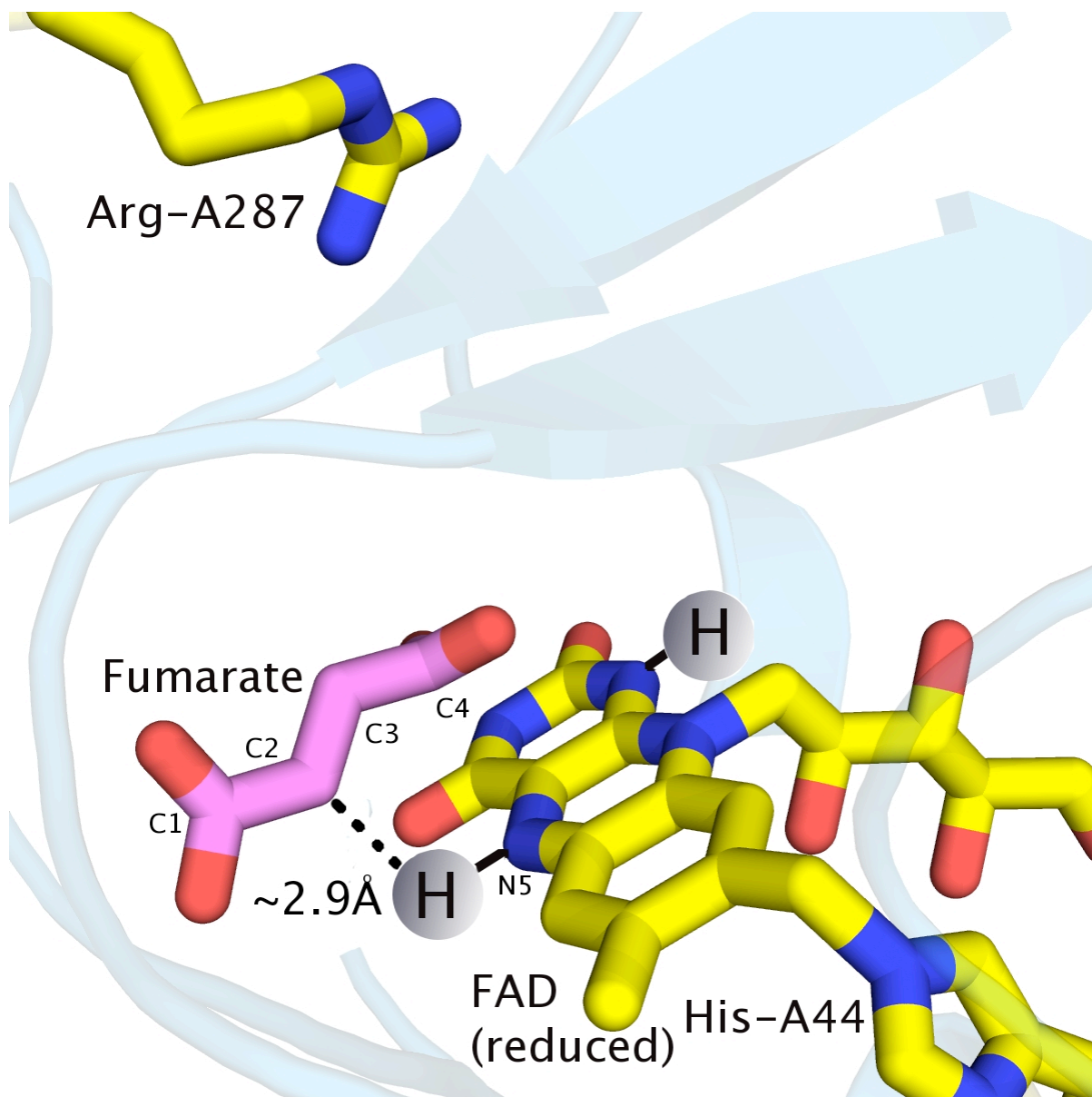
Figure 11. The QFR active site. Fumarate binds near the reduced FAD. The distance between the N5 of the FAD and the C-2 atom of the fumarate is 3.4 Å, while the distance from a modeled hydride on FAD and the C-2 atom of fumarate is ~2.9Å. The position of fumarate (carbons are magenta) is shown modeled into the active site. In the hydride donor, FAD, and proton donor, Arg-A287, carbon atoms are yellow, oxygen atoms are red, and nitrogen atoms are blue. The oxidation state of FAD could not be determined unambiguously by the crystal structures and is shown here modeled as the reduced state.

Structures cocrystallized with fumarate show a twisted conformation for the C2-C3 double bond (60). Domain rearrangements near the flavoprotein active site may stabilize the twisted conformation to facilitate catalysis by forcing fumarate to mimic the transition state (58, 92).

In classical enzymology, the enzyme provides an alternate path to product formation, speeding up the reaction in both the backward and forward direction. SQR and QFR violate the definition of a classic catalyst. While each enzyme can catalyze the opposite reaction in vitro and can functionally replace the other in vivo (31, 66), both enzymes are more efficient in one direction than in the other (Table 1). So far, two separate pieces of the molecular architecture have been shown to control the direction of the reaction. The first is the identity of the side-chain residues near the electron transfer cofactors of each enzyme. These side chains tune the reduction potentials of each cofactor and control the preferential direction of electron transfer through the complex (Fig. 7). In considering the full fumarate reduction reaction $2H^+ + 2e^- + $ fumarate $\rightarrow$ succinate, it is clear that electrons are one substrate. Since SQR limits the availability of electrons at the active site, fumarate reduction is not preferentially catalyzed, even in the presence of fumarate, due to limitation of the electron substrate.

A second parameter controlling the direction of the reaction in SQR and QFR is control of the one-electron reduced flavin semiquinone intermediate during enzyme turnover. Electron paramagnetic resonance (EPR) analysis of SQR and QFR reveal differences in the FAD flavin semiquinone intermediate during enzyme turnover, with the SQR FAD transitioning through anionic flavin semiquinone

26

(FAD$^{\bullet-}$), while QFR apparently uses a neutral flavin semiquinone (FADH$^{\bullet}$) (69).

The side chains within coulombic distance of the FAD may suggest how the flavin semiquinone intermediate is controlled. An examination of the environment around the FAD in the *E. coli* SQR and QFR, as well as other homologs, reveals an identical residue at a conserved position depending on whether the enzyme is SQR or QFR. SQR normally has a glutamine residue (Q50 in *E. coli* SQR), while the preponderance of QFRs have a glutamate (E49 in *E. coli* QFR) at the equivalent position. When the equivalent residues are swapped between SQR and QFR (i.e., the glutamine in SQR is switched to a glutamate like that found in QFR and the converse mutation is done to QFR), SQR becomes a better fumarate reductase while QFR becomes a more efficient succinate oxidase (69). This is explained, in part, by the observation that electrostatic differences caused by the γ-carboxylate of glutamate or the amide of glutamine shift the redox potential of FAD and the stability of the flavin semiquinone radical so that the radical in QFR becomes more like that in SQR (37, 69). The change in reduction potential along with the changed stabilization of the flavin radical in part accounts for kinetic differences between both enzymes and suggests that there is a change in the protonation state of the FAD environment. In addition, these studies suggest that the "forward reaction" of each enzyme uses a hydride transfer while the "backward reaction" uses a hydrogen atom transfer. These differences are not enough, however, to account for all of the catalytic changes observed that probably reflect a multitude of subtle changes in the flavin environment and dicarboxylate binding site (69).

The above observations may relate to another intriguing catalytic difference

between SQR and QFR in their respective abilities to reduce fumarate. As with most enzymes, fumarate reductase increases its rate of catalysis when there is a greater thermodynamic driving force, but succinate dehydrogenase demonstrates an unusual behavior termed the "tunnel diode" effect (105). These studies were initially done with the mitochondrial succinate dehydrogenase; however, the *E. coli* enzyme shows similar properties (89). It was shown that succinate dehydrogenase is able to efficiently catalyze fumarate reduction above a redox potential of approximately –60 mV (7.0); conversely, below this potential, the rate of catalytic fumarate reduction abruptly decreases even though the redox driving force has increased. This effect resembles the current-voltage characteristics of a tunnel diode found in electronic circuits. Succinate dehydrogenase is an excellent fumarate reductase, yet this activity is only found over a narrow range of redox potential. Note that fumarate reductase does not demonstrate this behavior, as its activity increases along with its potential driving force. The physical principles underlying the tunnel diode effect have not been determined but have been suggested to relate to subtle differences in the properties of the dicarboxylate binding site of SQR and QFR (89, 105). It is possible that the tunnel diode effect may limit fumarate reduction under hypoxic conditions and prevent SQR reduction of fumarate during anoxic conditions.

Subunit B: The Iron-Sulfur Protein Subunit

The iron-sulfur protein subunit comprises two distinct domains and is the second largest subunit (26.8 kDa in SQR and 27.0 kDa in QFR). The first domain adopts a plant-type ferredoxin fold (type I ferredoxin) and contains the [2Fe:2S] cluster, while
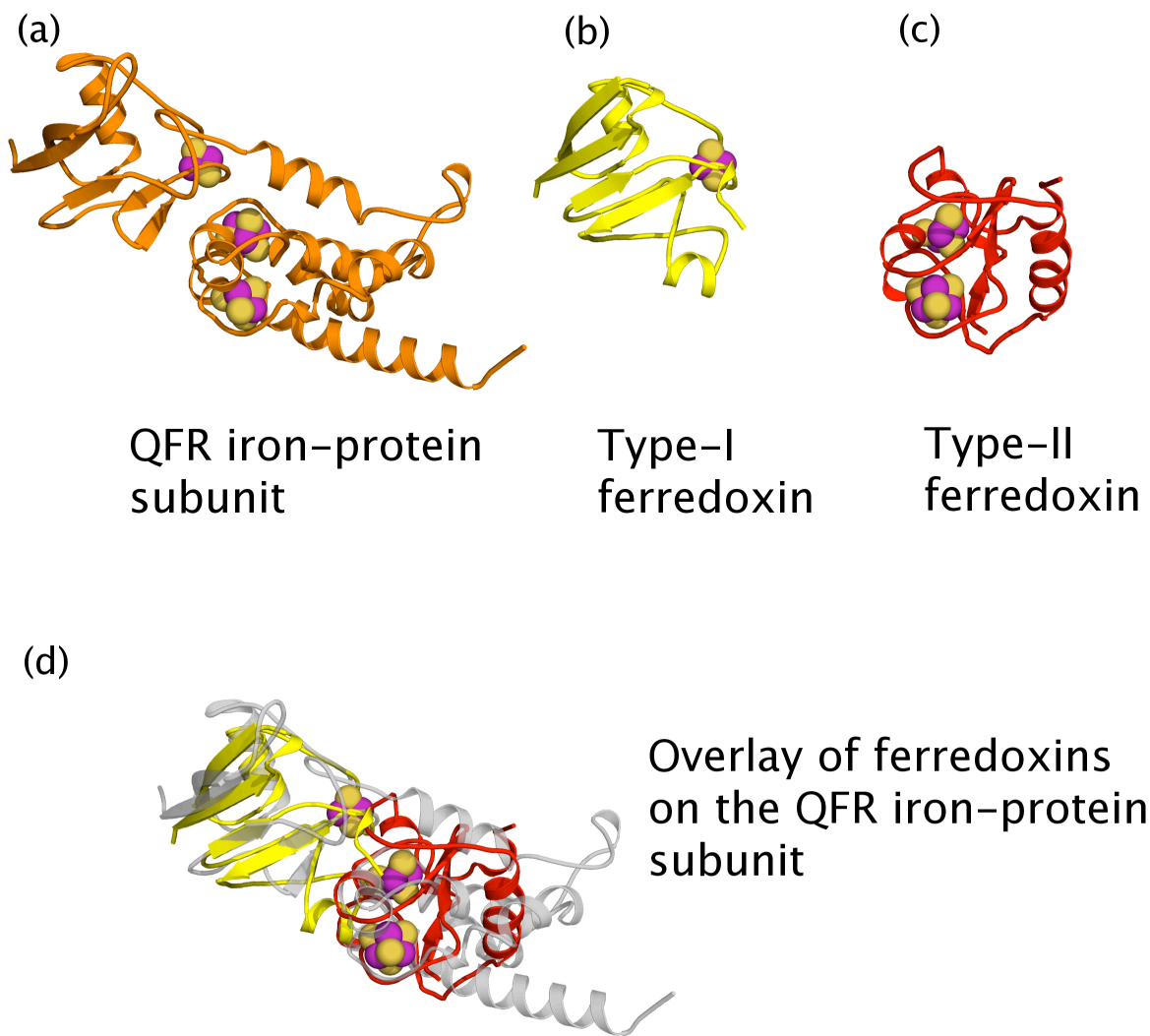
Figure 12. Comparisons of the iron-protein subunit fold with a type I and type II ferredoxin. (a) The QFR iron-protein subunit and positions of Fe:S clusters. The iron-protein main chain is orange. (b) Type I ferredoxin. The type I ferredoxin (yellow) contains a single [2Fe-2S] cluster. Shown is the type I ferredoxin from *Anabaena* 7120 (46) (PDB ID 1FRD). (c) Type II ferredoxin. The type II ferredoxin (red) contains two clusters, [4Fe:4S] and [3Fe:4S], in opposite positions compared with QFR. Shown is the type II ferredoxin from *Azotobacter vinelandii* (29) (PDB ID 1A6L). (d) Superposition of the type I and type II ferredoxins and the QFR iron protein subunit. The overlay displays the structural similarity between the ferredoxins and the QFR iron protein subunit (light gray). The root mean square deviation (RMSD) of atom positions in alignment between the *Anabaena* 7120 type I ferredoxin (46) and QFR is 1.3 Å for 68 C_α atoms, while the RMSD of atom positions in the alignment between the *A. vinelandii* 7Fe ferredoxin (29) and QFR is 1.0 Å for 37 C_α atoms. All iron atoms are purple and sulfur atoms are yellow in the iron-sulfur clusters.

the second domain adopts a bacteria-type ferredoxin fold (type II ferredoxin) and contains both the [3Fe:4S] and the [4Fe:4S] clusters (Fig. 12) (44). The iron protein is physically positioned between the dicarboxylate interconversion active site in the flavoprotein subunit and the Q—QH_2 interconversion active site in the membrane. The Fe:S clusters provide a pathway for efficient electron transfer between the two active sites of these enzymes. The history of the discovery of Fe:S clusters in SQR and QFR is described in an excellent review from Beinert (5). Note that succinate dehydrogenase was one of the first proteins known to demonstrate tightly bound iron (104). The compositions of the Fe:S clusters of SQR were first identified and characterized with EPR spectroscopy in bovine heart mitochondria (6, 7, 85, 94). Subsequent studies in *E. coli* QFR confirmed the same composition of Fe:S clusters in this enzyme (47, 48, 78). In mitochondrial SQR, *E. coli* SQR, and QFR, Fe:S cluster irons are coordinated by cysteines in ferredoxin-like sequence motifs with the [4Fe:4S] cluster coordinated by a C-X-X-C-X-X-C-X_3-C-P motif and the [3Fe:4S] cluster coordinated by a C-X_5-C-X_3-C-P motif (22, 24). In QFR, the [2Fe:2S] cluster is coordinated by a C-X_4-C-X-X-C-X_{10}-C-P motif. Infrequently, in *E. coli* SQR, the third cysteine of the [2Fe:2S] coordinating motif is replaced by an aspartate (24), a unique alteration of this motif in SQRs. Mutation of Cys-B65 in QFR to aspartate to mimic the SQR [2Fe:2S] structure had no overall effect on the midpoint potential or catalytic activity (117), and it is not known why aspartate is found in this position in SQR (Fig. 6).

As mentioned above, the reduction potential of the Fe:S clusters is tuned to control the availability of electrons at the active site FAD (Fig. 7). All three Fe:S

clusters of SQR have higher midpoint potentials (83, 85) than their counterparts in QFR, but in both enzymes, the reduction potentials of the [4Fe:4S] cluster is unusually low. Prior to the determination of crystal structures, it was speculated that this Fe:S cluster could be off-pathway for electron transfer (54). The crystal structure reveals that edge-to-edge distances of the [4Fe:4S] cluster to the [2Fe:2S] and [3Fe:4S] clusters (Fig. 7) fall within physiological electron transfer ranges (<14Å) (86). While the thermodynamic barrier imposed by the low [4Fe:4S] cluster potential suggests that electron transfer to the [4Fe:4S] cluster is not rate limiting, site-directed mutagenesis of *E. coli*SQR that introduced negative charges near the 4Fe:4S lowered the potential (by ~70 mV to –285 mV) and decreased catalytic turnover by 65% (17). That the [4Fe:4S] cluster of QFR is a direct participant in electron transfer reactions had previously been shown by protein film uanidine ry and mutagenic studies of *E. coli* QFR (37).

These studies showed that when the [4Fe:4S] cluster is reduced it results in a boost in catalytic rate for fumarate reduction by QFR. This is somewhat reminiscent of changes in the electronic properties of the FAD that apparently contribute to the tunnel diode properties of SQR in the flavoprotein subunit. These findings are consistent with an interpretation in which oxido-reduction of the redox centers has direct influence on catalytic rates in both SQR and QFR.

Subunits C and D: The Membrane Subunits

The integral membrane subunits of SQR and QFR contain the second active site in the enzyme (Q-site), which performs oxido-reduction of the membrane-
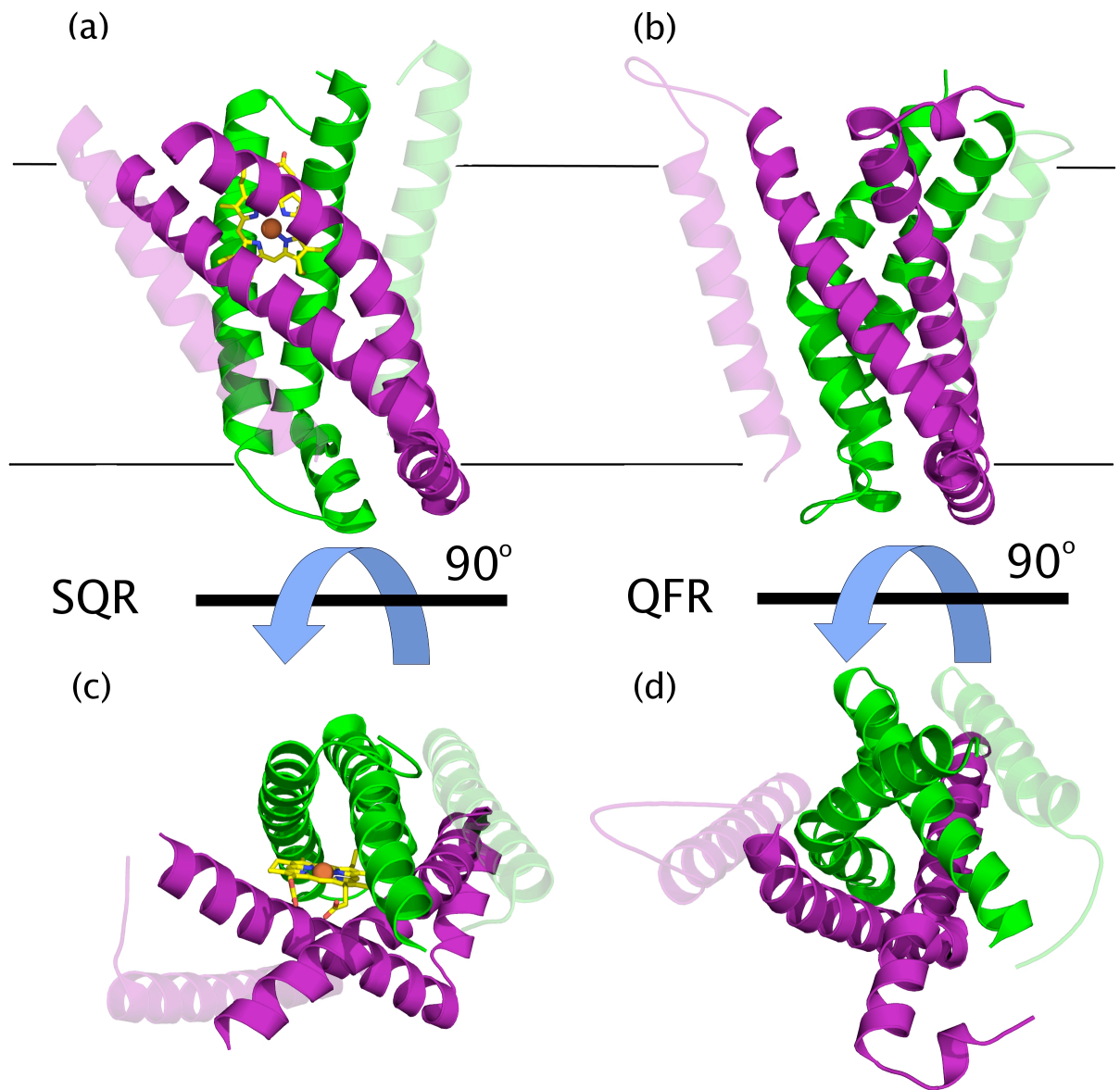
Figure 13. Comparison of four-helix bundles in the QFR (a and c) and SQR (b and d) integral membrane subunits (*sdhC*, *frdC* in purple and *sdhD, frdD* in green). Ribbons shown in bold coloring represent the four-helix bundle motif. The remaining helices are shown with transparency to differentiate them from the four-helix bundle. Ubiquinone (a), heme (a), and menaquinol (b) are yellow. Oxygen atoms are red, nitrogen atoms are blue, and iron is orange.

Soluble small molecule quinone. In contrast to the soluble subunits of SQR and

QFR, which share considerable sequence similarity, there is no detectable

sequence identity in the integral membrane subunits that contain the Q-site. Despite this, the C and D integral membrane subunits of both enzymes each comprise three transmembrane helices that come together to form a four-helix bundle structural motif (Fig. 13).

The membrane-spanning subunits of SQR and QFR additionally differ in cofactor association. SQR contains a *b*-type heme, heme b_{556}, which is absent in QFR (Fig. 14). Each complex also preferentially associates with a different type of quinone molecule; in SQR, ubiquinone (Fig. 3b) is used as the physiological electron acceptor, while in QFR menaquinol (Fig. 3c) is used as the electron donor.

Note, however, that the Q-binding sites in both QFR and SQR can accommodate either ubiquinone or menaquinone molecules as evidenced by both in vivo and in vitro studies (31, 66, 69). One explanation of why the enzymes preferentially bind one quinone over the other is that the redox potential of the [3Fe:4S] cluster, which is the direct electron donor/acceptor for SQR and QFR, respectively, is poised to interact preferentially with either the higher potential ubiquinone (+ 90 mV) or the lower potential menaquinone (−74 mV). As would be expected for active sites that bind different small molecules, the side-chain residues of each Q-site differ to optimize the binding of one species (Fig. 15). The location of the Q-site with respect to the soluble domain also differs; an alignment of SQR and QFR soluble domains results in Q-sites that are positioned 15 Å away (Fig. 14) from each other (121).
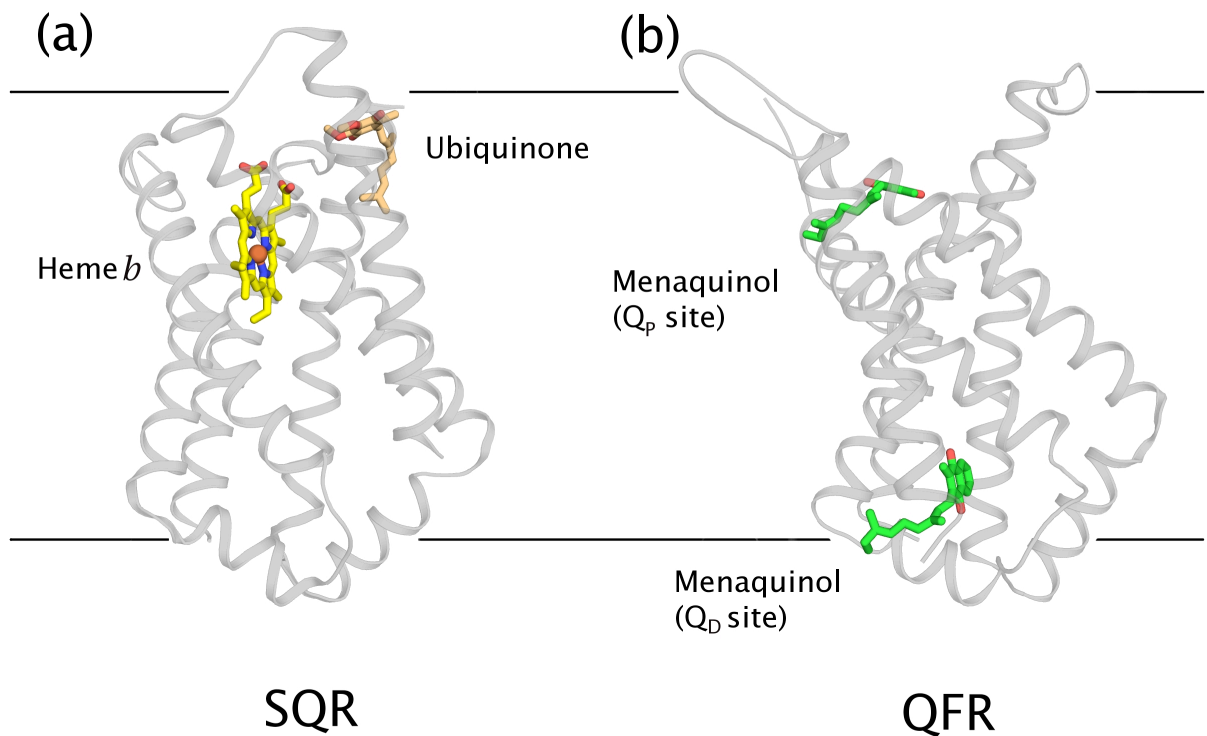
Figure 14. Comparison of relative Q-binding positions in SQR and QFR. (a) SQR ubiquinone binding site. (b) QFR menaquinol binding sites. Only the integral membrane domains are shown for clarity (light-gray ribbons). Heme *b* carbon atoms are yellow, iron atoms are brown, ubiquinone carbon atoms are tan, and menaquinol carbon atoms are green. In all the molecules, oxygen atoms are red and nitrogen atoms are blue.

Ubiquinone binding in SQR

It was shown by EPR spectroscopy more than 30 years ago that mitochondrial SQR stabilizes a ubi-semiquinone radical (94). Photoaffinity labeling with quinone analogs also identified potential amino acid residues in bovine mitochondrial SQR involved in side-chain interactions with the quinone (62, 103).

34

The crystal structure of *E. coli* SQR (Fig. 15) confirmed the general architecture of

the quinone binding site in bacterial SQR (121).
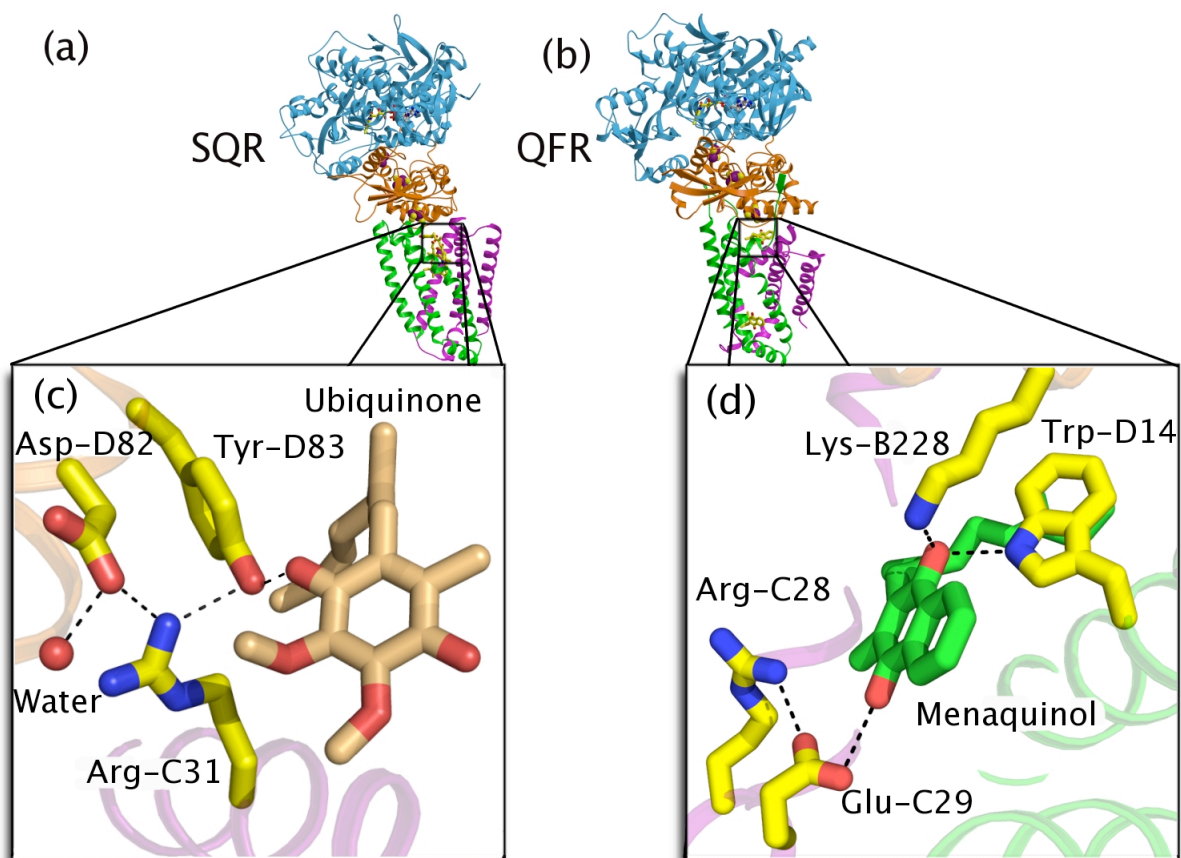
Figure 15. Q-binding sites in SQR and QFR in relation to the entire complex. (a) SQR Q-site. Ubiquinone carbon atoms are tan, with oxygen atoms are red. (b) QFR Q-site. Menaquinol carbon atoms are green, with oxygen atoms being red. In both panels, side-chain carbon atoms are yellow, oxygen atoms are red, and nitrogen atoms are green.

In *E. coli* SQR both the crystal structure (89) and kinetic data (67) are consistent

with a single catalytic pocket termed the QP-site (for Q-proximal), where quinone

binds. The Qp-site is located within 8 Å of the [3Fe:4S] cluster and 7 Å from the edge of the *b*-heme moiety, both distances well within the range for efficient electron transfer (86). Co- crystal structures are available for the *E. coli* SQR with ubiquinone and the Q-site inhibitor atpenin-A5 (36). The different binding positions for these molecules suggest that ubiquinone and ubi-semiquinone (the one-electron intermediate) bind in the SQR Q-site in two distinct positions during the catalytic cycle, consistent with other quinone binding sites, suggesting a general plasticity for
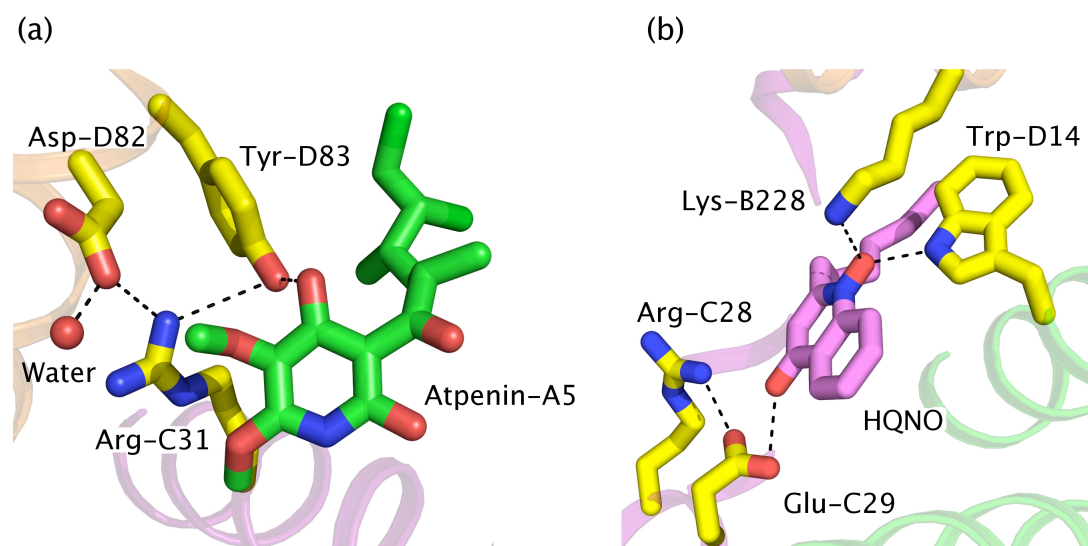
Figure 16. Inhibitors bound to Q-sites in QFR and SQR. (a) The inhibitor atpenin-A5 (carbon atoms are green) in the SQR Q-site and contacts. Carbon atoms of atpenin-A5 are green, with oxygen atoms in red and nitrogen atoms in blue. Side-chain carbon atoms are yellow; oxygen atoms are red, and nitrogen atoms are blue. Careful inspection of the atpenin-A5 binding site and the ubiquinone binding site (Fig. 15) shows a different binding position for these two species. (b) The QFR Q-site inhibitor 2-heptyl-4-hydroxy quinoline *N*-oxide (HQNO; carbon atoms are magenta) with contacts. HQNO carbon atoms are magenta, with oxygen atoms being red and nitrogen atoms being blue. Comparison with Fig. 15 shows that the position of this inhibitor is similar to that of the menaquinol. HQNO is proposed to act as a menasemiquinone analog. Side-chain carbon atoms are yellow, oxygen atoms are red, and nitrogen atoms are blue.

quinone binding sites. This phenomenon has previously been observed in the photosynthetic reaction center (19) and is proposed as a mechanism to protect the ubi-semiquinone radical intermediate from interaction with solvent. The co-structure of SQR with ubiquinone (121) reveals a single hydrogen bond between the ubiquinone O1 atom and the side chain hydroxyl of Tyr-D83 (Fig. 15). The costructure with the Q-site inhibitor atpenin-A5 (36) reveals that a deeper binding pocket for quinone is available (Fig. 16), which would prevent the premature disassociation of a highly reactive, partially reduced semiquinone. In the second binding position, additional hydrogen bonds to Ser-C27 and His-B207 bring ubiquinone into close proximity to a putative proton shuttle pathway (Fig. 17). This putative pathway would provide a mechanism for protons to enter the binding pocket in the membrane-spanning region.
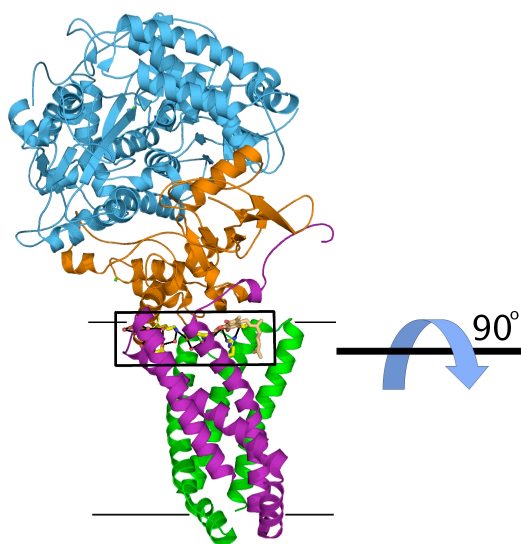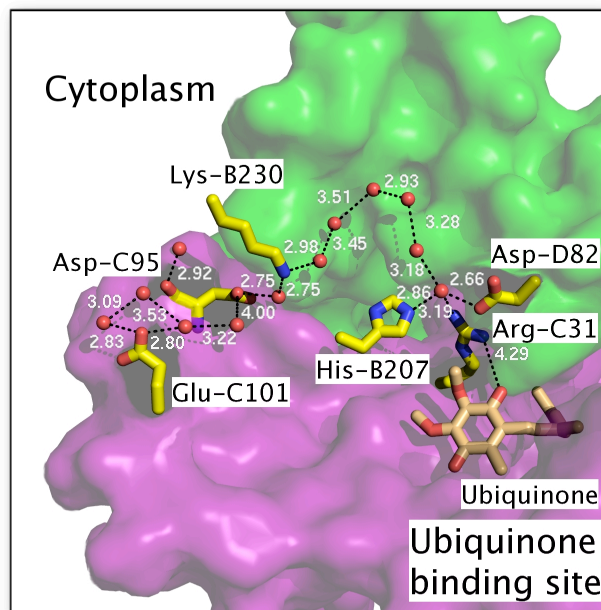
Figure 17. SQR proton shuttle to ubiquinone binding site. (a) The SQR structure. (b) A close-up of the proton shuttle and ubiquinone binding site. The integral membrane subunits are represented with surface models and are purple (*sdhD*, SQR; *frdD*, QFR) and green (*sdhD*, SQR; *frdD*, QFR). The proton shuttle comprises ordered water molecules and residues Lys-B208, Lys-B230, Arg-C31, Asp-C95, Glu-C101, and Asp-D82. Water molecules are shown as red spheres. Side-chain carbons are yellow, oxygen atoms are red, and nitrogen atoms are blue. Ubiquinone is tan, and its oxygen atoms are red. Dashes represent the proposed pathway for the proton shuttle.

Cyt b_{556}

The crystal structure of SQR (121) includes a b-type heme (52) that uses His-C84 and His-D71 as the Fe- ligands, confirming what was expected from spectroscopic studies (23, 70, 90). The position of heme b_{556} with respect to the electron transfer pathway was a surprise since the heme is off-pathway (Fig. 7) for electron transfer between the [3Fe:4S] cluster and ubiquinone. As electrons are delivered to the Q-site from the [3Fe:4S] cluster, the structure raises the possibility that the first electron can reduce either the heme directly or the quinone. It is ~11 Å from the [3Fe:4S] cluster to the edge of the heme, whereas it is only ~7 Å from the Fe:S cluster to the quinone (121). Subsequently, EPR studies indicate that an intact quinone binding site is necessary for reduction of the heme (111). Although the logical conclusion from these studies is that the quinone is reduced before the heme, pulse radiolysis investigation of isolated *E. coli* SQR suggests that there can be a very rapid equilibration of the electron between the heme and the quinone so that first electron could be delivered to either redox center (4). Further study is clearly needed to clarify the role order of delivery of electrons to the b-heme.

The overall role of the heme in SQR is also controversial. One role for the heme is structural, as it has been shown that assembly of the SQR holoenzyme is perturbed in *E. coli* heme-deficient mutants (82). Another proposal is that the heme may act as an "electron sink" during reduction of the enzyme. This additional cofactor would prevent electrons from accumulating on the FAD when ubiquinone is not immediately available by diverting electrons away from the iron-sulfur clusters (121). Since single-electron-reduced FAD is highly reactive, an additional cofactor in

39

the membrane-spanning region would prevent back-reactions in vivo (i.e., fumarate reduction) and, more importantly, would prevent inappropriate reactions such as the partial reduction of O_2 to form harmful reactive oxygen species (ROS) during aerobic respiration. The redox potentials of the cofactors in SQR would tend to pull electrons away from the flavin site, which is in direct opposition to what is the case for *E. coli* QFR where the cofactors are tuned so electrons are transferred toward the FAD (Fig. 7). This proposal is consistent with the known tendency of QFR to form ROS in vitro when oxygen is available from the flavin binding site, while SQR does not (38, 74). These interesting findings suggest one reason that organisms have evolved both a SQR and a QFR. As pointed out by Imlay (38), as *E. coli* transits from an

Menaquinol binding in QFR

The structure of QFR revealed electron density attributed to menaquinol in two positions: a proximal Q_P-position located in proximity to the [3Fe:4S] cluster of the *frdB* iron-sulfur protein subunit and a distal Q_D-position located on the opposite side of the membrane (Fig. 14) (44). The Q_P- and Q_D-sites are separated by ~25 Å, a distance too far for physiological electron transfer (86), in part explaining why QFR cannot itself support formation of a proton gradient. While the relevance of Q_D continues to be investigated, it is clear that menaquinol binding the Q_P-site is the immediate electron donor to the [3Fe:4S] cluster (32, 68, 106). Note also that a recent X-ray structure of porcine SQR also revealed two binding sites for the quinone site inhibitor 2-thenoyltrifluoroacetone (TTFA), and these sites were spatially separated across the membrane in a manner similar to what was seen in

QFR (106). There is no evidence that this distal quinone binding site has any functional significance in the mammalian SQR, and the hydrophobic TTFA inhibitor was crystallized with the enzyme at a concentration some two orders of magnitude higher than necessary for inhibition of the enzyme. It is also relevant that the di-heme members of the SQR and QFR family of enzymes (32, 57, 59, 60, 72) have a functional quinone catalytic site on the distal side of the membrane. Thus, it should be considered that the Q_D-site might be an evolutionarily conserved hydrophobic pocket that is functionally active in the di-heme-containing enzymes but nonfunctional in the single heme and/or no-heme members of the SQR/QFR family.

Unlike SQR, where quinone analogs adopt somewhat different conformations as compared to ubiquinone, comparisons of the costructure of QFR and menaquinol with the costructure of QFR and the semiquinone analog 2-*N*-heptyl-4-hydroxyquinoline *N*-oxide (HQNO) (45) reveal that both menaquinol and the semiquinone analog effectively bind to the same site (Fig. 16). Several residues in the membrane-spanning subunits stabilize menaquinol binding at this position, including Trp-D14, Arg-C28, and Glu-C29 (Fig. 15) (44). Glu-C29 had previously been identified in random mutagenesis studies as being important for quinol binding (118). EPR analysis of the Glu-C29 → Leu mutation showed an alteration in the stability of the semiquinone radical by increasing the lifetime by four orders of magnitude (33). Glu- C29 may play an important catalytic role in protonation reactions and by destabilizing the semiquinol radical to prevent possible side reactions between it and oxygen.

An unusual aspect of the Q-site in QFR is the formation of a hydrogen-bonding

interaction from the Lys-B228 Nζ atom to the menaquinol O1 atom (Fig. 15) (45). Lys-B228 lies on an amphipathic helix that rests on the membrane, and the side chain is inserted down into the membrane bilayer. The formation of a hydrogen-bonding interaction with menaquinol would neutralize the positive charge of this side chain and additionally suggests that this side chain is a

possible proton donor (45). Even a conservative mutation to arginine abolishes both menaquinol oxidation and ubiquinone reduction.

Evolution and similarity of SQR and QFR

As is described above, SQR and QFR share sequence similarity in the soluble domain, which suggests that they evolved from a gene duplication event. The strongest sequence similarity (58%) is observed in the flavoprotein subunit (A chain), which contains the active site for succinate-fumarate interconversion. The flavoprotein subunit also exhibits significant sequence and structural similarity to soluble fumarate reductases, as well as to L-aspartate oxidase in *E. coli*. These soluble counterparts lack a covalent bond to FAD and consequently lack succinate-oxidizing ability (8, 79, 81, 109). This suggests that fumarate reduction came about first, with the ability to oxidize succinate occurring later with the formation of a covalent bond to FAD. Sequence comparisons between mitochondrial SQR and eubacterial homologs predict that those lineages have an ancient common origin in α-proteobacteria (11, 101).

Evidence for an ancient evolutionary origin of complex II enzymes comes from sequence relationships between iron- sulfur protein subunits (subunit B) of different

42

species (14). The iron-sulfur protein subunit is related in sequence to ferredoxins (Fig. 12), evolutionarily ancient redox-active proteins present in prokaryotes, in mitochondria and chloroplasts of eukaryotes, and in archaea. This suggests that they may have been present in the last universal common ancestor (LUCA) as part of a diverse array of respiratory processes. The iron-sulfur protein subunit originally may have been a separate soluble protein that transferred electrons between divergent reductases and membrane-bound four-helix bundle cytochromes. Over time, the iron-sulfur protein developed affinity for the flavoprotein subunit, followed by the membrane-spanning subunits, leading to the current subunit arrangement. Sequence and cofactor differences in the integral membrane subunits (subunits C and D) place SQR and QFR into separate subclasses (32), and here the enzymes differ substantially. *E. coli* SQR contains two transmembrane polypeptide chains bound to a single heme. In contrast, *E. coli* QFR contains two transmembrane subunits but lacks heme (32, 34). Through evolution, the iron-sulfur protein may have bound various membrane subunits, explaining the current diversity of membrane subunits found in homologs of SQR and QFR.

Unanswered questions

One unanswered question revolves around whether small- and large-scale protein movements are required for succinate- fumarate interconversion. Domain rearrangements around the flavin cofactor may provide some catalytic control in the flavoprotein subunit. The flavoprotein subunits of SQR and QFR, along with soluble fumarate reductases, contain several conserved residues near the active site that

do not directly interact with the substrate. Furthermore, the conformation of two domains enclosing the active site is altered in many of the structures, which may be relevant to fumarate/succinate interconversion by coercing the molecules into a transition state and may also prevent access of water or oxygen to the active site during the formation of the transition state. The existence and importance of domain movements have been called into question since the introduction of a disulfide bond between domains, which theoretically restricts interdomain motions, does not completely abolish enzyme activity in soluble fumarate reductases (93). Furthermore, little evidence exists for how FAD is reprotonated during the active cycle or how the structure of FAD changes between oxidation and reduction.

Quinone chemistry in SQR and QFR is also an area of active interest. No well-established mechanism exists for quinone reduction in SQR or quinol oxidation in QFR. The role of the heme in electron transfer reactions in SQR and other complex II homologs remains to be established as well. Furthermore, QFR is a much more potent producer of the superoxide than is SQR, yet differences in how these enzymes produce ROS (and under what conditions) remain unknown. Higher SQR cofactor potentials and the presence of a heme may shift electrons away from FAD, the known site of ROS production in QFR.

References

1.   Ackrell, B. A. C., B. Cochran, and G. Cecchini. 1989. Interactions of
        Oxaloacetate with Escherichia-Coli Fumarate Reductase. Archives of
        Biochemistry and Biophysics 268:26-34.

2.   Ackrell, B. A. C., E. B. Kearney, and M. Mayr. 1974. Studies on Succinate-
        Dehydrogenase .24. Role of Oxalacetate in Regulation of Mammalian
        Succinate-Dehydrogenase. Journal of Biological Chemistry 249:2021-2027.

3.   Anderson, R. F., R. Hille, S. S. Shinde, and G. Cecchini. 2005. Electron
        transfer within complex II - Succinate : Ubiquinone oxidoreductase of
        Escherichia coli. Journal of Biological Chemistry 280:33331-33337.

4.   Beinert, H. 2002. Spectroscopy of succinate dehydrogenases, a historical
        perspective. Biochimica Et Biophysica Acta-Bioenergetics 1553:7-22.

5.   Beinert, H., B. A. C. Ackrell, E. B. Kearney, and T. P. Singer. 1974. Epr
        Studies on Mechanism of Action of Succinate-Dehydrogenase in Activated
        Preparations. Biochemical and Biophysical Research Communications
        58:564-572.

6.   Beinert, H., and R. H. Sands. 1960. Studies on succinic and DPNH
        dehydrogenase preparations by paramagnetic resonance (EPR)
        spectroscopy. Biochemical and Biophysical Research Communications 3:41-
        46.

7.   Besteiro, S., M. Biran, N. Biteau, V. Coustou, T. Baltz, P. Canioni, and F.
        Bringaud. 2002. Succinate secreted by Trypanosoma brucei is produced by a

novel and unique glycosomal enzyme, NADH-dependent fumarate reductase. Journal of Biological Chemistry 277:38001-38012.

8.   Birch-Machin, M. A., R. W. Taylor, B. Cochran, B. A. C. Ackrell, and D. M. Turnbull. 2000. Late-onset optic atrophy, ataxia, and myopathy associated with a mutation of a complex II gene. Annals of Neurology 48:330-335.

9.   Blaut, M., K. Whittaker, A. Valdovinos, B. A. C. Ackrell, R. P. Gunsalus, and G. Cecchini. 1989. Fumarate Reductase Mutants of Escherichia-Coli That Lack Covalently Bound Flavin. Journal of Biological Chemistry 264:13599-13604.

10.   Burger, G., B. F. Lang, M. Reith, and M. W. Gray. 1996. Genes encoding the same three subunits of respiratory complex II are present in the mitochondrial DNA of two phylogenetically distant eukaryotes. Proceedings of the National Academy of Sciences of the United States of America 93:2328-2332.

11.   Calhoun, M. W., K. L. Oden, R. B. Gennis, M. J. T. Demattos, and O. M. Neijssel. 1993. Energetic Efficiency of Escherichia-Coli - Effects of Mutations in Components of the Aerobic Respiratory-Chain. Journal of Bacteriology 175:3020-3025.

12.   Campbell, L. L., and J. R. Postgate. 1965. Classification of Spore-Forming Sulfate-Reducing Bacteria. Bacteriological Reviews 29:359-&.

13.   Castresana, J., and M. Saraste. 1995. Evolution of Energetic Metabolism - the Respiration-Early Hypothesis. Trends in Biochemical Sciences 20:443-448.

14.   Cecchini, G., I. Schroder, R. P. Gunsalus, and E. Maklashina. 2002. Succinate dehydrogenase and fumarate reductase from Escherichia coli. Biochimica Et Biophysica Acta-Bioenergetics 1553:140-157.

15.   Cecchini, G., V. Yankovskaya, Y. Sher, and E. Maklashina. 2002. Structural insights into the function and physiology of complex II. p. 757-766. In S.Chapman, R. Perham, N.S. Scrutton (eds.) Flavins and Flavoproteins. Rudolf Wever, Berline, Germany.

16.   Cheng, V. W. T., E. Ma, Z. Zhao, R. A. Rothery, and J. H. Weiner. 2006. The iron-sulfur clusters in Escherichia coli succinate dehydrogenase direct electron flow. Journal of Biological Chemistry 281:27662-27668.

17.   Chirino, A. J., E. J. Lous, M. Huber, J. P. Allen, C. C. Schenck, M. L. Paddock, G. Feher, and D. C. Rees. 1994. Crystallographic Analyses of Site-Directed Mutants of the Photosynthetic Reaction-Center from Rhodobacter-Sphaeroides. Biochemistry 33:4584-4593.

18.   Cole, S. T. 1982. Nucleotide-Sequence Coding for the Flavoprotein Subunit of the Fumarate Reductase of Escherichia-Coli. European Journal of Biochemistry 122:479-484.

19.   Cole, S. T., T. Grundstrom, B. Jaurin, J. J. Robinson, and J. H. Weiner. 1982. Location and Nucleotide-Sequence of Frdb, the Gene Coding for the Iron-Sulfur Protein Subunit of the Fumarate Reductase of Escherichia-Coli. European Journal of Biochemistry 126:211-216.

20. Crouse, B. R., C. A. Yu, L. Yu, and M. K. Johnson. 1995. Spectroscopic Identification of the Axial Ligands of Cytochrome B(560) in Bovine Heart Succinate-Ubiquinone Reductase. Febs Letters 367:1-4.

21. Darlison, M. G., and J. R. Guest. 1984. Nucleotide-Sequence Encoding the Iron Sulfur Protein Subunit of the Succinate-Dehydrogenase of Escherichia-Coli. Biochemical Journal 223:507-517.

22. Doherty, M. K., S. L. Pealing, C. S. Miles, R. Moysey, P. Taylor, M. D. Walkinshaw, G. A. Reid, and S. K. Chapman. 2000. Identification of the active site acid/base catalyst in a bacterial fumarate reductase: A kinetic and crystallographic study. Biochemistry 39:10695-10701.

23. Edmondson, D. E., and P. Newton-Vinson. 2001. The covalent FAD of monoamine oxidase: Structural and functional role and mechanism of the flavinylation reaction. Antioxidants & Redox Signaling 3:789-806.

24. Efimov, I., C. N. Cronin, and W. S. McIntire. 2001. Effects of noncovalent and covalent FAD binding on the redox and catalytic properties of p-cresol methylhydroxylase. Biochemistry 40:2155-2166.

25. Engst, S., V. Kuusk, I. Efimov, C. N. Cronin, and W. S. McIntire. 1999. Properties of p-cresol methylhydroxylase flavoprotein overproduced by Escherichia coli. Biochemistry 38:16620-16628.

26. Guest, J. R. 1981. Partial Replacement of Succinate-Dehydrogenase Function by Phage-Specified and Plasmid-Specified Fumarate Reductase in Escherichia-Coli. Journal of General Microbiology 122:171-179.

27. Hagerhall, C. 1997. Succinate: Quinone oxidoreductases - Variations on a conserved theme. Biochimica Et Biophysica Acta-Bioenergetics 1320:107-141.

28. Hagerhall, C., S. Magnitsky, V. D. Sled, I. Schroder, R. P. Gunsalus, G. Cecchini, and T. Ohnishi. 1999. An Escherichia coli mutant quinol : fumarate reductase contains an EPR-detectable semiquinone stabilized at the proximal quinone-binding site. Journal of Biological Chemistry 274:26157-26164.

29. Hederstedt, L. 1999. Bioenergetics - Respiration without O-2. Science 284:1941-1942.

30. Hirsch, C. A., M. Rasminsky, B. D. Davis, and E. C. C. Lin. 1963. A fumarate reductase in Escherichia coli distinct form succinate dehydrogenase. Journal of Biological Chemistry 238:3770-3780.

31. Horsefield, R., V. Yankovskaya, G. Sexton, W. Whittingham, K. Shiomi, S. Omura, B. Byrne, G. Cecchini, and S. Iwata. 2006. Structural and computational analysis of the quinone-binding site of complex II (succinate-ubiquinone oxidoreductase) - A mechanism of electron transfer and proton conduction during ubiquinone reduction. Journal of Biological Chemistry 281:7309-7316.

32. Hudson, J. M., K. Heffron, V. Kotlyar, Y. Sher, E. Maklashina, G. Cecchini, and F. A. Armstrong. 2005. Electron transfer and catalytic control by the iron-sulfur clusters in a respiratory enzyme, E. coli fumarate reductase. Journal of the American Chemical Society 127:6977-6989.

33. Imlay, J. A. 1995. A Metabolic Enzyme That Rapidly Produces Superoxide, Fumarate Reductase of Escherichia-Coli. Journal of Biological Chemistry 270:19767-19777.

34. Inderlie, C. B., and E. A. Delwiche. 1973. Nitrate Reduction and Growth of Veillonella-Alcalescens. Journal of Bacteriology 114:1206-1212.

35. Ishimoto, M., M. Umeyama, and S. Chiba. 1974. Alteration of Fermentation Products from Butyrate to Acetate by Nitrate Reduction in Clostridium-Perfringens. Zeitschrift Fur Allgemeine Mikrobiologie 14:115-121.

36. Iuchi, S., T. Fujiwara, and E. C. C. Lin. 1990. The Arcb Gene of Escherichia-Coli Encodes a Sensor-Regulator Protein for Anaerobic Repression of the Arc Modulon. Molecular Microbiology 4:715-727.

37. Iuchi, S., and E. C. C. Lin. 1988. Arca (Dye), a Global Regulatory Gene in Escherichia-Coli Mediating Repression of Enzymes in Aerobic Pathways. Proceedings of the National Academy of Sciences of the United States of America 85:1888-1892.

38. Iverson, T. M., C. Luna-Chavez, G. Cecchini, and D. C. Rees. 1999. Structure of the Escherichia coli fumarate reductase respiratory complex, p. 1961-1966, Science, vol. 284.

39. Iverson, T. M., C. Luna-Chavez, L. R. Croal, G. Cecchini, and D. C. Rees. 2002. Crystallographic studies of the Escherichia coli quinol-fumarate reductase with inhibitors bound to the quinol-binding site. Journal of Biological Chemistry 277:16124-16130.

40. Johnson, M. K., J. E. Morningstar, G. Cecchini, and B. A. C. Ackrell. 1985. Detection of a Tetranuclear Iron-Sulfur Center in Fumarate Reductase from Escherichia-Coli by Electron-Paramagnetic Resonance Spectroscopy. Biochemical and Biophysical Research Communications 131:756-762.

41. Johnson, M. K., J. E. Morningstar, G. Cecchini, and B. A. C. Ackrell. 1985. In vivo Detection of a 3 Iron Cluster in Fumarate Reductase from Escherichia-Coli. Biochemical and Biophysical Research Communications 131:653-658.

42. Jones, H. M., and R. P. Gunsalus. 1985. Transcription of the Escherichia-Coli Fumarate Reductase Genes (Frdabcd) and Their Coordinate Regulation by Oxygen, Nitrate, and Fumarate. Journal of Bacteriology 164:1100-1109.

43. Jones, R. W. 1980. The Role of the Membrane-Bound Hydrogenase in the Energy-Conserving Oxidation of Molecular-Hydrogen by Escherichia-Coli. Biochemical Journal 188:345-350.

44. Kearney, E. B. 1960. Flavin Componant of the Mammalian Enzyme. Journal of Biological Chemistry 235:865-877.

45. Kita, K., C. R. T. Vibat, S. Meinhardt, J. R. Guest, and R. B. Gennis. 1989. One-Step Purification from Escherichia-Coli of Complex-Ii (Succinate - Ubiquinone Oxidoreductase) Associated with Succinate-Reducible Cytochrome-B556. Journal of Biological Chemistry 264:2672-2677.

46. Kowal, A. T., M. T. Werth, A. Manodori, G. Cecchini, I. Schroder, R. P. Gunsalus, and M. K. Johnson. 1995. Effect of Cysteine to Serine Mutations on the Properties of the [4fe-4s] Center in Escherichia-Coli Fumarate Reductase. Biochemistry 34:12284-12293.

47.   Kroger, A., S. Biel, J. Simon, R. Gross, G. Unden, and C. R. D. Lancaster. 2002. Fumarate respiration of Wolinella succinogenes: enzymology, energetics and coupling mechanism. Biochimica Et Biophysica Acta-Bioenergetics 1553:23-38.

48.   Lambden, P. R., and J. R. Guest. 1976. Mutants of Escherichia-Coli-K12 Unable to Use Fumarate as an Anaerobic Electron-Acceptor. Journal of General Microbiology 97:145-160.

49.   Lancaster, C. R. D. 2003. Wolinella succinogenes quinol : fumarate reductase and its comparison to E-coli succinate : quinone reductase. Febs Letters 555:21-28.

50.   Lancaster, C. R. D., R. Gross, and J. Simon. 2001. A third crystal form of Wolinella succinogenes quinol : fumarate reductase reveals domain closure at the site of fumarate reduction. European Journal of Biochemistry 268:1820-1827.

51.   Lancaster, C. R. D., A. H. Haas, M. G. Madej, and M. Mileni. 2006. Recent progress on obtaining theoretical and experimental support for the "E-pathway hypothesis" of coupled transmembrane electron and proton transfer in dihaem-containing quinol : fumarate reductase. Biochimica Et Biophysica Acta-Bioenergetics 1757:988-995.

52.   Lancaster, C. R. D., A. Kroger, M. Auer, and H. Michel. 1999. Structure of fumarate reductase from Wolinella succinogenes at 2.2 angstrom resolution. Nature 402:377-385.

53.   Lazazzera, B. A., D. M. Bates, and P. J. Kiley. 1993. The Activity of the Escherichia-Coli Transcription Factor Fnr Is Regulated by a Change in Oligomeric State. Genes & Development 7:1993-2005.

54.   Lee, G. Y., D. Y. He, L. Yu, and C. A. Yu. 1995. Identification of the Ubiquinone-Binding Domain in Qps1 of Succinate-Ubiquinone Reductase. Journal of Biological Chemistry 270:6193-6198.

55.   Lemire, B. D., J. J. Robinson, and J. H. Weiner. 1982. Identification of Membrane Anchor Polypeptides of Escherichia-Coli Fumarate Reductase. Journal of Bacteriology 152:1126-1131.

56.   Lucas, M. F., and M. J. Ramos. 2006. Mechanism of a soluble fumarate reductase from Shewanella frigidimarina: A theoretical study. Journal of Physical Chemistry B 110:10550-10556.

57.   Madej, M. G., H. R. Nasiri, N. S. Hilgendorff, H. Schwalbe, G. Unden, and C. R. D. Lancaster. 2006. Experimental evidence for proton motive force-dependent catalysis by the diheme-containing succinate: Menaquinone oxidoreductase from the gram-positive bacterium Bacillus licheniformis. Biochemistry 45:15049-15055.

58.   Maklashina, E., D. K. Berthold, and G. Cecchini. 1998. Anaerobic expression of Escherichia coli succinate dehydrogenase: Functional replacement of fumarate reductase in the respiratory chain during anaerobic growth. Journal of Bacteriology 180:5989-5996.

59.   Maklashina, E., and G. Cecchini. 1999. Comparison of catalytic activity and inhibitors of quinone reactions of succinate dehydrogenase (succinate-

ubiquinone oxidoreductase) and fumarate reductase (menaquinol-fumarate oxidoreductase) from Escherichia coli. Archives of Biochemistry and Biophysics 369:223-232.

60.   Maklashina, E., P. Hellwig, R. A. Rothery, V. Kotlyar, Y. Sher, J. H. Weiner, and G. Cecchini. 2006. Differences in protonation of ubiquinone and menaquinone in fumarate reductase from Escherichia coli. Journal of Biological Chemistry 281:26655-26664.

61.   Maklashina, E., T. M. Iverson, Y. Sher, V. Kotlyar, J. Andrell, O. Mirza, J. M. Hudson, F. A. Armstrong, R. A. Rothery, J. H. Weiner, and G. Cecchini. 2006. Fumarate reductase and succinate oxidase activity of Escherichia coli complex II homologs are perturbed differently by mutation of the flavin binding domain. Journal of Biological Chemistry 281:11357-11365.

62.   Maklashina, E., R. A. Rothery, J. H. Weiner, and G. Cecchini. 2001. Retention of heme in axial ligand mutants of succinate-ubiquinone oxidoreductase (complex II) from Escherichia coli. Journal of Biological Chemistry 276:18968-18976.

63.   Massey, V., and T. P. Singer. 1957. Studies on succinic dehydrogenase. III. The fumaric reducatase acitvity of succinic dehydrogenase. Journal of Biological Chemistry 228:263-274.

64.   Matsson, M., D. Tolstoy, R. Aasa, and L. Hederstedt. 2000. The distal heme center in Bacillus subtilis Succinate: Quinone reductase is crucial for electron transfer to menaquinone. Biochemistry 39:8617-8624.

65.   Messner, K. R., and J. A. Imlay. 2002. Mechanism of superoxide and hydrogen peroxide formation by fumarate reductase, succinate dehydrogenase, and aspartate oxidase. Journal of Biological Chemistry 277:42563-42571.

66.   Mewies, M., W. S. McIntire, and N. S. Scrutton. 1998. Covalent attachment of flavin adenine dinucleotide (FAD) and flavin mononucleotide (FMN) to enzymes: The current state of affairs. Protein Science 7:7-20.

67.   Miki, K., and E. C. C. Lin. 1973. Enzyme Complex Which Couples Glycerol-3-Phosphate Dehydrogenation to Fumarate Reduction in Escherichia-Coli. Journal of Bacteriology 114:767-771.

68.   Mitchell, P. 1961. Coupling of Phosphorylation to Electron and Hydrogen Transfer by a Chemi-Osmotic Type of Mechanism. Nature 191:144-148.

69.   Morningstar, J. E., M. K. Johnson, G. Cecchini, B. A. C. Ackrell, and E. B. Kearney. 1985. The High-Potential Iron-Sulfur Center in Escherichia-Coli Fumarate Reductase Is a 3-Iron Cluster. Journal of Biological Chemistry 260:3631-3638.

70.   Morris, C. J., A. C. Black, S. L. Pealing, F. D. C. Manson, S. K. Chapman, G. A. Reid, D. M. Gibson, and F. B. Ward. 1994. Purification and Properties of a Novel Cytochrome - Flavocytochrome-C from Shewanella-Putrefaciens. Biochemical Journal 302:587-593.

71.   Mowat, C. G., K. L. Pankhurst, C. S. Miles, D. Leys, M. D. Walkinshaw, G. A. Reid, and S. K. Chapman. 2002. Engineering water to act as an active site acid catalyst in a soluble fumarate reductase. Biochemistry 41:11990-11996.

72.	Muratsubaki, H., and T. Katsume. 1985. Characterization of Fumarate Reductase from Bakers-Yeast - Essential Sulfhydryl-Group for Binding of Fad. Journal of Biochemistry 97:1201-1209.

73.	Nakamura, K., M. Yamaki, M. Sarada, S. Nakayama, C. R. T. Vibat, R. B. Gennis, T. Nakayashiki, H. Inokuchi, S. Kojima, and K. Kita. 1996. Two hydrophobic subunits are essential for the heme b ligation and functional assembly of complex II (succinate-ubiquinone oxidoreductase) from Escherichia coli. Journal of Biological Chemistry 271:521-527.

74.	Ohnishi, T. 1975. Thermodynamic and Epr Characterization of Iron-Sulfur Centers in Nadh-Ubiquinone Segment of Mitochondrial Respiratory-Chain in Pigeon Heart. Biochimica Et Biophysica Acta 387:475-490.

75.	Ohnishi, T., C. C. Moser, C. C. Page, P. L. Dutton, and T. Yano. 2000. Simple redox-linked proton-transfer design: new insights from structures of quinol-fumarate reductase. Structure 8:R23-R32.

76.	Ohnishi, T., D. B. Winter, T. E. King, and J. Lim. 1974. Epr Studies on a Hipip Type Iron-Sulfur Center in Succinate-Dehydrogenase Segment of Respiratory-Chain. Biochemical and Biophysical Research Communications 61:1017-1025.

77.	Page, C. C., C. C. Moser, X. X. Chen, and P. L. Dutton. 1999. Natural engineering principles of electron tunnelling in biological oxidation-reduction. Nature 402:47-52.

78.   Pankhurst, K. L., C. G. Mowat, C. S. Miles, D. Leys, M. D. Walkinshaw, G. A. Reid, and S. K. Chapman. 2002. Role of His505 in the soluble fumarate reductase from Shewanella frigidimarina. Biochemistry 41:8551-8556.

79.   Pealing, S. L., A. C. Black, F. D. C. Manson, F. B. Ward, S. K. Chapman, and G. A. Reid. 1993. Sequence of the Gene Encoding Flavocytochrome-C from Shewanella-Putrefaciens - a Tetraheme Flavoenzyme That Is a Soluble Fumarate Reductase Related to the Membrane-Bound Enzymes from Other Bacteria (Vol 31, Pg 12132, 1992). Biochemistry 32:3829-3829.

80.   Pershad, H. R., J. Hirst, B. Cochran, B. A. C. Ackrell, and F. A. Armstrong. 1999. Voltammetric studies of bidirectional catalytic electron transport in Escherichia coli succinate dehydrogenase: comparison with the enzyme from beef heart mitochondria. Biochimica Et Biophysica Acta-Bioenergetics 1412:262-272.

81.   Peterson, J., C. Vibat, and R. B. Gennis. 1994. Identification of the Axial Heme Ligands of Cytochrome B(556) in Succinate - Ubiquinone Oxidoreductase from Escherichia-Coli. Febs Letters 355:155-156.

82.   Puustinen, A., M. Finel, T. Haltia, R. B. Gennis, and M. Wikstrom. 1991. Properties of the 2 Terminal Oxidases of Escherichia-Coli. Biochemistry 30:3936-3942.

83.   Reid, G. A., C. S. Miles, R. K. Moysey, K. L. Pankhurst, and S. K. Chapman. 2000. Catalysis in fumarate reductase. Biochimica Et Biophysica Acta-Bioenergetics 1459:310-315.

84. Rothery, E. L., C. G. Mowat, C. S. Miles, S. Mott, M. D. Walkinshaw, G. A. Reid, and S. K. Chapman. 2004. Probing domain mobility in a flavocytochrome. Biochemistry 43:4983-4989.

85. Ruzicka, F. J., H. Beinert, K. L. Schepler, W. R. Dunham, and R. H. Sands. 1975. Interaction of Ubisemiquinone with a Paramagnetic Component in Heart Tissue. Proceedings of the National Academy of Sciences of the United States of America 72:2886-2890.

86. Salmon, K., S. P. Hung, K. Mekjian, P. Baldi, G. W. Hatfield, and R. P. Gunsalus. 2003. Global gene expression profiling in Escherichia coli K12 - The effects of oxygen availability and FNR. Journal of Biological Chemistry 278:29837-29855.

87. Salmon, K. A., S. Hung, N. R. Steffen, R. Krupp, P. Baldi, G. W. Hatfield, and R. P. Gunsalus. 2005. Global gene expression profiling in Escherichia coli K12 - Effects of oxygen availability and ArcA. Journal of Biological Chemistry 280:15084-15096.

88. Schirawski, J., and G. Unden. 1998. Menaquinone-dependent succinate dehydrogenase of bacteria catalyzes reversed electron transport driven by the proton potential. European Journal of Biochemistry 257:210-215.

89. Schmitz, R. A., S. Achebach, and G. Unden. 2004. Analysis of fumarate nitrate reductase regulator as an oxygen sensor in Escherichia coli, p. 628-644, Oxygen Sensing, vol. 381.

90. Schnarrenberger, C., and W. Martin. 2002. Evolution of the enzymes of the citric acid cycle and the glyoxylate cycle of higher plants - A case study of endosymbiotic gene transfer. European Journal of Biochemistry 269:868-883.

91. Schultz, B. E., and S. I. Chan. 2001. Structures and proton-pumping strategies of mitochondrial respiratory enzymes. Annual Review of Biophysics and Biomolecular Structure 30:23-65.

92. Shenoy, S. K., L. Yu, and C. A. Yu. 1997. The smallest membrane anchoring subunit (QPs3) of bovine heart mitochondrial succinate-ubiquinone reductase - Cloning, sequencing, topology, and Q-binding domain. Journal of Biological Chemistry 272:17867-17872.

93. Singer, T. P., E. B. Kearney, and P. Bernath. 1956. Studies on succinic dehydrogenase. II. Isolation and properties of the dehydrogenase from beef heart. Journal of Biological Chemistry 223.

94. Sucheta, A., B. A. C. Ackrell, B. Cochran, and F. A. Armstrong. 1992. Diode-Like Behavior of a Mitochondrial Electron-Transport Enzyme. Nature 356:361-362.

95. Sun, F., X. Huo, Y. J. Zhai, A. J. Wang, J. X. Xu, D. Su, M. Bartlam, and Z. H. Rao. 2005. Crystal structure of mitochondrial respiratory membrane protein complex II. Cell 121:1043-1057.

96. Taylor, P., S. L. Pealing, G. A. Reid, S. K. Chapman, and M. D. Walkinshaw. 1999. Structural and mechanistic mapping of a unique fumarate reductase. Nature Structural Biology 6:1108-1112.

97.   Thauer, R. K., K. Jungermann, and K. Decker. 1977. Energy-Conservation in Chemotropic Anaerobic Bacteria. Bacteriological Reviews 41:100-180.

98.   Tisdale, H., J. Hauber, G. Prager, P. Turini, and T. P. Singer. 1968. Studies on Succinate Dehydrogenase .15. Isolation Molecular Properties and Isoenzymes of Fumarate Reductase. European Journal of Biochemistry 4:472-&.

99.   Tran, Q. M., R. A. Rothery, E. Maklashina, G. Cecchini, and J. H. Weiner. 2006. The quinone binding site in Escherichia coli succinate dehydrogenase is required for electron transfer to the heme b. Journal of Biological Chemistry 281:32310-32317.

100.   Turner, K. L., M. K. Doherty, H. A. Heering, F. A. Armstrong, G. A. Reid, and S. K. Chapman. 1999. Redox properties of flavocytochrome c(3) from Shewanella frigidimarina NCIMB400. Biochemistry 38:3302-3309.

101.   Wagner, G. C., R. J. Kassner, and M. D. Kamen. 1974. Redox Potentials of Certain Vitamins-K - Implications for a Role in Sulfite Reduction by Obligately Anaerobic Bacteria. Proceedings of the National Academy of Sciences of the United States of America 71:253-256.

102.   Walker, W. H., and T. P. Singer. 1970. Identification of Covalently Bound Flavin of Succinate Dehydrogenase as 8alpha-(Histidyl) Flavin Adenine Dinucleotide. Journal of Biological Chemistry 245:4224-&.

103.   Weiner, J. H., and P. Dickie. 1979. Fumarate Reductase of Escherichia-Coli - Elucidation of the Covalent-Flavin Component. Journal of Biological Chemistry 254:8590-8593.

104. Werth, M. T., H. Sices, G. Cecchini, I. Schroder, S. Lasage, R. P. Gunsalus, and M. K. Johnson. 1992. Evidence for Non-Cysteinyl Coordination of the [2fe-2s] Cluster in Escherichia-Coli Succinate-Dehydrogenase. Febs Letters 299:1-4.

105. Westenberg, D. J., R. P. Gunsalus, B. A. C. Ackrell, H. Sices, and G. Cecchini. 1993. Escherichia-Coli Fumarate Reductase Frdc and Frdd Mutants - Identification of Amino-Acid-Residues Involved in Catalytic Activity with Quinones. Journal of Biological Chemistry 268:815-822.

106. Wood, D., M. G. Darlison, R. J. Wilde, and J. R. Guest. 1984. Nucleotide-Sequence Encoding the Flavoprotein and Hydrophobic Subunits of the Succinate-Dehydrogenase of Escherichia-Coli. Biochemical Journal 222:519-534.

107. Yamamoto, I., and M. Ishimoto. 1977. Anaerobic Growth of Escherichia-Coli on Formate by Reduction of Nitrate, Fumarate, and Trimethylamine N-Oxide. Zeitschrift Fur Allgemeine Mikrobiologie 17:235-242.

108. Yankovskaya, V., R. Horsefield, S. Tornroth, C. Luna-Chavez, H. Miyoshi, C. Leger, B. Byrne, G. Cecchini, and S. Iwata. 2003. Architecture of succinate dehydrogenase and reactive oxygen species generation. Science 299:700-704.

109. Tisdale, H., J. Hauber, G. Prager, P. Turini, and T. P. Singer. 1968. Studies on succinate dehydrogenase. 15. Isolation, molecular properties, and isoenzymes of fumarate reductase. *Eur. J. Biochem.* 4:472–477

110. Tran, Q. H., J. Bongaerts, D. Vlad, and G. Unden. 1997. Requirement for the proton-pumping NADH dehydrogenase I of *Escherichia coli* in respiration of NADH to fumarate and its bioenergetic implications. *Eur. J. Biochem.* 244:155–160.

111. Tran, Q. M., R. A. Rothery, E. Maklashina, G. Cecchini, and J. H. Weiner. 2006. The quinone binding site in *Escherichia coli* succinate dehydrogenase is required for electron transfer to the heme *b*. *J. Biol. Chem.* 281:32310–32317.

112. Turner, K. L., M. K. Doherty, H. A. Heering, F. A. Armstrong, G. A. Reid, and S. K. Chapman. 1999. Redox properties of flavocytochrome c_3 from *Shewanella frigidimarina*. *Biochemistry* 38:3302–3309.

113. Wagner, G. C., R. J. Kassner, and M. D. Kamen. 1974. Redox potentials of certain vitamins K: implications for a role in sulfite reduction by obligately anaerobic bacteria. *Proc. Natl. Acad. Sci. USA* 71:253–256.

114. Walker, W. H., and T. P. Singer. 1970. Identification of covalently bound flavin of succinate dehydrogenase as 8α-(histidyl) flavin adenine dinucleotide. *J. Biol. Chem.* 245:4224–4225.

115. Weidner, U., S. Geier, A. Ptock, T. Friedrich, H. Leif, and H. Weiss. 1993. The gene locus of the proton translocating NADH:ubiquinone oxidoreductase in *Escherichia coli*—organization of the fourteen genes and relationship between the derived proteins and subunits of mitochondrial complex I. *J. Mol. Biol.* 233:109–122.

116. Weiner, J. H., and P. Dickie. 1979. Fumarate reductase of *Escherichia coli*: elucidation of the covalent flavin component. *J. Biol. Chem.* 254:8590–8593.

117. Werth, M. T., H. Sices, G. Cecchini, I. Schröder, S. Lasage, R. P. Gunsalus, and M. K. Johnson. 1992. Evidence for non-cysteinyl coordination of the [2Fe-2S] cluster in *Escherichia coli* succinate dehydrogenase. *FEBS Lett.* 299:1–4.

118. Westenberg, D. J., R. P. Gunsalus, B. A. C. Ackrell, H. Sices, and G. Cecchini. 1993. *Escherichia coli* fumarate reductase *frdC* and *frdD* mutants— identification of amino acid residues involved in catalytic activity with quinones. *J. Biol. Chem.* 268:815–822.

119. Wood, D., M. G. Darlison, R. J. Wilde, and J. R. Guest. 1984. Nucleotide sequence encoding the flavoprotein and hydrophobic subunits of the succinate dehydrogenase of *Escherichia coli*. *Biochem. J.* 222:519–534.

120. Yamamoto, I., and M. Ishimoto. 1977. Anaerobic growth of *Escherichia coli* on formate by reduction of nitrate, fumarate, and trimethylamine N-oxide. *Z. Allg. Mikrobiol.* 17:235–242.

121. Yankovskaya, V., R. Horsefield, S. Tornroth, C. Luna-Chavez, H. Miyoshi, C. Leger, B. Byrne, G. Cecchini, and S. Iwata. 2003. Architecture of succinate dehydrogenase and reactive oxygen species generation. *Science* 299:700–704.

CHAPTER II

A THREONINE ON THE ACTIVE SITE LOOP CONTROLS TRANSITION
STATE FORMATION IN *ESCHERICHIA COLI* RESPIRATORY COMPLEX II[1]

Abstract

In *Escherichia coli*, the complex II superfamily members succinate:ubiquinone oxidoreductase (SQR) and quinol:fumarate reductase (QFR) participate in aerobic and anaerobic respiration, respectively. Complex II enzymes catalyze succinate and fumarate interconversion at the interface of two domains of the soluble flavoprotein subunit, the FAD binding domain and the capping domain. An 11-amino acid loop in the capping domain (Thr-A234 to Thr-A244 in quinol:fumarate reductase) begins at the interdomain hinge and covers the active site. Amino acids of this loop interact with both the substrate and a proton shuttle, potentially coordinating substrate binding and the proton shut- tle protonation state. To assess the loop's role in catalysis, two threonine residues were mutated to alanine: QFR Thr-A244 (act-T; Thr-A254 in SQR), which hydrogen-bonds to the sub- strate at the active site, and QFR Thr-A234 (hinge-T; Thr-A244 in SQR), which is located at the hinge and hydrogen-bonds the proton shuttle. Both mutations impair catalysis and decrease substrate binding. The crystal structure of the hinge-T

mutation reveals a reorientation between the FAD-binding and capping domains that accompanies proton shuttle alteration. Taken together, hydrogen bonding from act-T to substrate may coordinate with interdomain motions to twist the double bond of fumarate and introduce the strain important for attaining the transition state.

Introduction

Complex II superfamily members catalyze two distinct capacity, complex II links the citric acid cycle to the electron transfer chain. The two reactions are coupled, since electrons that are the product of one reaction are transferred through the complex II enzyme to become the reactant of the second reaction. Homologues of complex II that preferentially oxidize succinate and reduce quinone participate in aerobic respiration are known as succinate:ubiquinone oxidoreductases (SQR; SdhCDAB). By contrast, those homologues that preferentially reduce fumarate and oxidize quinol are known as quinol:fumarate reductases (QFR; FrdABCD) and participate in bacterial anaerobic respiration with fumarate as the terminal electron acceptor.

Complex II enzymes contain four polypeptide chains, two of which, the flavoprotein (FrdA; SdhA) and the iron protein (FrdB; SdhB), are soluble subunits and two of which span the membrane (FrdCD; SdhCD) (2). Succinate and fumarate inter- conversion occurs in the flavoprotein, whereas quinol and qui- none interconversion occurs in the membrane-spanning region of the protein. In addition to the integral-membrane complex II homologues, there are known soluble homologues of the flavoprotein that only catalyze dicarboxylate oxidoreduction

without coupling this reaction to quinone chemistry within the membrane.

Both the soluble and integral membrane homologues of complex II contain an FAD prosthetic group in the flavoprotein that performs hydride transfer during catalysis. In the membrane-bound forms of complex II, covalent binding of FAD raises its potential ($Em7 = \sim$-55 to -70 mV) and allows membrane-bound enzymes to proficiently oxidize succinate as well as reduce fumarate (3-6). In contrast, noncovalently bound FAD in the soluble bacterial homologues, such as flavocytochrome c3 (Fcc3) and l-aspartate oxidase, has a redox potential ~100 mV lower (~-150 mV) (7). As a result, these soluble homologues cannot proficiently oxidize succinate (8-11).

X-ray structures from the complex II superfamily reveal that the active site for dicarboxylate oxidoreduction shares a common architecture with absolutely conserved catalytic residues (1, 2, 8-17). Like its eukaryotic and prokaryotic counterparts, the flavoprotein subunit of Escherichia coli SQR and QFR comprises two domains (i.e. an FAD-binding domain and a capping domain) with the active site at the domain interface. A short hinge region connects these two domains (Fig. 18A; residues 231-234 and 351-353 of the QFR flavoprotein subunit).
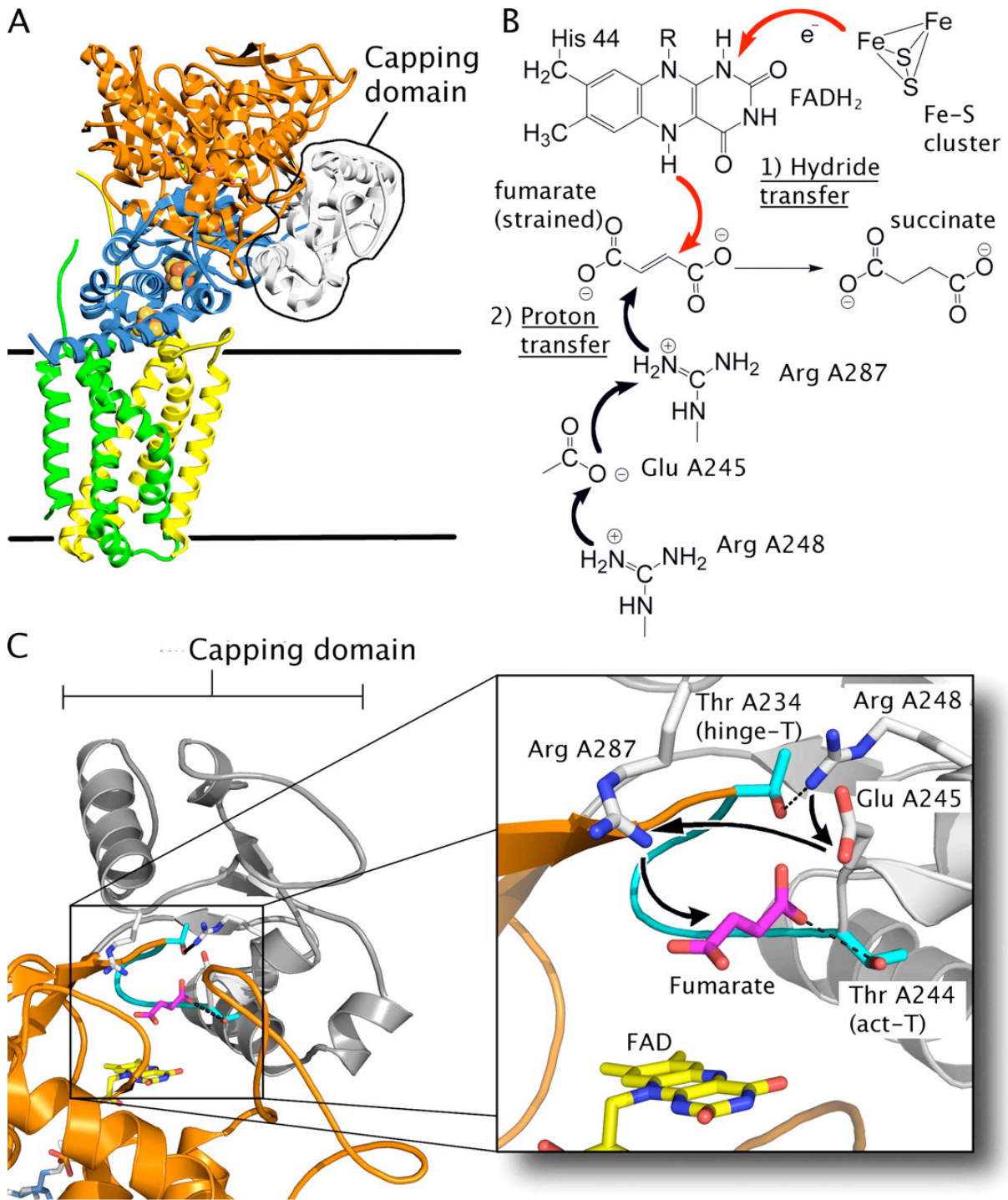
Fig. 18. Overview of active site architecture and the fumarate reduction reaction mechanism in complex II enzymes. *A.* The overall architecture of wild type *E. coli* QFR (PDBID 1KF6) is shown in relation to the membrane. The FrdA subunit (orange) is shown with the capping domain (grey) circled. The FrdB (blue), FrdC (green) and FrdD (yellow) subunits are shown as ribbons, with iron-sulfur clusters of the FrdB subunit shown as spheres. *B.* In QFR and soluble fumarate reductases, fumarate reduction is believed to occur in two distinct steps. The first is hydride transfer from reduced FAD and the second is proton transfer from Arg A287. Electron transfer and hydride transfer are displayed as red arrows and all proton transfer steps are shown with black arrows. Reprotonation of the Arg A287 side chain is achieved through a shuttle comprising Glu A245 and Arg A248. While re-reduction of the FAD requires two electrons that are transferred from iron-sulfur clusters in the iron protein subunit protein, the pathway for re-protonation of the FAD has not been elucidated. *C.* The QFR active site is located in the flavoprotein (FrdA) at the interface between the FAD binding domain (orange) and the capping domain (grey). The active site loop (cyan) contains both proton shuttling residues and substrate binding residues. Nitrogen atoms are colored blue, oxygen colored red, FAD carbons are yellow, and fumarate carbons are magenta. Side chain carbons are colored grey for Arg A245, Arg A248, and Arg A287; side chain carbons for act-T and hinge-T are colored cyan. The location of fumarate in the active site is from an unpublished structure. Black arrows indicate the direction of proton transfer through the proton shuttle during fumarate reduction.

The FAD-binding and capping domains can assume any of a continuum of interdomain angles without distortion of the fold of either domain (2, 8-11, 18-23). These flavoprotein structures can be categorized into three groups, depending on interdomain orientation (19): domains "closed" over the active site (16, 18, 19, 22), domains rotated into an "open" position for solvent access into the active site (8, 9), and an "intermediate" position (10, 11, 20, 21, 23). Although all of the structures in the open state lack bound dicarboxylate at the active site (8, 9), there has also been a structure of a dicarboxylate-free active site in the closed position (16). In general, the majority of structures with ligand bound into the active site are in closed or intermediate positions that are nearly closed. The flavoproteins of both the Wolinella succinogenes QFR (20, 22) and the soluble Fcc3 flavoproteins (9, 10) have been observed with different domain angles in different crystal forms, suggesting that crystal packing forces can alter the interdomain angle and reflect the flexibility between these domains. The physiological significance of interdomain flexibility in the complex II superfamily is debated (24), and there is currently no known correlation between domain rotations and the catalysis. However, this type of interdomain movement has been suggested to control substrate access to the active site in a number of other flavoenzymes (25).

Intriguingly, the interdomain hinge between the FAD-binding and capping domains contains an absolutely conserved His-Pro-Thr motif that begins in an 11-amino acid loop (Fig. 19A) containing residues important for catalysis in QFR and SQR (Fig. 18B). This active site loop begins at the hinge with a threonine (Thr-A234 in the E. coli QFR, Thr-A244 in the E. coli SQR) denoted as the hinge-T. The loop

ends at a second threonine (Thr-A244 in E. coli QFR, Thr-A254 in the E. coli SQR) that forms a hydrogen-bonding interaction to the substrate in the active site and is denoted as act-T. The act-T hydrogen bond to substrate is particularly notable, since it may prime fumarate to accept hydride transfer from FAD, the first step in fumarate reduction by QFR. In solution, fumarate is a planar molecule constrained by a double bond (12); however, in complex II co-structures with fumarate, the O1 and O2 oxygen atoms are out of plane with the rest of the molecule (11, 20). The strain across the double bond of fumarate may facilitate hydride transfer from flavin N5 to fumarate C2 by stabilizing the transition state and lowering the transition state barrier (11, 12).

The second step of fumarate reduction in QFR, protonation of the intermediate carbanion, may be influenced by hinge-T (QFR Thr-A234), located at the end of the interdomain hinge and the beginning of the active site loop. The hinge-T side chain Oγ forms a hydrogen-bonding interaction with the side chain uanidine Nζ atom of Arg 248, which is a part of the proton shuttle that delivers a proton to the buried active site. This proton shuttle begins with Arg-A248, extends through Glu-A245, and ends with Arg-A287, which directly interacts with substrate (12, 26-29). In theory, the hydrogen-bonding interaction between the hinge-T Oγ and Arg-248 Nζ should lower the pKa of the arginine side chain and allow proton transfer at physiological pH values.

Materials and Methods

To further investigate the unique role of the active site loop in catalysis, the function of act-T (QFR Thr-A244; SQR Thr-A254) and hinge-T (QFR Thr-A234; SQR Thr-A244) was examined using alanine mutations in the E. coli QFR and SQR enzymes. Both mutants showed a loss of substrate binding and a loss of catalysis. Since the hinge-T does not interact directly with substrate, the basis for the loss of substrate binding in the hinge-T mutant QFR was evaluated using x-ray crystallography, which revealed that the absence of interpretable density for bound dicarboxylate resulted from a domain reorientation. The role of the hydrogen bonds provided by act-T and hinge-T are discussed for QFR and SQR, respectively. Bacterial Strains and Plasmids—E. coli strain DW35 (ΔfrdABCD, sdhC::kan), which was used as the host for expression of wild type and mutant forms of QFR and SQR, has been previously described (30). Plasmid pH3 (frdA+B+C+D+) was used for expression of wild type QFR (4), and plasmid pFAS (PFRDsdhC+D+A+B+) was used for expression of wild type SQR (31).

Mutagenesis—Mutation of individual amino acids was accomplished using the QuikChange (Stratagene, La Jolla, CA) site-directed mutagenesis kit. All mutations were verified by sequencing the HindIII-BstXI restriction fragment for SdhA mutations or the BstEII-ApaI fragment from FrdA. Mutagenized fragments were subcloned back into pFAS for SQR mutants or pH3 for QFR mutants. All cloning procedures were performed in accordance with methods previously described (4, 30, 31).

Growth Conditions and Enzyme Purification—E. coli DW35 harboring the appropriate plasmid was grown under microaerophilic conditions in Terrific Broth medium as previously described (32). Isolation of membrane fractions (33) and subsequent purification of QFR and SQR enzymes were performed according to previously published methods (31, 34). Protein concentration was measured by the bicinchoninic acid method (Pierce) with bovine serum albumin as a standard. FAD and heme content were determined as previously described (32).

Measurement of Enzyme Activity—To activate the enzymes, QFR and SQR were diluted to 5 mg of protein/ml in 30 mm BTP (BisTris-propane, pH 7.0), 0.1 mm EDTA, 0.05% Anapoe® C12E9 (Anatrace, Maumee, OH), 3 mm malonate and incubated for 20 min at 30 °C. For spectroscopic analysis, the enzymes were then concentrated with a Centriprep YM30 (Millipore) centrifugal filter device following the manufacturer's instructions and then passed through a PD-10 gel filtration column to remove malonate. Activated enzyme was then stored on ice for the duration of the experiment. The standard assay medium at 30 °C contained 50 mm BTP, 0.1 mm EDTA, 0.006% C12E9 with the pH adjusted to intervals of 6.0-9.4 as appropriate. Potassium ferricyanide and phenazine ethosulfate/2,6-dichlorophenol indophenol were used as electron acceptors for reactions of succinate oxidation for QFR and SQR, respectively (35). Fumarate reduction was determined with reduced methyl viologen or by menaquinol oxidation, as described previously (36). Optical spectra were recorded with an Agilent 8453 diode array spectrophotometer 1 min after the addition of ligand to an isolated enzyme in 30 mm BTP, 0.1 mm EDTA, 0.01% Anapoe C12E9.

Crystallization of QFR FrdA T234A—QFR FrdA T234A crystals were grown from protein purified by previously described methods for wild type enzyme (37) using the hanging drop vapor diffusion method in 10% polyethylene glycol 5000 monomethyl ether, 250 mm magnesium acetate, 100 mm citric acid, pH 5.8, and 0.1 mm EDTA at 22 °C with drop sizes of 1 µl. QFR crystals formed in the orthorhombic space group P212121 with unit cell dimensions a = 96.9 Å, b = 135.5 Å, and c = 266.0 Å with α = β = γ = 90° (Table 1).

Data Collection, Processing, and Model Refinement—Data were collected at beamline 11-1 at the Stanford Synchrotron Radiation Laboratories on crystals cryoprotected with 30% ethylene glycol using a wavelength of 1 Å on an ADSC detector at 100 K. Data were processed using DENZO, SCALEPACK (38), and the CCP4 (39) suite of programs. Since crystals were isomorphous with crystals from known structures of wild type QFR, rigid body refinement was performed with CNS (40) to obtain initial model phases. Maps were calculated with CCP4 (39), CNS (40), and PHENIX (41). Iterative rounds of model rebuilding were performed in O (42) and COOT (43), whereas refinement was performed with CNS (40) and PHENIX (41) with loose non crystallographic symmetry restraints.

Table 2. Crystallographic data collection, processing, and refinement

Wavelength (Å)	1.0
Resolution (Å)	3.65
Unit cell dimensions (Å)	a = 96.9 b = 135.5 c = 266.0
Space Group	$P2_12_12_1$
Observations (#)	76015
Unique (#)	32532
I/σ	9.52(2.5)
Completeness	80.3%
R_{sym} [1]	8.4%(39%)
R_{work} [2]	24.68%
R_{free} [3]	29.54%
$RMSD^4$ Bond lengths (Å)	0.019
$RMSD^4$ Bond angles (°)	1.92

1. R_{sym} = [____] , where [__] and [__] are the ith and mean measurements of the intensity of reflection hkl.

2. R_{cryst} = [____] , where [__] and [__] are the observed and calculated structure factors for the reflection hkl and k is a weighting factor.

3. R_{free} = [____] , where [__] and [__] are the observed and calculated structure factors for the reflection hkl and k is a weighing factor. T is the test set of reflections.

4. Root mean square deviation

Model building with omit maps was used to minimize map bias. Ab initio protein folding was performed with RAPPER (44). Final R-factors for the structures were R_{cryst} = 26.05% and R_{free} = 29.57% with reasonable geometry. Figures were created in the program PyMOL (45). The Dyndom server (39) was used to calculate the angle of domain motions between wild type QFR and hinge-T QFR.

Results

In this study, two conserved threonine residues have been mutated to alanine in QFR and SQR. The first of these, act-T (Thr-A244 in QFR; Thr-A254 in SQR), hydrogen-bonds to dicarboxylate substrates bound at the active site (10, 16, 18, 21, 23). The second conserved threonine residue studied, hinge-T (Thr-A234 in QFR; Thr-A244 in SQR) hydrogen-bonds to Arg-A248 in the proton shuttle and is at the hinge region connecting the capping and FAD domains.

Active Site Threonine Mutants—Wild type SQR oxidizes succinate with a high kcat of 110 s-1 (36); however, the SQR act-T mutant was incapable of succinate oxidation in the pH range of 6.0-9.0 tested. Moreover, heme b reduction was not observed upon prolonged incubation of the SQR act-T mutant with succinate, although wild type SQR heme b would be fully reduced under such conditions (data not shown). Similar to the SQR act-T mutant, the QFR act-T mutant (Thr-A244 → Ala) was unable to oxidize succinate. Fumarate reductase activity in the QFR act-T mutant fell by more than 800-fold compared with wild type (Table 2). The residual activity depended upon fumarate concentration, with the K_{fumm} being increased by 40-fold (Table 2). Thus, the QFR act-T mutation affected both kcat and K_m.

The act-T substitution resulted in dramatic changes in the ligand-induced optical properties of act-T-QFR and act-T-SQR (Fig. 19). The amplitude of the spectral peaks at 400 and 500 nm are reduced 3-4-fold in the mutant enzymes, and there is a loss of the characteristic charge transfer band in the presence of OAA (Fig. 19).

Succinate oxidation　　　　**Fumarate reduction**

pH
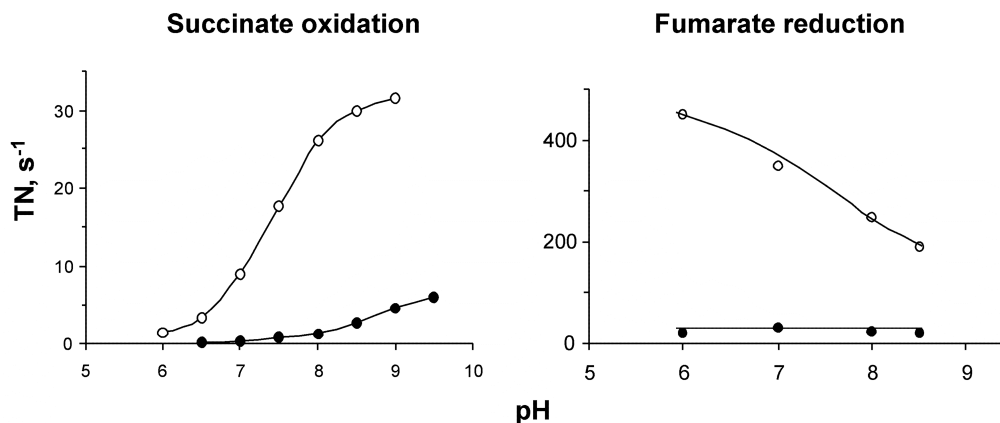
Figure 19. Dicarboxylate induced optical changes in SQR and QFR enzymes (pH 7.0, 25°C). Difference spectra represent the effect of malonate (green), fumarate (blue), and OAA (magenta) on the spectrum of fully oxidized enzymes. Dicarboxylates were used at saturating concentrations for optical spectra. For the wild type SQR and QFR the concentrations of ligands were 0.1 mM OAA, 1 mM malonate, 5 mM fumarate. For the SQR act-T and QFR act-T enzymes, the concentrations were 2 mM OAA, 10 mM malonate, 10 mM fumarate. The protein concentration in all cases was normalized to 4.9 μM for spectral analysis. Shown in the figure are representative spectra of 4 independent experiments.

These results are consistent with the observation that altered substrate binding prevents formation of the charge transfer complex and that both the QFR act-T and SQR act-T mutant enzymes are compromised in substrate binding (Table 3). This altered binding would preclude efficient catalysis.

Table 3. *Kinetic parameters of wild type and mutant QFR.*

	Fumarate reduction		Succinate oxidation		
	k_{cat} (s^{-1})	K_m^{fum} (mM)	k_{cat} (s^{-1})	K_m^{succ}(mM)	K_i^{OAA}(µM)
WT-QFR	340	0.02	30	0.55	0.3
AcT-QFR	0.4	0.8	<0.03	nd	nd
HingeT-QFR	26	0.6	1.3	2.7	40

All assays were done at 30 ^{0}C. Fumarate reduction with methyl viologen
(pH 7.0) and succinate oxidation with potassium ferricyanide (pH 8.0)
were performed as described in "Experimental Procedures".
Nd, not determined

Hinge-threonine Mutants—The next region targeted for mutagenesis was the conserved Thr in the His-Pro-Thr (HPT) sequence of QFR and SQR, since this hinge-T interacts with the proton-shuttling residue Arg-A248. The QFR hinge-T mutant showed expression levels similar to those of wild type QFR; however, the SQR hinge-T mutant was expressed at 5-7-fold lower levels than wild type (data not shown). The SQR hinge-T mutant lost succinate-ubiquinone reductase activity and heme b activity. Attempts to purify the SQR hinge-T mutant enzyme resulted in proteolysis, which was probably due to impaired stability and/or assembly of the mutant enzyme.

In contrast, the QFR hinge-T mutant was amenable to enzymatic and structural analyses over a wide pH range. The hinge-T substitution significantly affected dicarboxylate binding at the active site (Table 2). The Km values for fumarate and succinate significantly increased, and the Ki for OAA increased by more than 100-fold (Table 2). Typical for complex II enzymes, the pH profile of kcat demonstrates a mirror-like profile, where succinate oxidation increases and

fumarate reduction decreases at high pH values (49). The QFR hinge-T mutation shifted the succinate oxidation pKa shift from 7.4 for wild type QFR to 8.7 in the mutant (Fig. 3). In the mutant, the fumarate reductase reaction is pH-independent over the pH range 6.0-8.5, consistent with the increase in apparent pKa to over pH 8.5 (Fig. 20). Although overall catalytic activity is impaired in the QFR hinge-T mutant, the residual succinate oxidase activity at pH 9.0 is about 10% of wild type, and the fumarate reductase activity at pH 8.0 is also 10% of wild type QFR.
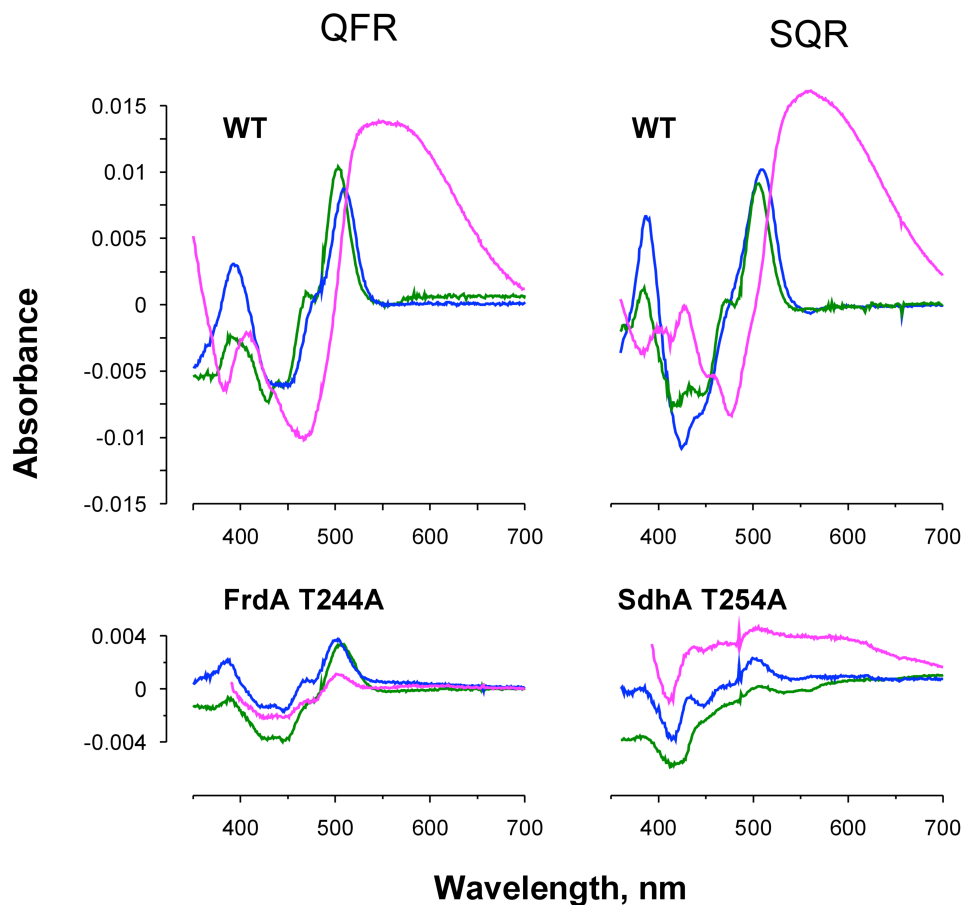
Figure 20. pH dependence of succinate oxidase and fumarate reductase reactions catalyzed by wild type and hinge-T QFR enzymes (30ºC). Enzymatic activities of wild type QFR (open circles) and hinge-T (FrdA T234A; filled circles) were performed as described in "Experimental procedures"

In agreement with the kinetic data, ligand induced optical changes in the QFR hinge-T enzyme (Fig. 21). At pH 7.0, all three dicarboxylates examined induced similar spectral changes, and OAA clearly showed two spectral features. One was a peak at 500 nm characteristic of the other dicarboxylates. The second change was a significantly reduced charge transfer band (500-700 nm) compared with wild type QFR (Fig. 19), consistent with a change of relative orientation of the OAA and flavin in the mutant at pH 7.0 (48). At pH 9.0, where the hinge-T mutant demonstrated 10-fold higher activity than at pH 7.0, the increased absorbance of the charge transfer band closely resembled that seen for wild type QFR. The OAA-induced optical changes for wild type QFR did not significantly differ between pH 7.0 and 9.0 (Fig. 21).
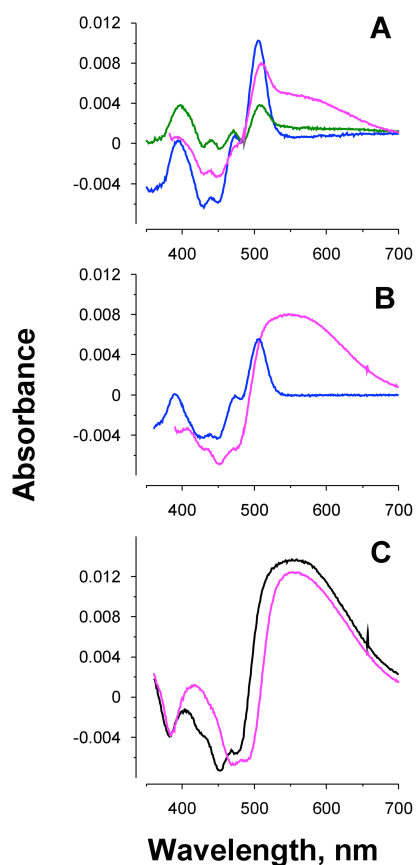
Figure 21. Ligand induced optical changes of hinge-T QFR enzyme (25ºC). *A* and *B*. Difference spectra show the effect of malonate (green, 10 mM) fumarate (blue, 10mM), and OAA (magenta, 2 mM) on the spectrum of fully oxidized FrdA T234A enzymes at pH 7.0 (*A*) and 9.0 (*B*). The concentrations of ligands were 10 mM malonate, 10 mM fumarate, and 2 mM OAA. *C*. OAA induced spectral changes of wild type QFR at pH 7.0 (black) and 9.0 (magenta). Protein concentration of wild type and hinge-T QFR was 4.9 μM.

Structural Characterization of the QFR Hinge-T Mutant—To provide a structural framework for how the hinge-T substitution affected substrate binding and enzyme activity, the structure was determined to 3.65 Å resolution using x-ray crystallography. Previous E. coli QFR structures show clear electron density for the weak inhibitor citrate bound at the active site, due to citrate in the crystallization

conditions (23, 50). The QFR hinge-T mutation caused a dramatically decreased affinity for dicarboxylate inhibitors (Table 3), and despite the presence of 100 mm citrate in the crystallization reaction, the structure of the mutant enzyme showed no clear electron density in the active site.

Loss of substrate binding in the hinge-T mutant may be explained upon examination of the structure. In homologue structures where the capping domain and FAD domain are in a closed conformation (21, 23, 50), a minimum of one-third of the hydrogen bonds to substrate are provided by residues of the capping domain. In the QFR hinge-T structure, the capping domain rotated by 5.3°, opening a pathway to the active site (Fig. 22). The new rotated capping domain position resembles the maximally open conformation observed in the Shewanella Fcc3 enzyme (9). This rotation moves the capping domain side chains into positions where they no longer hydrogen-bond to substrate or inhibitors. Consistent with this, all structures to date with an open position of the capping domain lack bound substrate at the active site.

Figure 22. Comparison of the position of the capping domain in wild type and hinge-T (FrdA T234A) QFR. The hinge-T QFR capping domain (green) is superimposed onto the flavoprotein of wild type QFR capping domain (grey). Green dashes connect the main chain of the hinge-T mutant in regions where the crystallographic electron density does not allow the main chain to be resolved unambiguously. Side chain carbons are colored grey in wild-type QFR and are colored green in the hinge-T mutant. FAD carbons are colored yellow, nitrogen atoms are colored blue, oxygen colored red. *A*. In the hinge-T mutant, the structure of the FAD-binding domain (orange) is not significantly altered and can be superimposed with a RMS deviation of 0.3 Å. However the capping domain has rotated 5.3º with respect to the wildtype enzyme (PDBID 1KF6). The direction of the capping domain rotation and the proposed substrate path are denoted with black arrows.

Particularly important to catalytic activity are Arg-A287, the proton donor during reduction, and Thr-A244, which is critical for transition state formation. In the majority of crystal structures of complex II homologs, the   uanidine group of the residue equivalent to Arg-A287 is poised for proton transfer to substrate, since it forms a hydrogen bond to the bound dicarboxylate (10, 11, 19, 20, 22). In the hinge-T mutant, the movement of the capping domain into the open position shifted the Cα atom of Arg A287 5.5 Å from the active site and moved the Nζ atom of the side chain to a distance too far for proton transfer. The act-T side chain was also located on the capping domain. In the hinge-T mutant, the domain rotation moved the Cα atom of act-T by 1.5 Å and shifted the side chain away from the dicarboxylate binding site. The repositioning of both Arg-A287 and act-T may contribute to the observed decrease in the reaction rate in the hinge-T mutant.

In the hinge-T mutant, the rotation of the capping domain into the open conformation was associated with decreased electron density quality compared with other regions of the mutant QFR. This was shown by an increase in crystallographic temperature factors. In the structure, the average temperature factor was 72 $Å^2$ in the FAD-binding domain main chain as compared with 168 Å2 in the capping domain main chain. A similar temperature factor increase is observed in the Shewanella Fcc3 open conformation structure (Protein Data Bank code 1QO8) (9). The electron density maps for the hinge-T mutation lacked appreciable density for many of the side chains. Nevertheless, it is clear that the domain rotation observed in the hinge-T mutation results in alterations of the
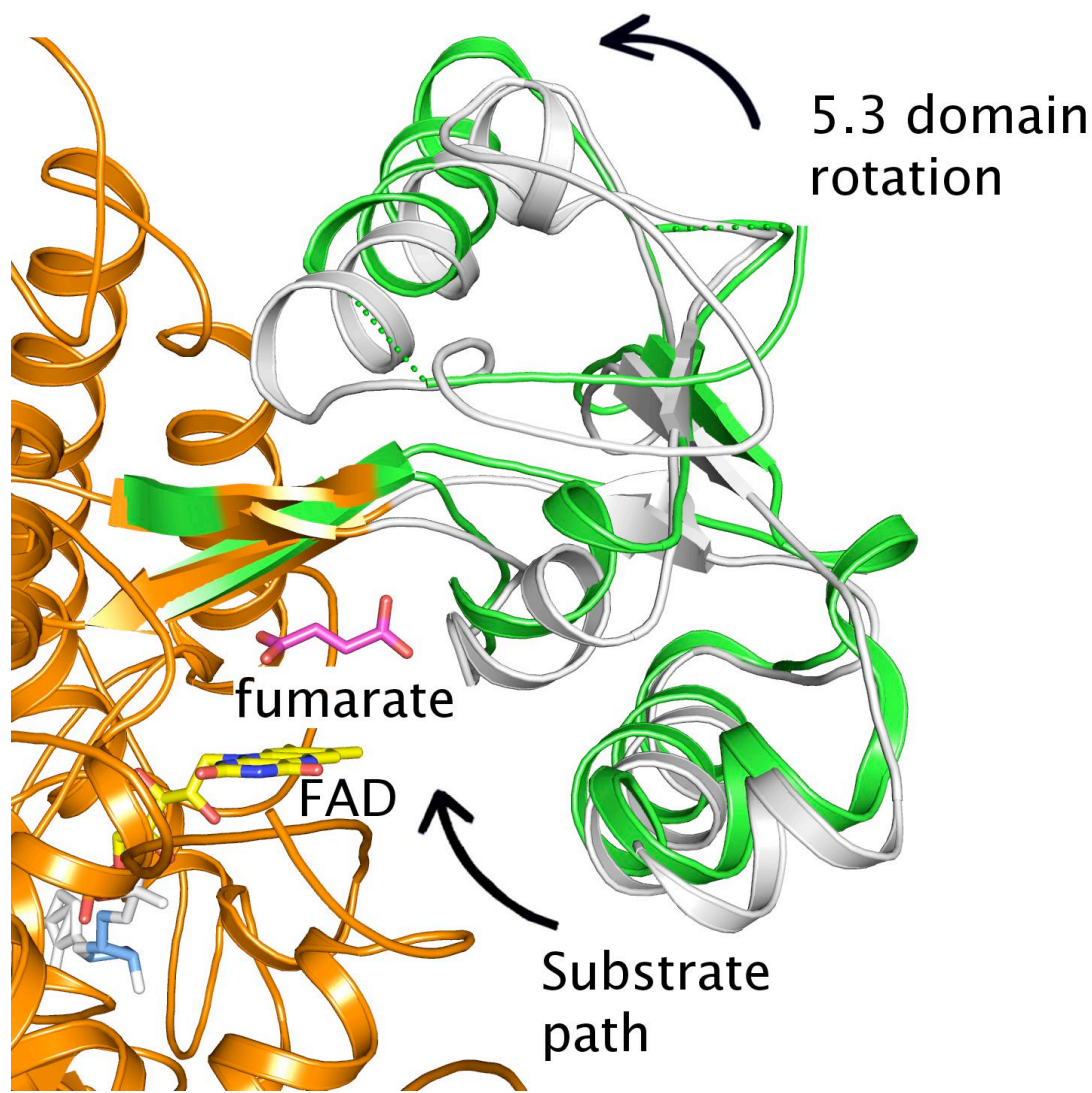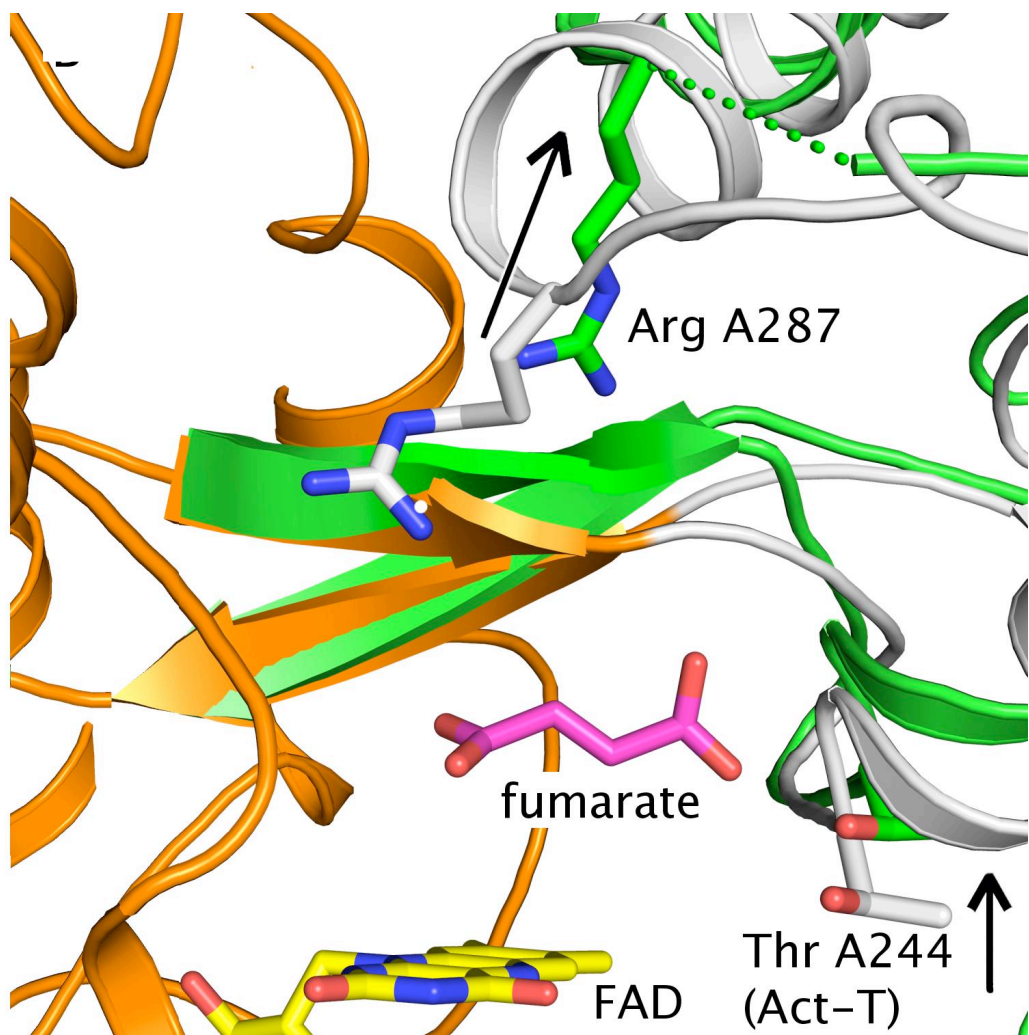
Figure 23. Comparison of the position of the capping domain in wild type and hinge-T (FrdA T234A) QFR. The hinge-T QFR capping domain (green) is superimposed onto the flavoprotein of wild type QFR capping domain (grey). Green dashes connect the main chain of the hinge-T mutant in regions where the crystallographic electron density does not allow the main chain to be resolved unambiguously. Side chain carbons are colored grey in wild-type QFR and are colored green in the hinge-T mutant. FAD carbons are colored yellow, nitrogen atoms are colored blue, oxygen colored red. *A*. In the hinge-T mutant, the structure of the FAD-binding domain (orange) is not significantly altered and can be superimposed with a RMS deviation of 0.3 Å. However the capping domain has rotated 5.3º with respect to the wildtype enzyme (PDBID 1KF6). The direction of the capping domain rotation and the proposed substrate path are denoted with black arrows. The altered position of the capping domain shifts the proton shuttling residues in the hinge-T mutant. Black arrows indicate the direction of local structural changes.

Hydrogen bond network of Arg-A287 and Arg-A248 in the proton shuttle, which may alter the pKa values of each side chain. In addition to the 5.5-Å shift of Arg-A287, the Cα atom of Arg-A248 shifted 2.1 Å away from the active site (Fig. 23). As described above, the hinge-T mutant had an altered pH profile as compared with wild type. The hinge-T Oγ-Arg-A248 Nζ hydrogen bond probably serves to modulate the pKa of Arg-A248 so that loss of the hydrogen bond from the Oγ of Thr-A234 to the uanidine group of Arg-A248 may raise the pKa of the Arg-A248 side chain. Crystallographic electron density does not unambiguously reveal the Arg-A248 side chain position, which is most likely disordered and solvent-exposed.

Discussion

The E. coli complex II homologs QFR and SQR contain covalently bound FAD and thus are able to reversibly oxidize succinate or reduce fumarate (49). This makes them useful models for study of bidirectional catalysis in complex II enzymes (1, 12, 49). An active site loop identified between act-T (QFR Thr-A244; SQR Thr-A254) and hinge-T (QFR Thr-A234; SQR Thr-A244) was tested for its importance in catalysis of the reaction in both directions for two reasons; first, it provides numerous hydrogen bonds to substrate, and second, it provides a key stabilizing interaction with the proton shuttle. In this study, the role of the two conserved threonine residues in this loop was investigated.

The Act-T Hydrogen Bond May Stabilize the Transition State—Structures of Fcc3 fumarate reductases and the W. succinogenes QFR co-crystallized with

fumarate show a twisted conformation of the C1 carboxylate in the species bound at the active site. Fumarate twisting may strain the double bond and decrease the free energy barrier for attaining the transition state (11, 12, 21). Elimination of the act-T side chain, which hydrogen-bonds to the carbonyl where fumarate is twisted, dramatically impairs catalysis of both the E. coli SQR and QFR enzymes (Table 2). The altered binding of dicarboxylate ligands in the act-T mutant is seen with the absence of CT absorbance upon OAA binding and significantly decreased spectral changes upon fumarate or malonate binding (Fig. 19). This suggests that the removal of the act-T Oγ hydrogen bond affects both substrate binding and transition state stabilization. In contrast, substitutions of other active site residues equivalent to E. coli FrdA His-232 and His-354 were mainly shown to affect substrate binding (12, 26, 51).

Furthermore, in the Fcc3 enzyme, x-ray crystallography of a mutant enzyme equivalent to E. coli QFR FrdA H232A only showed subtle changes in the position of fumarate; however, the C1 carboxyl group is found in the same twisted conformation as in wild type enzyme (26), indicating that this histidine does not participate in transition state formation. The substitution of the active site threonine (FrdA Thr-244/SdhA Thr-254) to alanine caused a much more dramatic effect on complex II enzyme activity compared with the single substitutions of the two histidine residues found at the active site in the soluble Fcc3 enzyme (26). The results presented here are consistent with act-T being essential for positioning the C1 carboxyl of fumarate and efficient catalysis in the complex II family of enzymes.

The Hinge-T Mutant May Trap the Proton Shuttle in an Intermediate State—

Hinge-T (Thr-A234 in QFR; Thr-A244 in SQR) in the conserved His-Pro-Thr of the capping domain hydrogen-bonds to the Arg-A248 side chain, part of the complex II proton shuttle. The effect of removing this hydrogen-bonding interaction was investigated. The hinge-T variant enzyme demonstrates altered pH dependence of the catalyzed reactions. This has several plausible explanations that are not mutually exclusive. First, the elimination of the hydrogen bond from Thr-A234 to Arg-A248 may alter the Arg-A248 side chain conformation so that it no longer can transfer protons to Glu-A245, thereby disrupting catalytic activity. Since electron density for the side chain of Arg-A248 could not be observed in the hinge-T mutant structure, the orientation of Arg-A248 in the hinge-T variant cannot be unambiguously established. A second explanation is that the loss of a hydrogen bond to Arg-A248 may shift the pKa of the proton shuttle. This may correlate with the increased succinate oxidase activity and stabilization of the OAA anionic transition state at high pH. In wild type QFR, the CT amplitude does not change at pH 7 or 9 and does not correlate with the pKa of the reaction (36, 49). This suggests that microscopic pKa values of amino acid residues involved in substrate activation are below pH 7, and the observed pKa of the reaction is influenced by other active site or proton shuttle residues. Increased stabilization of the CT species in the hinge-T mutant with increased pH may reflect either change in the pKa of the residues involved in substrate activation or conformational changes in the movable capping domain that effect ionization properties of the active site residues and/or substrate binding position.

Proton Shuttle Regeneration May Trigger Domain Movements during

87

Catalysis—Unexpectedly, a dramatically decreased substrate affinity is observed in the hinge-T mutant enzyme. The x-ray structure of the hinge-T variant reveals a rearrangement between the FAD-binding and capping domains of the flavoprotein subunit that disrupts hydrogen bonding to substrate and prevents optimal substrate orientation for catalysis. Sequence and structural analysis support the possibility that the orientation between the capping domain and FAD-binding domain is not fixed. The capping domain contains a disproportionate number of glycine residues. Of the 120 residues in the capping domain, 19 are glycines, and of those, seven are within the first 20 residues of the capping domain. Glycines typically predominate where their added flexibility allows conformational rearrangements of proteins.

The interdomain angles appear to be influenced by the presence of substrate at the active site. In the higher resolution Fcc3 structures (11), which allow for reliable identification of hydrogen bonds, only 11 interdomain hydrogen bonds between the FAD domain and the capping domain stabilize the closed state. Of these, six are between the polypeptide chains, and five are to substrate. Consequently, lack of bound substrate would probably destabilize a closed conformation. Similarly, the wild type E. coli QFR structure was determined in complex with citrate in an intermediate position of the FAD-binding and capping domains (50). In the intermediate structure, a decreased percentage of stabilizing hydrogen-bonding interactions are observed; only eight hydrogen bonds mediate this contact. In this case, it is the hydrogen bonds to the dicarboxylate that are exclusively lost, such that in the intermediate position of the capping domain, only

two through-substrate bonds remain. Furthermore, all open structures of flavoprotein homologues, including this new structure of the hinge-T mutant, lack crystallographic electron density corresponding to bound dicarboxylate at the active site.

In previous structures, it was unclear how crystal contacts influenced domain opening. This hinge-T mutant has the same crystal packing as wild type and exhibits a domain rotation, indicating that the rotation is probably correlated to the enzymatic state and not an artifact of different crystallization conditions. The low number of stabilizing contacts, a high percentage of which are through substrate, suggests that the kinetic barrier between open and closed states is low and can be influenced by substrate binding. As a result, substrate binding or proton shuttle state could heavily influence the conformation. Flavoproteins in general may use such movements to control active site solvation as a means of optimizing catalysis and even determining the enzyme's role as an oxidase, oxygenase, or dehydrogenase (25, 52).

The possibility that domain reorientation accompanies catalysis and may correlate with the proton shuttle state stands in contrast to previous studies in a soluble QFR homolog (Fcc3) from Shewanella frigidimarina, which suggest a minimal role for capping domain mobility in fumarate catalysis (24). There, a disulfide bond was introduced between the capping domain and the rest of the flavoprotein to restrict capping domain movement. This disulfide bond reduced catalysis by 90%, and it was argued that this constituted an insignificant decrease in activity. One possible explanation for the difference in models from Fcc3 and the

QFR hinge-T mutant could be due to the nature of soluble fumarate reductases compared with membrane-bound complex II homologs. In all structures of the E. coli QFR determined to date, the electron density maps showed significantly better quality for integral membrane polypeptides than for the soluble domain.[4] Thus, it is possible that membrane association may add stability to the entire protein and allow for conformational freedom in the soluble domain in E. coli QFR. Furthermore, other capping domain movements may compensate for the motion restriction imposed by the disulfide bond, allowing the substrate access to the active site.

Act-T May Work in Concert with Domain Movements to Promote the Formation of the Transition State—Although there are several possibilities for the observed domain reorientations in the hinge-T mutant, the design of this variant to mimic a regenerating proton shuttle suggest that this movement accompanies catalysis. As seen in Fig. S1 (movie), a channel that forms in the ligand-free conformation allows substrate to access the active site. The open orientation of the two domains poises the act-T side chain to form essential hydrogen-bonding interactions that selectively pull the substrate into the active site. Subsequently, the bonds between act-T and substrate may induce active site closure by rotation of the capping domain to form further hydrogen bonding interactions with the substrate. Domain closure may force the interaction between act-T and substrate to twist the C1 carboxyl group and strain the double bond of fumarate while concomitantly orienting the proton shuttle Arg-A287 into an optimal position for catalysis. In this now solvent-protected active site, the dicarboxylate transition state

90

can accept hydride from FAD and a proton from Arg-A287.

Conclusions

The roles of two threonine residues on an active site loop were analyzed with the mutation to alanine. The act-T mutation shows the importance of a hydrogen bond to substrate that stabilizes the high energy intermediate states. Movement of the active site loop and the capping domain from open to closed states may serve to twist the substrate into a transition state for catalysis. Fluctuation between the open and closed states of the capping domain may protect the high energy intermediate from water in the active site while still permitting substrate binding in the open state. This may serve as an important mechanism to enhance on-pathway catalytic efficiency while minimizing the formation of off-pathway side products.

References

1.   Cecchini, G. (2003) *Annu. Rev. Biochem.* **72**, 77-109

2.   Iverson, T. M., Luna-Chavez, C., Schröder, I., Cecchini, G., and Rees, D. C. (2000) *Curr. Opin. Struct. Biol.* **10**, 448-455

3.   Ohnishi, T., King, T. E., Salerno, J. C., Blum, H., Bowyer, J. R., and Maida, T. (1981) *J. Biol. Chem.* **256**, 5577-5582

4.   Blaut, M., Whittaker, K., Valdovinos, A., Ackrell, B. A. C., Gunsalus, R. P., and Cecchini, G. (1989) *J. Biol. Chem.* **264**, 13599-13604

5.   Ackrell, B. A. C., Cochran, B., and Cecchini, G. (1989) *Arch. Biochem. Biophys.* **268**, 26-34

6.   Leger, C., Heffron, K., Pershad, H. R., Maklashina, E., Luna-Chavez, C., Cecchini, G., Ackrell, B. A. C., and Armstrong, F. A. (2001) *Biochemistry* **40**, 11234-11245

7.   Jeuken, L. J. C., Jones, A. K., Chapman, S. K., Cecchini, G., and Armstrong, F. A. (2002) *J. Amer. Chem. Soc.* **124**, 5702-5713

8.   Mattevi, A., Tedeschi, G., Bacchella, L., Coda, A., Negri, A., and Ronchi, S. (1999) *Structure* **7**, 745-756

9.   Bamford, V., Dobbin, P. S., Richardson, D. J., and Hemmings, A. M. (1999) *Nat. Struct. Biol.* **6**, 1104-1107

10.   Taylor, P., Pealing, S. L., Reid, G. A., Chapman, S. K., and Walkinshaw, M. D. (1999) *Nat. Struct. Biol.* **6**, 1108-1112

11.   Leys, D., Tsapin, A. S., Nealson, K. H., Meyer, T. E., Cusanovich, M. A., and Van Beeumen, J. J. (1999) *Nat. Struct. Biol.* **6**, 1113-1117

12.   Reid, G. A., Miles, C. S., Moysey, R. K., Pankhurst, K. L., and Chapman, S. K. (2000) *Biochim. Biophys. Acta* **1459**, 310-315

13.   Lancaster, C. R. D. (2003) *Adv. Protein Chem.* **63**, 131-149

14.   Ackrell, B. A. C. (2000) *FEBS Lett.* **466**, 1-5

15.   Lancaster, C. R. D., and Kroger, A. (2000) *Biochim. Biophys. Acta* **1459**, 422-431

16.   Sun, F., Huo, X., Zhai, Y. , Wang, A., Xu, J., Su, D., Bartlam, M., and Rao, Z. (2005) *Cell* **121**, 1043-1057

17.   Huang, L. S., Shen, J. T., Wang, A. C., and Berry, E. A. (2006) *Biochim. Biophys. Acta* **1757**, 1073-1083

18.   Yankovskaya, V., Horsefield, R., Törnroth, S., Luna-Chavez, C., Miyoshi, H., Léger, C., Byrne, B., Cecchini, G., and Iwata, S. (2003) *Science* **299**, 700-704

19.   Huang, L. S., Sun, G., Cobessi, D., Wang, A. C., Shen, J. T., Tung, E. Y., Anderson, V. E., and Berry, E. A. (2006) *J. Biol. Chem.* **281**, 5965-5972

20.   Madej, M. G., Nasiri, H. R., Hilgendorff, N. S., Schwalbe, H., and Lancaster, C. R. D. (2006) *EMBO J.* **25**, 4963-4970

21.   Lancaster, C. R. D., Kroger, A., Auer, M., and Michel, H. (1999) *Nature* **402**, 377-385

22.   Lancaster, C. R. D., Grosβ, R., and Simon, J. (2001) *Eur. J. Biochem.* **268**, 1820-1827

23.   Iverson, T. M., Luna-Chavez, C., Cecchini, G., and Rees, D. C. (1999) *Science* **284**, 1961-1966

24.   Rothery, E. L., Mowat, C. G., Miles, C. S., Mott, S., Walkinshaw, M. D., Reid, G. A., and Chapman, S. K. (2004) *Biochemistry* **43**, 4983-4989

25.   Mattevi, A. (2006) *Trends Biochem. Sci.***31**, 276-283

26.   Doherty, M. K., Pealing, S. L., Miles, C. S., Moysey, R., Taylor, P., Walkinshaw, M. D., Reid, G. A., and Chapman, S. K. (2000) *Biochemistry* **39**, 10695-10701

27.   Pankhurst, K. L., Mowat, C. G., Miles, C. S., Leys, D., Walkinshaw, M. D., Reid, G. A., and Chapman, S. K. (2002) *Biochemistry* **41**, 8551-8556

28.   Mowat, C. G., Moysey, R., Miles, C. S., Leys, D., Doherty, M. K., Taylor, P., Walkinshaw, M. D., Reid, G. A., and Chapman, S. K. (2001) *Biochemistry* **40**, 12292-12298

29. Pankhurst, K. L., Mowat, C. G., Rothery, E. L., Hudson, J. M., Jones, A. K., Miles, C. S., Walkinshaw, M. D., Armstrong, F. A., Reid, G. A., and Chapman, S. K. (2006) *J. Biol. Chem.* **281**, 20589-20597

30. Westenberg, D. J., Gunsalus, R. P., Ackrell, B. A. C., Sices, H., and Cecchini, G. (1993) *J. Biol. Chem.* **268**, 815-822

31. Maklashina, E., Berthold, D. A., and Cecchini, G. (1998) *J. Bacteriol.* **180**, 5989-5996

32. Maklashina, E., Rothery, R. A., Weiner, J. H., and Cecchini, G. (2001) *J. Biol. Chem.* **276**, 18968-18976

33. Rothery, R. A., Seime, A. M., Spiers, A. M. C., Maklashina, E., Schroder, I., Gunsalus, R. P., Cecchini, G., and Weiner, J. H. (2005) *FEBS J.* **272**, 313-326

34. Kita, K., Vibat, C. R. T., Meinhardt, S., Guest, J. R., and Gennis, R. B. (1989) *J. Biol. Chem.* **264**, 2672-2677

35. Maklashina, E., Hellwig, P., Rothery, R. A., Kotlyar, V., Sher, Y., Weiner, J. H., and Cecchini, G. (2006) *J. Biol. Chem.* **281**, 26655-26664

36. Maklashina, E., Iverson, T. M., Sher, Y., Kotlyar, V., Andréll, J., Mirza, O., Hudson, J. M., Armstrong, F. A., Rothery, R. A., Weiner, J. H., and Cecchini, G. (2006) *J. Biol. Chem.* **281**, 11357-11365

37. Luna-Chavez, C., Iverson, T. M., Rees, D. C., and Cecchini, G. (2000) . *Protein Expression Purif.* **19,** 188-196

38.   Otwinowski, Z. (1993) In *CCP4 Study Weekend Data Collection and Processin,*(Sawyer, L., Isaacs, N., and Bailey S., eds): pp. 56-62, *SERC Daresbury Labortatory, UK*

39.   Bailey, S. (1994) *Acta Cryst. Sect. D* **50**, 760-763

40.   Brunger, A. T., Adams, P. D., Clore, G. M., DeLano, W. L., Gros, P., Grosse-Kunstleve, R. W., Jiang, J. S., Kuszewski, J., Nilges, M., Pannu, N. S., Read, R. J., Rice, L. M., Simonson, T., and Warren, G. L. (1998) *Acta Cryst. Sect. D* **54**, 905-921

41.   Adams, P. D., Grosse-Kunstleve, R. W., Hung, L. W., Ioerger, T. R., McCoy, A. J., Moriarty, N. W., Read, R. J., Sacchettini, J. C., Sauter, N. K., and Terwilliger, T. C. (2002) *Acta Cryst. Sect. D* **58**, 1948-1954

42.   Jones, T. A., Zou, J. Y., Cowan, S. W., and Kjeldgaard, M. (1991) *Acta Cryst. Sect. A* **47**, 110-119

43.   Emsley, P., and Cowtan, K. (2004) *Acta Cryst. Sect. D* **60**, 2126-2132

44.   DePristo, M. A., de Bakker, P. I. W., Johnson, R. J. K., and Blundell, T. L. (2005) *Structure* **13**, 1311-1319

45.   DeLano, W. L. (2002) *DeLano Scientific, Palo Alto, CA, USA*

46.   Veeger, C., Dervartanian, D. V., Kalse, J. F., de Kok, A., and Koster, J. F. (1966) In *Flavins and Flavoproteins*, (Slater, E. C., ed.) pp. 242-262, Elsevier/Amsterdam, The Netherlands

47.   Wardrope, C., Mowat, C. G., Walkinshaw, M. D., Reid, G. A., and Chapman, S. K. (2006) *FEBS Lett.* **580**, 1677-1680

48.   Massey, V., and Ghisla, S. (1974) *Ann. N. Y. Acad. Sci.* **227**, 446-465

49.   Maklashina, E., and Cecchini, G. (1999) *Arch. Biochem. Biophys.* **369**, 223-232

50.   Iverson, T. M., Luna-Chavez, C., Croal, L. R., Cecchini, G., and Rees, D. C. (2002) *J. Biol. Chem.* **277**, 16124-16130

51.   Schröder, I., Gunsalus, R. P., Ackrell, B. A. C., Cochran, B., and Cecchini, G. (1991) *J. Biol. Chem.* **266**, 13572-13579

52.   Bossi, R. T., Negri, A., Tedeschi, G., and Mattevi, A. (2002) *Biochemistry* **41**(9), 3018-3024

Acknowledgements

CHAPTER III

GEOMETRIC RESTRAINT DRIVES ON- AND OFF- PATHWAY CATALYSIS BY

THE ESCHERICHIA COLI MENAQUINOL:FUMARATE REDUCTASE

Abstract

Complex II superfamily members catalyze the kinetically difficult interconversion of succinate and fumarate. Due to the relative simplicity of complex II substrates and their similarity to other biologically abundant small molecules, substrate specificity presents a challenge in this system. In order to identify determinants for on-pathway catalysis, off-pathway catalysis, and enzyme inhibition, crystal structures of *Escherichia coli* menaquinol:fumarate reductase (QFR), a complex II superfamily member, were determined bound to the substrate, fumarate, and the inhibitors oxaloacetate, glutarate, and 3-nitropropionate. Optical difference spectroscopy and computational modeling support a model where QFR twists the dicarboxylate, activating it for catalysis. Orientation of the C2-C3 double bond of activated fumarate parallel to the C(4a)-N5 bond of FAD allows orbital overlap between the substrate and the cofactor, priming the substrate for nucleophilic attack. Off-pathway

catalysis, such as the conversion of malate to oxaloacetate or the activation of the toxin 3-nitropropionate may occur when inhibitors bind with a similarly activated bond in the same position. Conversely, inhibitors that do not orient an activatable bond in this manner, such as glutarate and citrate, are excluded from catalysis and act as inhibitors of substrate binding. These results support a model where electronic interactions via geometric constraint and orbital steering underlie catalysis by QFR.

Introduction

Complex II superfamily enzymes provide a crucial link between oxidoreduction reactions in the membrane bilayer and in the soluble milieu (1). During aerobic respiration in *E. coli*, the complex II enzyme succinate:ubiquinone oxidoreductase (SQR) oxidizes succinate and reduces ubiquinone. In bacterial anaerobic respiration with fumarate as the terminal electron acceptor, the reaction proceeds in the opposite direction, and the complex II homolog menaquinol:fumarate oxidoreductase (QFR) oxidizes menaquinol and transfers the electrons to fumarate. Complex II superfamily members contain either three or four polypeptide chains (Fig. 24): two soluble subunits (the flavoprotein, FrdA, and the iron protein, FrdB in *E. coli* QFR) and either one or two integral membrane subunits (FrdC and FrdD in the *E. coli* QFR).
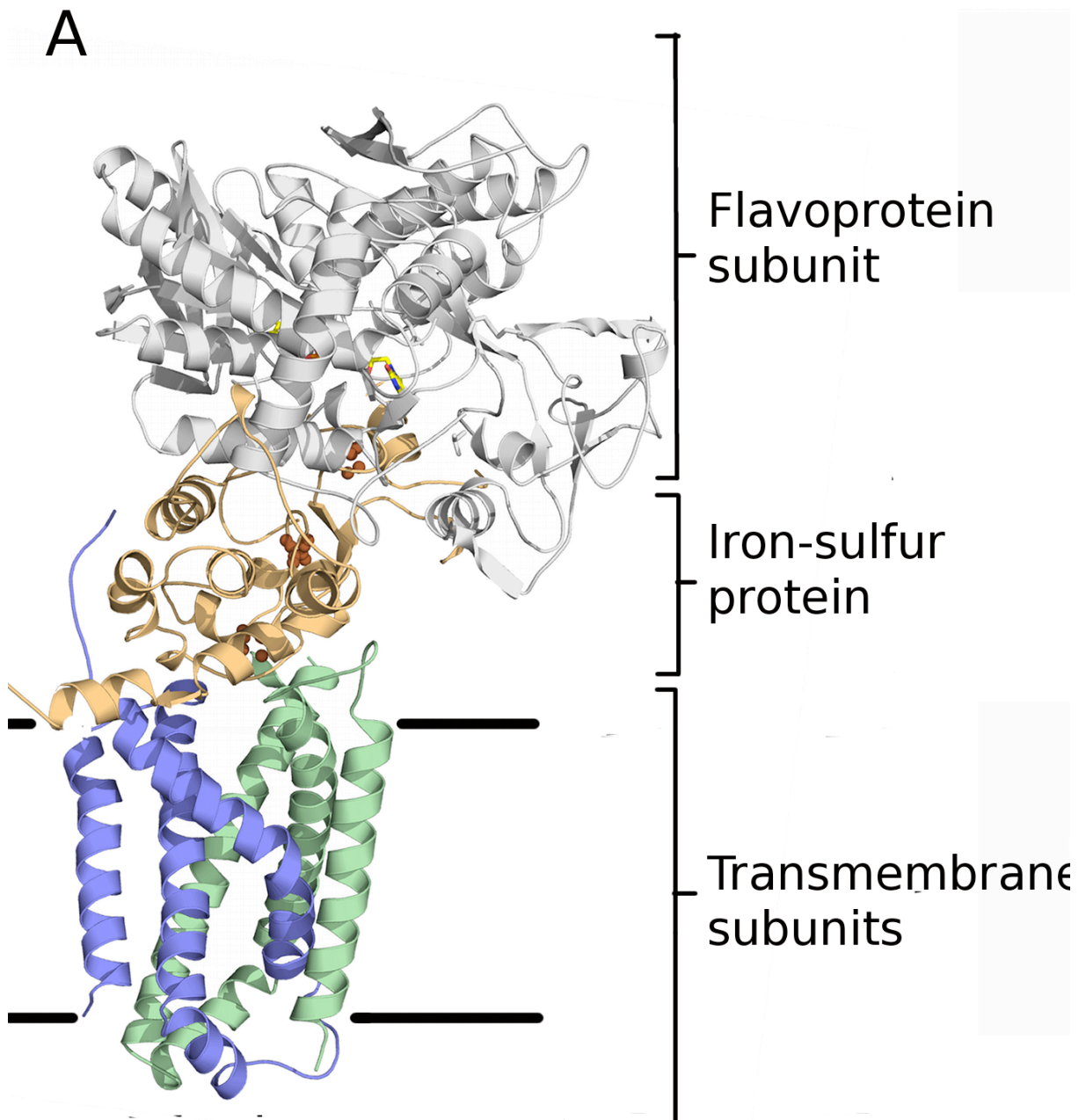
Figure. 24. Structure of the *E. coli QFR* and relevant ligands. A. Structure of the *E. coli* QFR heterotetramer with the flavoprotein subunit (FrdA) colored *grey*, iron-sulfur protein (FrdB) colored *orange*, and the transmembrane subunits colored *blue* (FrdC) and *green* (FrdD).

While there are significant differences in the integral membrane subunits across the family, complex II enzymes all share a high percentage of sequence identity in the soluble subunits, including the flavoprotein, where the kinetically challenging oxidoreduction of fumarate and succinate takes place (1). Numerous molecules including metabolic intermediates and ingested toxins structurally resemble succinate and fumarate. Some of these are excluded from the active site, while others act as inhibitors (Fig. 25).
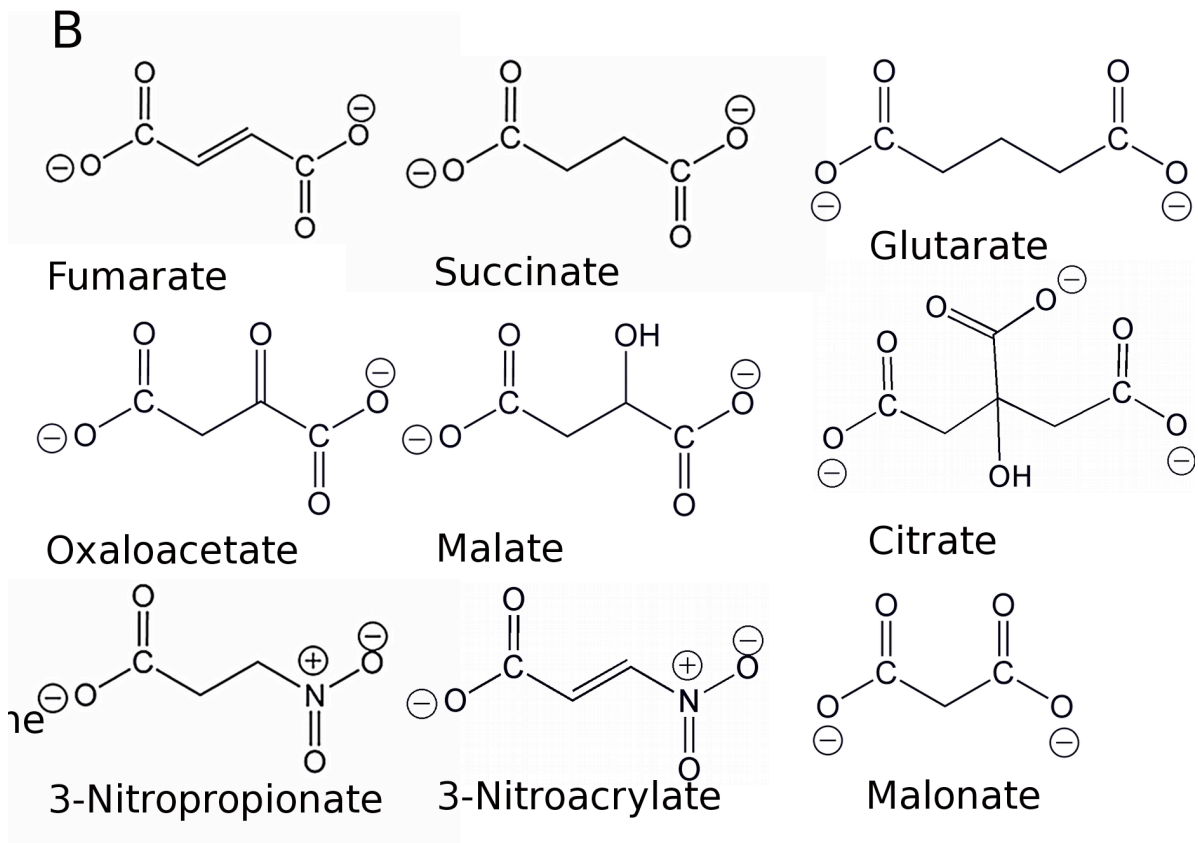
Figure. 25 B. Structures of the substrate, fumarate, the product, succinate, and molecules that interact with the dicarboxylate binding site and are discussed in this work.

Several of these come from normal respiratory processes. For example, oxaloacetate is a Krebs cycle intermediate and acts as a tight, slow-binding inhibitor

100

of complex II, possibly as a regulatory mechanism (2,3). It has additionally been proposed that oxaloacetate can be formed through off-pathway catalysis by complex II when fumarate hydration to malate is followed by oxidation to oxaloacetate (3,4). Oxaloacetate binding to the complex II active site results in a charge transfer complex between the oxaloacetate carbonyl and the FAD hydride that can be monitored spectroscopically (4,5).

Along with physiological regulation from metabolites, complex II activity may be affected by overproduction of dicarboxylates that result from dysfunction of cellular catabolic pathways. For example, mutation of glutaryl co-A decarboxylase can lead to elevated levels of the dicarboxylates glutarate and 3-hydroxy glutarate (Fig. 1B) and this has been associated with glutaric acidemia type I, which has symptoms that include cerebral swelling and motor defects (6). Respiratory chain deficiency correlates with glutaric acidemia type I, and complex II inhibition is observed in cell culture upon application of glutarate (7).

Ingested toxins offer a third source of complex II inhibitors, often with severe health consequences. The fungus *Arthrinium sphaerospermum* produces the secondary metabolite 3-nitropropionate (3-NP) an irreversible complex II inhibitor (Fig. 1B)(8-10). When ingested, 3-NP can induce striatal brain lesions similar to those observed in patients with Huntington's disease, an autosomal dominant neurodegenerative disease characterized by dyskinesia, cognitive defects, and psychological pathologies (11). In fact, 3-NP is commonly used to recapitulate a subset of the pathologies of Huntington's Disease in animal models (11). The mechanism of 3-NP inhibition of complex II is under debate. Previously, 3-NP has

been proposed to form a covalent adduct with either FAD (8), an active site cysteine residue (12), or a catalytic arginine near the dicarboxylate binding site (13). The formation of any of these adducts likely requires a single enzyme turnover, but has not been determined conclusively (12). 3-NP has also been proposed to act as a non-covalent inhibitor of complex II enzymes (14).

To study the details of complex II catalysis and inhibition at the flavoprotein active site, the *E. coli* QFR was co-crystallized with the substrate, fumarate, and the inhibitors, oxaloacetate, glutarate, and 3-NP. Mass spectrometry and optical spectroscopy allowed unambiguous confirmation of the covalent 3-NP adduct and the proposal of a possible reaction mechanism. The implications for fumarate turnover and the mechanisms of inhibition are discussed.

Materials and Methods

QFR purification– *E. coli* QFR was produced in *E. coli* strain DW35 (*ΔfrdABCD, sdhC:kan*) containing the pH3 (*frdA$^+$B$^+$C$^+$D$^+$)* plasmid. Cells were grown under microaerophilic conditions in Terrific Broth medium as previously described (15). Membranes were isolated as described in (15) and were resuspended in a solution of 20 mM Tris, 0.1 mM EDTA (pH 7.4) and solubilized with $C_{12}E_9$ detergent (Anatrace, Maumee, OH) added to a final concentration of 2% (w/v). Purification of QFR was performed in the presence of 0.05% (w/v) $C_{12}E_9$ as described (15) using Q-sepharose anion exchange (GE Healthcare), POROS anion exchange (Applied Biosystems), and size exclusion chromatography on a superdex S-200 column (GE Healthcare).

Enzyme assays– In order to measure full succino-quinone reductase or succino-oxidase activity of QFR, it is necessary to remove any tightly bound oxaloacetate, which co-purifies with the as-isolated enzyme (3). To activate the enzyme, QFR was diluted to 5 mg of protein/ml in 30 mM Bis-Tris-Propane (BTP), pH 7.0, 0.1 mM EDTA, 0.05% $C_{12}E_9$, and 3 mM malonate and incubated for 20 min at 30° C. The enzyme was then concentrated with a Centricon YM30 filtration apparatus and the concentrated protein was passed through a PD-10 gel-filtration column to remove malonate. Activated enzyme was then stored at 4° C until used. The standard assay medium at 30° C contained 50 mM BTP, 0.1 mM EDTA, 0.006% $C_{12}E_9$, pH 8.0. Succino-oxidase activity of QFR was measured with the electron acceptor potassium ferricyanide as previously described (16). In order to determine apparent affinity constants for the dicarboxylates used in this study, inhibition of the ferricyanide reductase activity was determined as previously described (17).

Optical difference spectra– Optical properties of all of the bound ligands were measured with an Agilent 8453 diode array UV/VIS spectrophotometer 1 min after addition to isolated enzyme in 30 mM BTP, 0.1 mM EDTA, 0.01% Anapoe $C_{12}E_9$. Optical spectra were recorded at 25 ^{o}C in 50 mM HEPES, 100 mM NaCl, 0.01% Thesit using 1.25 mg/ml of isolated and activated *E. coli* QFR. Upon addition of the ligand, a spectrum was recorded and the spectrum of oxidized enzyme subtracted. Each spectrum represents the addition of the different ligands at the concentration of, 5 mM fumarate, 50 µM oxaloacetate, 4 mM malonate 12 mM glutarate, 50 mM citrate, and 0.1 mM 3-NP which was added from an alkaline solution. The spectra were recorded 10 min after the addition of the ligand. Inhibition of the enzyme by 3-

103

NP was determined as described by adding a final concentration of 0.2 mM 3-NP from a pH 10.0 solution to activated QFR (pH 8.0) and measuring kinetic and optical properties at pH 8.0.

Mass-spectrometry of 3-nitropropionate incubated QFR– QFR at (10 mg/mL) in 20 mM glycine pH 10.0, 0.1 mM EDTA and 0.05% $C_{12}E_9$ was incubated with 1 mM 3-NP for 1 hr on ice in a buffer consisting of 20 mM glycine pH 10.0, and 0.05% w/v $C_{12}E_9$ detergent and was incubated on ice for 1 hr. The QFR subunits were separated on a NuPAGE SDS gel (Invitrogen). The 66 kDa FrdA subunit was manually excised and digested with trypsin for 2 hrs at 37°C. The resulting peptide mixture was separated with a microcapillary HPLC system (Eksigent 1D plus with AS1 autosampler) using an 11 cm x 100 μm C18 reversed phase column (Jupiter C18, 5 μm, Phenomonex) packed directly into a nanospray emitter tip. Using a nanospray source, this was interfaced with either a nominal mass resolution LTQ or high resolution LTQ-orbitrap (Thermo Fisher) mass spectrometer where data dependent tandem (MS/MS) and MS^n spectra were collected throughout a 90 min separation. These spectra were searched against an *E. coli* protein database considering potential amino acid mass differentials corresponding to 3-NP adducts using SEQUEST (Thermo Electron, (18)). Subsequent injections targeting potentially modified peptides were also performed; this included the targeting of normal and stable isotope labeled 3-NP adducts using the LTQ-orbitrap. Later, it was determined that adduct formation could occur at physiological pH. As a result, the analysis of ^{15}N-labeled 3-NP adduct was performed with a modified pre-incubation

procedure where 10 mg/mL QFR was incubated with 1 mM ^{15}N labeled 3-NP in a buffer consisting of 20 mM Tris pH 7.4, 0.1 mM EDTA, and 0.05% $C_{12}E_9$.

Synthesis of isotope labeled 3-NP derivatives– 3-Bromopropionic acid (250 mg, 1.63 mmol), Na^{15}NO$_2$ (206 mg, 2.94 mmol, 98% ^{15}N), phloroglucinol (227 mg, 1.80 mmol), and DMF (3.3 mL) were added to a flame-dried round bottom flask. The reaction mixture was stirred at room temperature for 22 h, and then poured onto ice water and extracted with diethyl ether. The combined organic layers were dried over MgSO$_4$, filtered, and concentrated. A portion of the residue was sublimed (80 °C, 1 Torr) to yield 16 mg of the yellow crystalline product. Label incorporation, sample purity, and confirmation of structure were determined by NMR: ^{1}H NMR (400 MHz, CDCl$_3$) δ 4.66 (td, *J* = 6.0, 2.4 Hz, 2H), 3.06 (td, *J* = 6.4, 4.0 Hz, 2H); ^{13}C NMR (100 MHz, CDCl$_3$) ppm 174.3, 69.3, 30.6; ^{15}N NMR (60 MHz, CDCl$_3$) ppm 379.5.

Crystallization of the E. coli QFR with ligands– All crystallizations of QFR used the hanging drop vapor diffusion method at 22 °C and crystallization conditions modified from those previously described (19). QFR was co-crystallized with fumarate in 12.5% polyethylene glycol (PEG) 8000, 85 mM MgCH$_3$COO, 100 mM NaCitrate pH 5.8, 0.1% DTT, 0.1mM EDTA, and 5mM fumarate. QFR was co-crystallized with oxaloacetate in 12% PEG 5000 monomethyl ether (MME), 125 mM MgCH$_3$COO, 100 mM NaCitrate pH 5.8, 0.1% DTT, 0.1 mM EDTA, and 0.5 mM oxaloacetate. QFR was co-crystallized with glutarate in 14.5% PEG 8000, 125 mM MgCH$_3$COO, 95 mM NaCitrate pH 5.8, 0.1% DTT, 0.1 mM EDTA, and 10 mM glutarate. For co-crystallization of QFR with 3-NP, prior to crystallization, QFR was incubated with a 3-fold molar excess of 3-NP on ice for 1 hr at pH 10.0. Crystals

were grown in 10% PEG 5000 MME, 250 mM MgCH$_3$COO, 100 mM NaCitrate pH

5.8, 0.1% DTT, and 0.1 mM EDTA. All crystals formed in the orthorhombic space

group P2$_1$2$_1$2$_1$ with unit cell dimensions and data collection statistics shown in Table

1.

TABLE 4. Crystallographic data collection and refinement statistics

	+ Fumarate	+Glutarate	+3-NP	+Oxaloacetate
Wavelength	1.0 Å	1.03 Å	1.0 Å	1.2 Å
Beamline	SSRL 9-2	SSRL 11-1	ESRF ID-13	SSRL 9-2
Resolution	2.80 Å	3.05 Å	3.10 Å	3.35 Å
Completeness	94.9% (95.6%)	95.0% (96.6%)	92.9% (78.2%)	88.9% (73.9%)
I/σ	23.4 (5.8)	10.7 (3.5)	16.8 (4.1)	10.0 (2.7)
R$_{sym}$[a]	0.089 (.298)	0.099 (.296)	0.098 (0.256)	0.099 (0.237)
Refinement statistics				
R$_{cryst}$[b]	0.249	0.248	0.255	0.220
R$_{free}$	0.272	0.284	0.279	0.261
RMS deviation bonds (Å)	0.014	0.014	0.007	0.011
RMS deviation angles (°)	1.854	1.888	1.651	1.868

Values in parenthesis indicate statistics for the highest shell.

[a]R$_{sym}$ = Σ |I$_i$ - <I>|/ Σ I$_i$ where I is intensity, "I" is the ith measurement, and <I> is the weighted mean of I.

[b]R$_{cryst}$ = Σ ||F$_{obs}$| - |F$_{calc}$||/ Σ F$_{obs}$. R$_{free}$ is the same as R$_{cryst}$ for a set of data omitted from the refinement.

Data collection and processing– Crystallographic data were collected at the

beamlines listed in Table 1 at -173 °C after the addition of 30% ethylene glycol to the

crystallization conditions as a cryoprotectant. Data were processed using DENZO,

SCALEPACK (20), HKL2000 (21), and the CCP4 suite of programs (22). Since

crystals were isomorphous with crystals from known structures of QFR, rigid body

refinement was performed with CNS (23) to determine initial phases. The starting

model was QFR in complex with heptyl quinoline N-oxide (PDBID 1KF6, (24)) for the

3-NP and glutarate co-structures, a QFR in complex with citrate (PDBID 2B76; (17))

for the fumarate co-structure, and the finished glutarate co-structure for the

oxaloacetate co-structure. Iterative rounds of model rebuilding were performed in O

(25) and COOT (26). Omit maps, starting with segments of 50 amino acids in the

initial stages of refinement and eventually progressing to 250 amino acid segments,

were used extensively to minimize electron density map bias to the starting model.

Refinement and map calculations were performed with Refmac5 (22,27), CNS, and

Phenix with loose 2-fold non-crystallographic symmetry restraints used in the

fumarate structure and translation-liberation-screw (TLS) refinement (28) in all the

structures. TLS refinement parameters were determined with the TLSMD server

(29). Figures 1A and 2 were created in the program PyMOL.

Molecular modeling of dicarboxylate binding– QFR co-structures with fumarate,

glutarate, oxaloacetate, and citrate were prepared for modeling with Maestro

(Schrödinger LLC, (30)) by creating a file with only the flavoprotein subunit, the iron

protein subunit, and covalently linked FAD. Protons were added to the QFR

structure with Maestro, and the resultant structure was minimized using the

molecular mechanics force field, OPLS_2005. Ligands were prepared using the

Ligprep module by adding explicit hydrogen atoms. These ligands were then

reinserted into the active site of the minimized protein. The Glide XP subroutine in

Maestro was used for ligand docking and the free energy of binding was estimated

with the extended-precision scoring function (Glide XP)(30). During this phase of the calculation, flexibility of the ligand was allowed, while the protein was held rigid. Ligand binding and orientation were verified using omit maps and simulated annealing omit maps to minimize phase bias. Placement of multiple conformations of each ligand were attempted and were minimized using real space refinement in Coot. Docking of each ligand was tested using Glide to ensure that a physically reasonable binding orientation had been found (Fig. 26).

Results

QFR activity can be inhibited both *in vivo* and *in vitro* by dicarboxylates or carboxynitro molecules structurally similar to fumarate (Fig. 25). In this study, we investigate the determinants for binding and catalysis by identifying the interactions between QFR and the substrate fumarate, or the inhibitors oxaloacetate, glutarate, and 3-nitropropionate.

Structural details of fumarate binding with the E. coli QFR– Co-crystallization of QFR with fumarate resulted in the appearance of clear electron density within the enzyme active site. This density is consistent with an alignment of the C2-C3 double bond parallel to the C(4a)-N5 bond of the isoalloxazine ring of FAD (31). Notably, a torsioned conformation of fumarate is observed (Fig. 27), where the carboxylates are oriented 54° relative to one another, compared to the 0° orientation found in planar molecules.

Figure 26. Electron density of ligand binding to the active site. The active site of QFR is shown with nitrogen atoms colored *blue*, oxygen atoms colored *red,* carbons from the protein colored *grey*, carbons from the FAD colored *yellow*, and carbons from each bound ligand colored *cyan*. A. Active site of QFR co-crystallized with fumarate. B. Active site of QFR co-crystallized with oxaloacetate. C. Active site of QFR co-crystallized with 3-nitropropionate. D. Active site of QFR co-crystallized with glutarate.

Figure 27. Fumarate binding to the active site. The active site of QFR is shown with nitrogen atoms colored *blue*, oxygen atoms colored *red,* carbons from the protein colored *grey*, carbons from the FAD colored *yellow*, and carbons from each bound ligand colored *cyan*. Relevant inter-atomic distances, including potential hydrogen bonds, are indicated along a dashed line. A. Active site of QFR co-crystallized with fumarate.

Torsion of fumarate is predicted to have a significant electronic effect, with the C2

carbon bearing the twisted carboxylate becoming a better hydride acceptor as

electrons are better allowed to localize to the carbonyl (31,32). Hydride transfer thus presumably occurs between N5 of FAD and C2 of fumarate, and the distance between these atoms is 4 Å. Subsequent proton transfer is predicted to occur between the side chain of Arg-A287 and the C3 of fumarate. Of note, an ordered water molecule mediates the interaction between the C3 position of fumarate and the proton shuttle, Arg-A287. Seven putative hydrogen-bonding contacts stabilize fumarate in this torsioned conformation (Fig. 28).

The possibility of enzymatic turnover or photoreduction during data collection precludes positive identification of this dicarboxylate as fumarate with crystallography alone. To support the assignment of the ligand as fumarate (rather than citrate from the crystallization conditions, or the product succinate), optical difference spectra were collected. The binding of fumarate to QFR results in the appearance of peaks at 390 nm and 500 nm in the FAD absorption spectrum (Fig. 30). The addition of QFR to the crystallization buffer induced optical changes that indicate replacement of oxaloacetate with citrate. Upon addition of 5 mM fumarate, the concentration used during co-crystallization, a typical optical spectrum reflecting the replacement of citrate with fumarate was observed (data not shown).

Structural details of QFR inhibition by oxaloacetate– The structure of QFR in complex with oxaloacetate shows that this dicarboxylate inhibitor binds to QFR with a position similar to that of fumarate (Fig. 28).
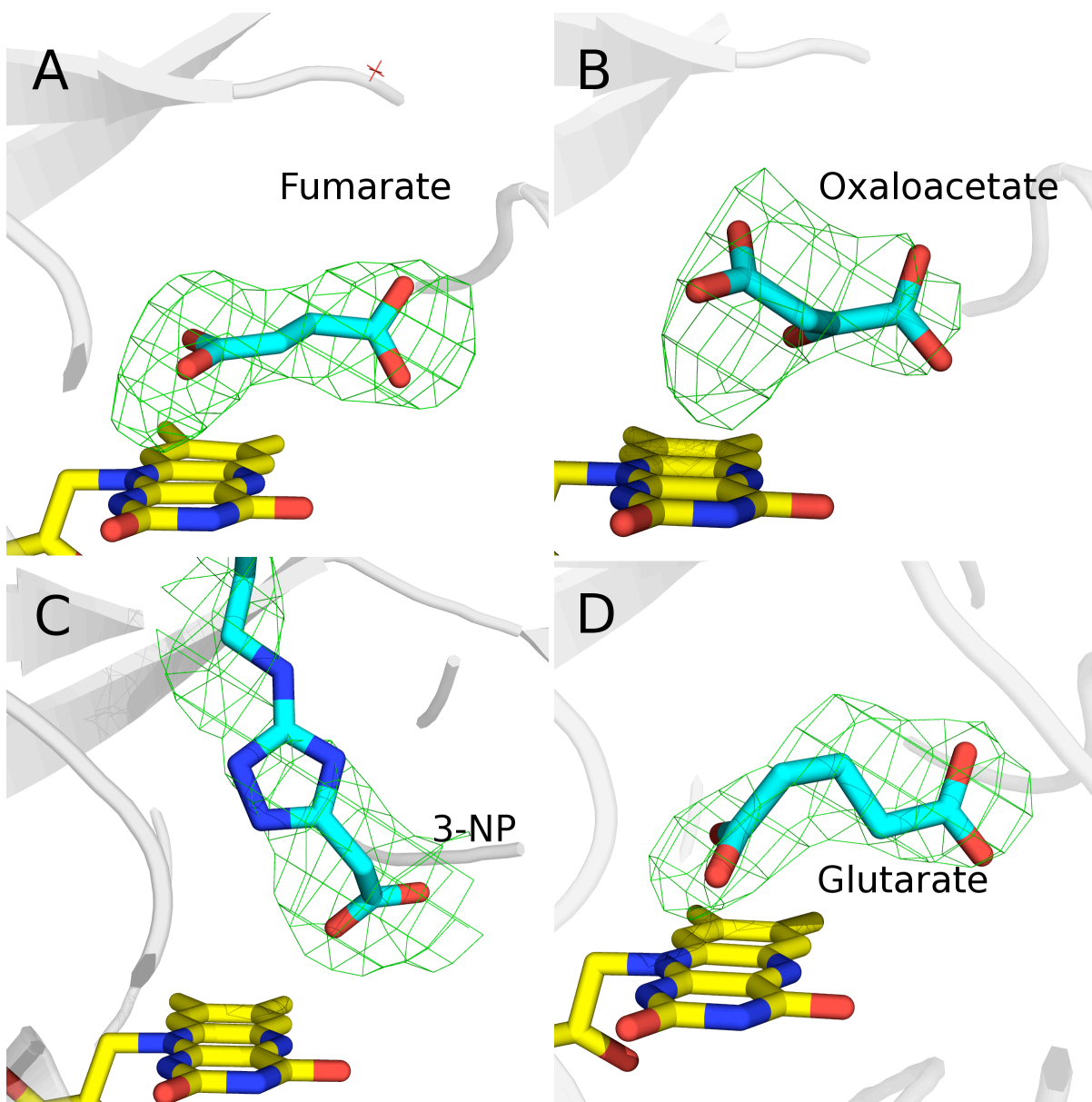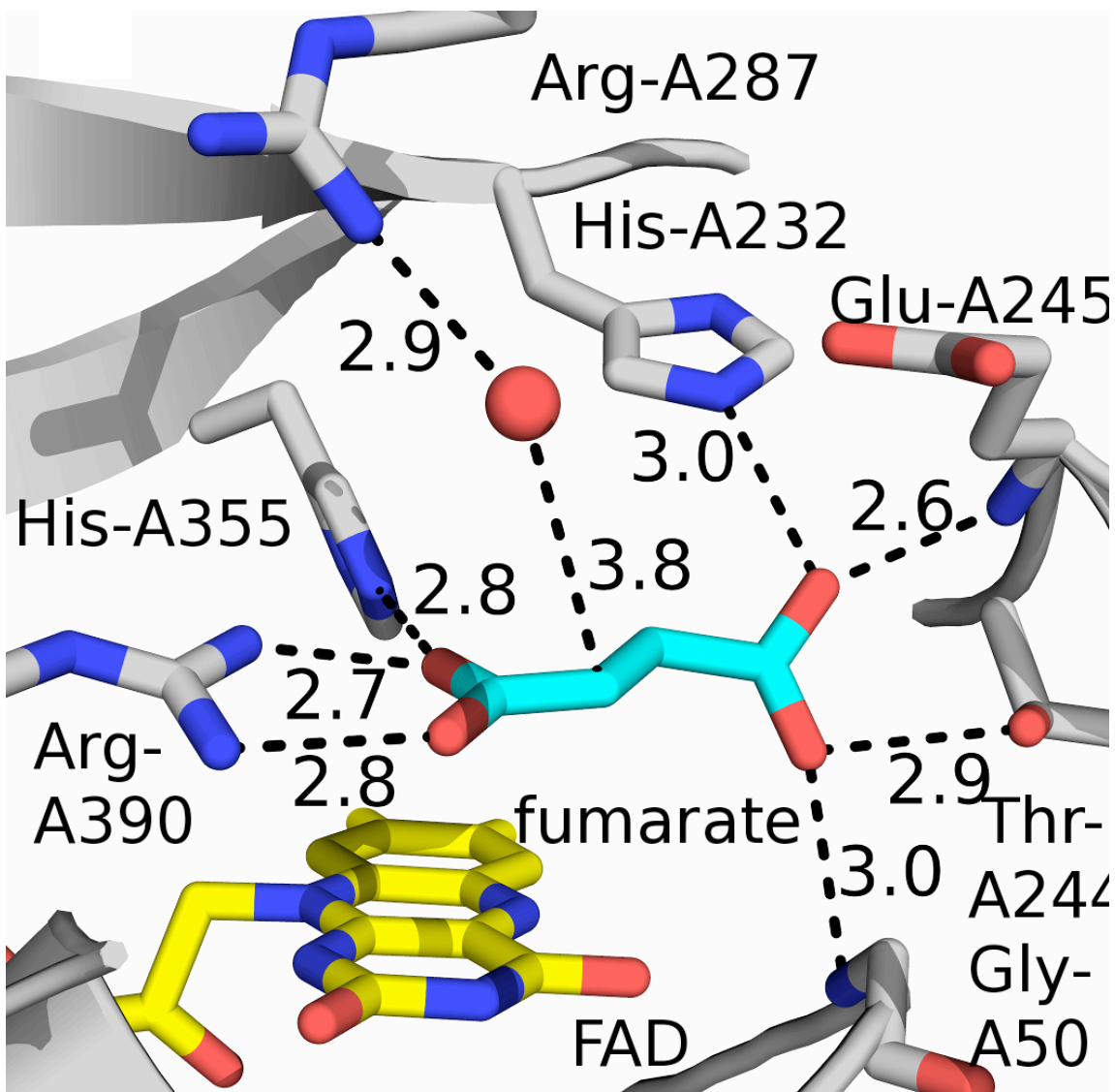
Figure 28. Oxaloacetate binding to the active site. The active site of QFR is shown with nitrogen atoms colored *blue*, oxygen atoms colored *red,* carbons from the protein colored *grey*, carbons from the FAD colored *yellow*, and carbons from each bound ligand colored *cyan*. Relevant inter-atomic distances, including potential hydrogen bonds, are indicated along a dashed line. A. Active site of QFR co-crystallized with fumarate.

In this binding mode, the C2-C3 bond is parallel to C(4a)-N5 of the FAD isoalloxazine ring, similar to the orientation of the C2-C3 double bond of fumarate in the co-structure of fumarate with QFR. In addition, the oxaloacetate carbonyl is

positioned laterally such that C2=O carbonyl is nearly parallel with the adjacent N5-C(5a) bond. This structural feature possibly underlies the charge-transfer interaction, which results in the formation of a broad peak in the optical spectrum centered at 550 nm (Fig. 30). Interestingly, while the apparent affinity of oxaloacetate to QFR is much greater than that of fumarate, only three putative hydrogen bonds stabilize oxaloacetate in this binding position (Fig. 28). This suggests that the charge-transfer interaction has a major contribution to binding affinity.

Structural basis of covalent inhibition by 3-NP– Differences in inhibition between SQR and QFR have mechanistic implications since each of these enzymes optimally catalyzes the reaction in one direction. As a result, we tested the effects of 3-NP addition on both wild-type QFR and the FrdA E49Q variant of QFR, which has previously been shown to have altered catalytic efficiency for fumarate reduction and succinate oxidation (17). Crystals of the FrdA E49Q variant of QFR in complex with 3-NP exhibited superior diffraction as compared to crystals of wild-type QFR in complex with 3-NP. As a result, crystals of the mutant enzyme were used for all subsequent structural analyses.

In the structure of 3-NP with the E49Q variant of QFR, electron density contiguous with Arg-A287 is evident, consistent with the formation of a covalent adduct between 3-NP and Arg-A287. This density is in the same location as the ordered solvent molecule observed in the co-structure between QFR and fumarate (Fig. 27). Proposed adducts from the literature were used as starting models to interpret the active site density, including 3-NP as a non-covalent inhibitor (14), 3-NP forming an adduct to Arg-A287 (13), 3-NP forming a covalent adduct to the FAD
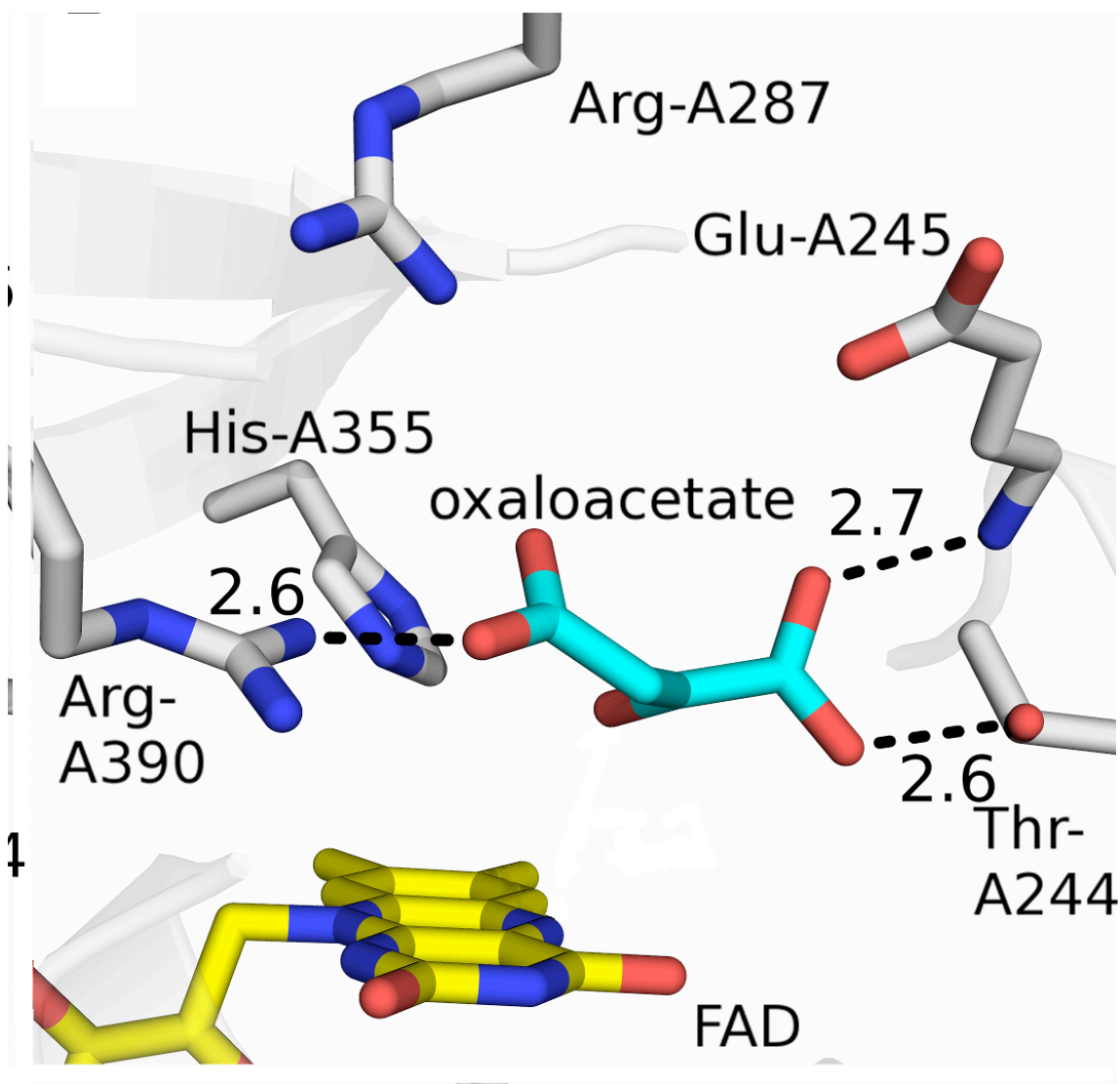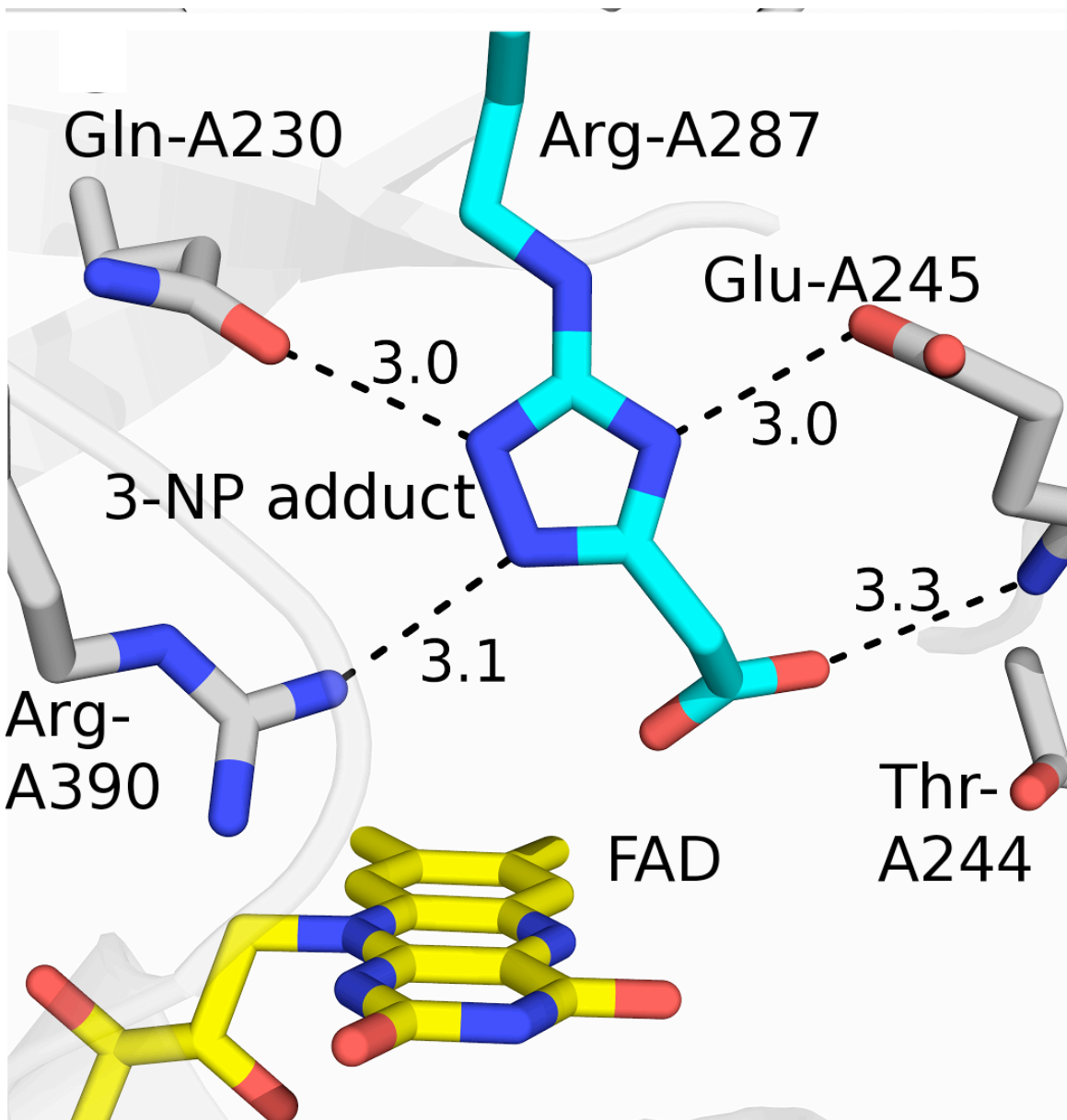
Figure 29. 3-NP binding to the active site. The active site of QFR is shown with nitrogen atoms colored *blue*, oxygen atoms colored *red,* carbons from the protein colored *grey*, carbons from the FAD colored *yellow*, and carbons from each bound ligand colored *cyan*. Relevant inter-atomic distances, including potential hydrogen bonds, are indicated along a dashed line. A. Active site of QFR co-crystallized with fumarate.

(12), and mixed states combining these possibilities. A 3-NP adduct to Arg-A287

modeled as a 5-membered 2,4,5-triazole structure best explains the density (Fig.

29), in close agreement with the crystal structure of avian complex II in complex with 3-NP (13). Notably, the side chain of adducted Arg-A287 displays an extended conformation when compared to the position of Arg-A287 from citrate bound QFR (PDBID: 2B76; (17)). This results in a 2.8 Å displacement of the uanidine group toward the FAD. An electrostatic contact between the terminal carboxylate of 3-NP and the N5 of FAD stabilizes the adduct. Further, the triazole ring makes putative hydrogen bond contacts to three side chains in the active site, with likely hydrogen-bonding contacts between the NH1 of the adduct and the $O_\varepsilon 1$ atom on Gln-A230, between the NH2 of the adduct and the $O_\varepsilon 1$ carbonyl atom on Glu-A245, and between the N13 of the adduct and the Nh2 of Arg-A390.

While the structure of the FrdA E49Q variant of QFR in complex with 3-NP demonstrates that the binding mode is distinctly different from that of fumarate, intriguingly, the addition of 3-NP to QFR induces changes to the optical spectrum that are similar to those observed with the addition of fumarate, with peaks appearing at 400 nm and 500 nm (Fig. 30).
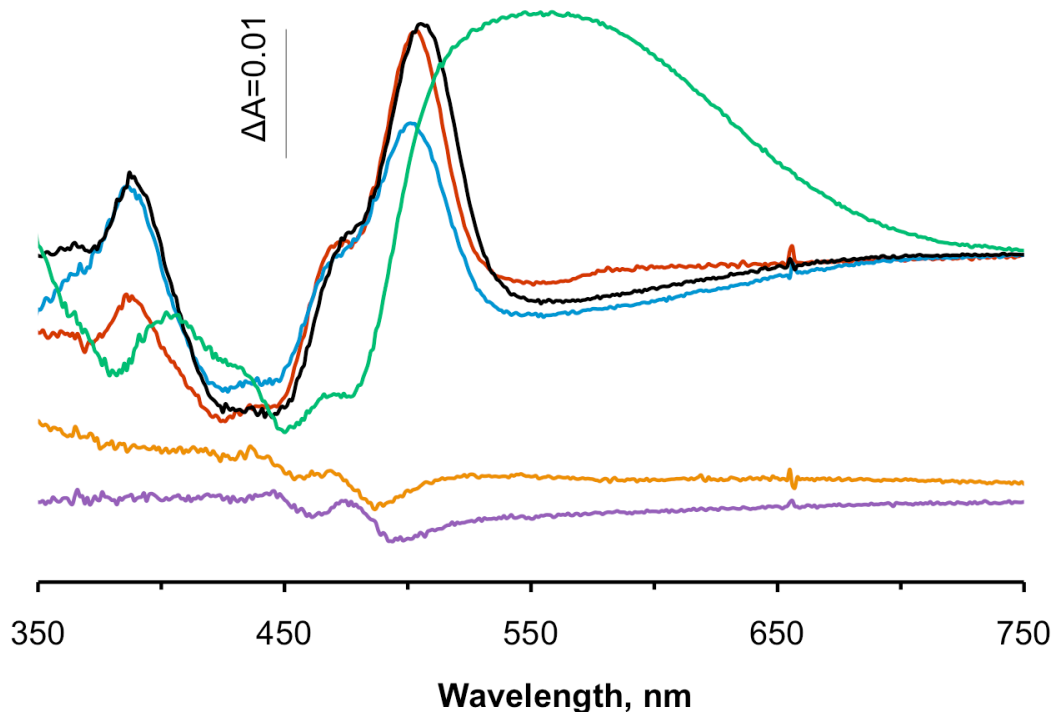
Figure 30. Optical difference absorption spectroscopy of QFR after the addition of ligands. Spectra are the difference between the spectrum of the enzyme after addition of each ligand and the spectrum of the oxidized enzyme. The spectra are
colored blue for fumarate, green for oxaloacetate, purple for glutarate, orange for citrate, black for 3-nitropropionate and red for malonate.

This observation is consistent with previous suggestions that 3-NP could act as an alternative substrate for complex II enzymes (8, 12). Therefore to determine whether catalytic oxidation or reduction of 3-NP takes place during adduct formation, the optical and catalytic properties of the 3-NP and *E. coli* QFR interaction were investigated over time. Upon addition of an equimolar ratio of 3-NP to wild-type *E. coli* QFR, 3-NP induces optical changes in the spectrum of activated QFR (Fig. 31).

The time course of these optical changes matches the change in catalytic activity, suggesting that 3-NP is, indeed, a substrate of QFR and that oxidation by FAD forms the species that attacks Arg-A287 to result in the formation of the 3-NP-Arg-A287 adduct. No further optical changes due to FAD interaction with a ligand nor oxidase activity was observed upon addition of a second equimolar dose of 3-NP. This indicates that a single catalytic turnover of QFR is a requirement for formation of the 3-NP-Arg adduct.

To determine whether catalytic oxidization or reduction of 3-NP takes place during adduct formation, the optical and catalytic properties of the 3-NP and *E. coli* QFR interaction were investigated over time. Upon addition of an equimolar ratio of 3-NP to wild-type *E. coli* QFR, 3-NP induces optical changes in the spectrum of activated QFR (Fig. 31).
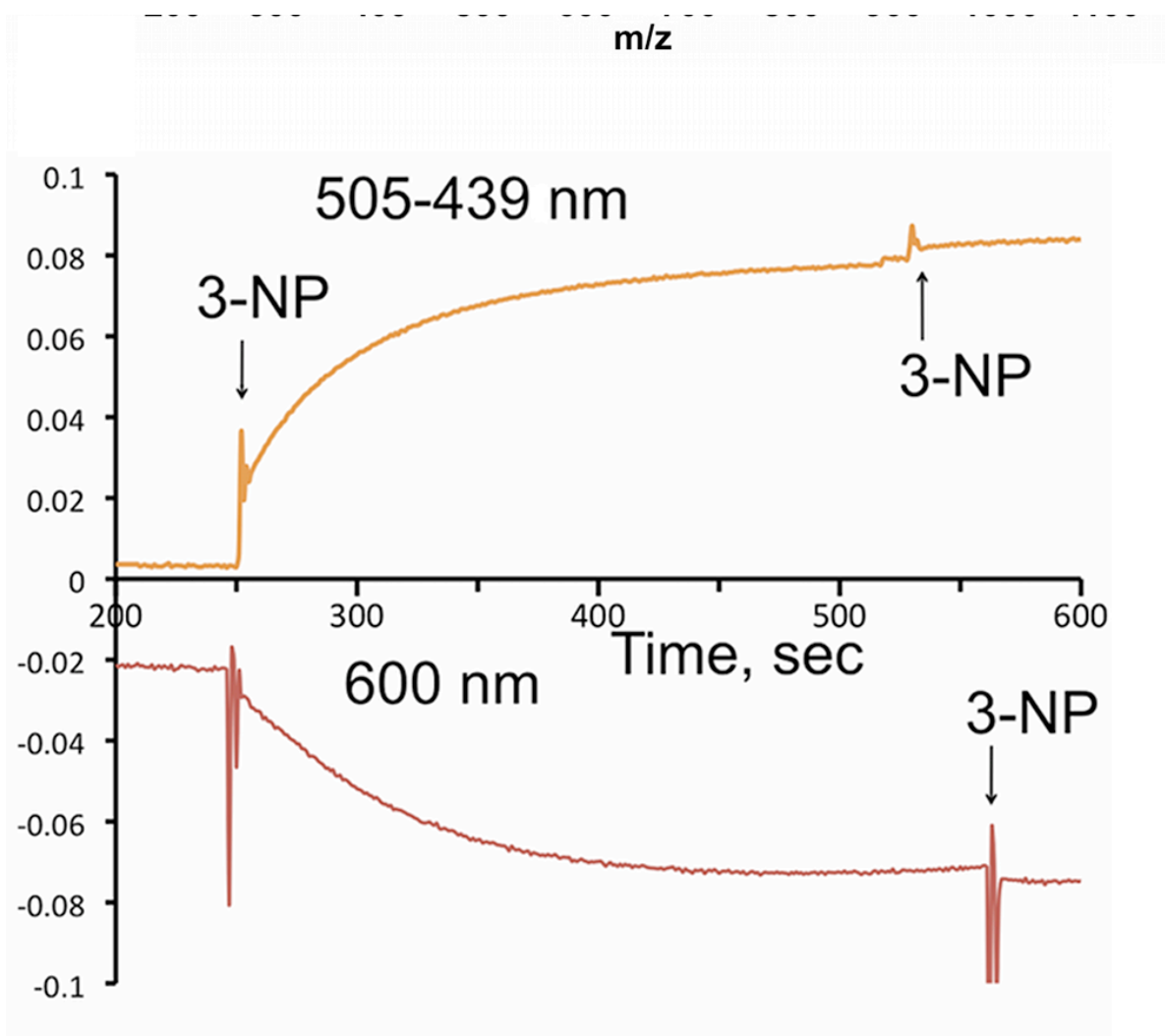
Figure 31. Optical spectrum following the reduction of FAD (*orange*) or consumption of DCIP (*dark red*) following 3-NP addition. Activated QFR (~5 µM) was added to 50 mM BTP pH 8.0, 30°C. 3-NP (0.2 mM final conc.) was added from a pH 10.0 solution and changes in the optical spectrum were monitored at 505-439 nm (upper trace). (Lower trace) 50 µM DCIP was added to the cuvette at the same QFR concentration (5 µM) and reduction of DCIP was monitored at 600 nm upon addition of 3-NP from the pH 10 solution. The arrow in both the upper and lower trace indicates that the addition of a second equivalent of 3-NP did not cause additional spectral changes indicating that one equivalent of 3-NP is sufficient to inhibit the enzyme. Note, the loss of enzyme activity corresponds to a 1:1 molar ratio of 3-NP to QFR.

118
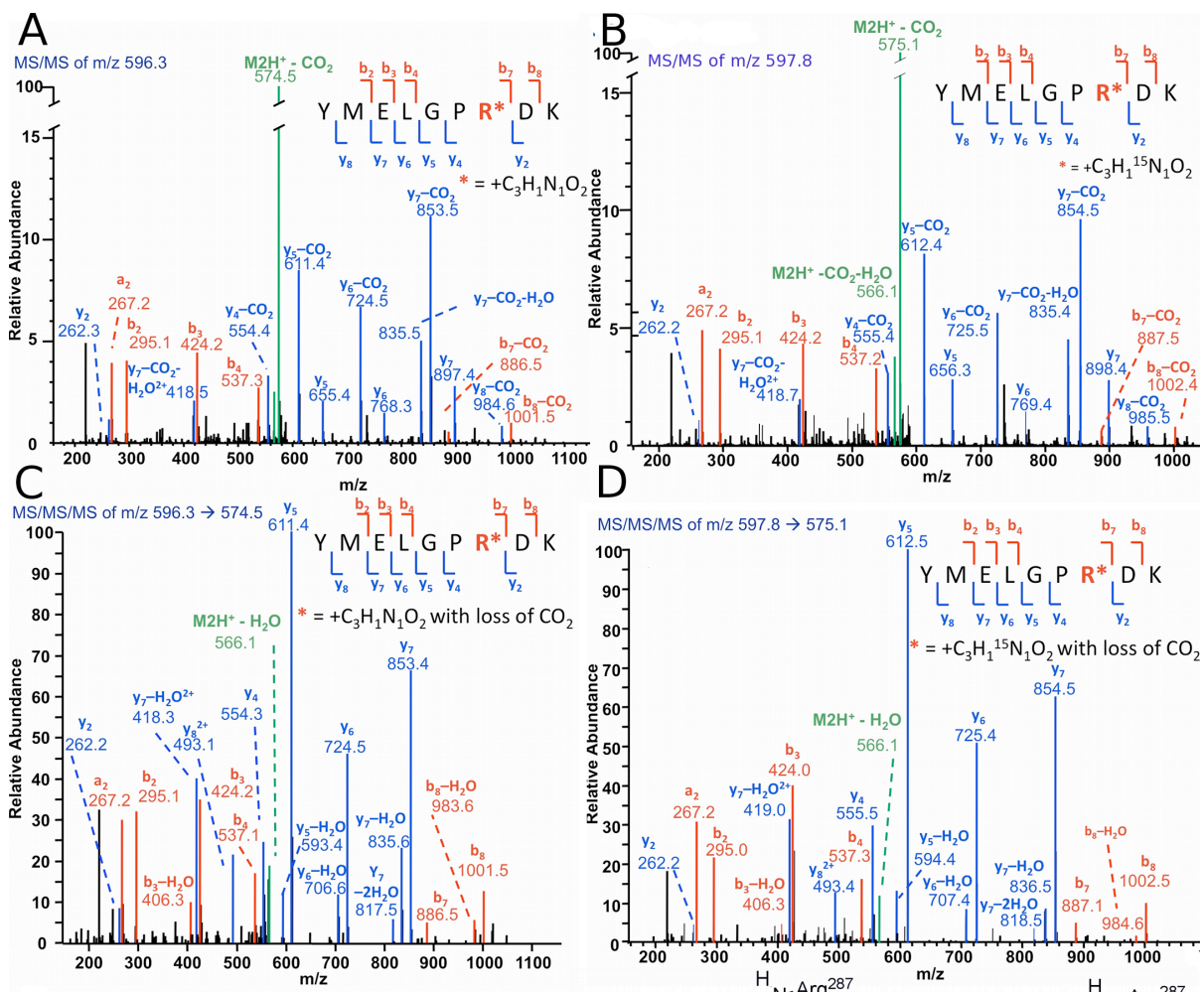
Figure 32. Identification of the 3-NP adduct and a proposed mechanism for its formation. A. Tandem mass spectrum (MS/MS) from analysis of fragmentation of the YMELGPR*DK peptide adducted to 3-NP. B. An MS/MS/MS (MS^3) spectrum of the $-CO_2$ neutral loss fragment isolated from 3-NP adducted peptide fragmentation (m/z 574.5 from A). C. Tandem mass spectrum obtained from analysis of fragmentation of the YMELGPR*DK peptide adducted to ^{15}N labeled 3-NP. D. An MS^3 spectrum of the $-CO_2$ neutral loss fragment isolated from the ^{15}N labeled 3-NP adducted peptide fragmentation (m/z 575.1 from B).

The time course of these optical changes matches the change in catalytic activity, suggesting that 3-NP is, indeed, a substrate of QFR and that oxidation by FAD forms the species that attacks Arg-A287 to result in the formation of the 3-NP-Arg-A287 adduct. No further FAD reduction nor catalytic inhibition was observed upon

addition

	K_m, mM	K_i, mM	

of   a   second

equimolar dose of 3-NP. This indicates that a single catalytic turnover of QFR is a

requirement for formation of the 3-NP-Arg adduct.

Verification of the chemical identity of the 3-NP adduct by mass spectrometry– The

location of the 3-NP adduct was verified using LC-MS/MS of trypsinized FrdA

pretreated with 3-NP.   The 3-NP adducted peptide was identified as a doubly

charged 596.3 m/z ion with 3-NP adduction with Arg-A287 (Fig. 32).

Further fragmentation identified the neutral loss of CO_2 in the MS^3 spectrum (Fig.

4C) strongly suggesting that the adduct is oriented with the nitro group coupled to

Arg-A287. Since direct coupling of a nitroalkane and amine is rare and elimination of

nitrous acid (HNO_2) is much more favorable, it was important to determine

unambiguously whether the nitrogen of 3-NP was incorporated into the triazole. ^{15}N

labeled 3-NP (98% ^{15}N) was synthesized and the mass spectral analysis was

repeated. The MS-MS and MS^3 analyses exhibited a shift of 1 Da for multiple

fragment ion peaks, demonstrating incorporation of ^{15}N into the triazole adduct (Fig.

4B,D).

S*tructural basis for inhibition by glutarate*– Increased systemic glutarate levels have

been correlated with decreased complex II activity *in vivo* (7), but have not

previously been shown to inhibit the enzyme directly. Activity of QFR was measured

in the presence and absence of glutarate, which demonstrates that this

dicarboxylate acts as a competitive inhibitor with a K_i of 1.9 mM (Table 3).

Fumarate	0.02*	
Succinate	0.5*	
Oxaloacetate		0.0003*
Malonate		0.025*
Citrate		20
Glutarate		1.9

Table 5. Comparison of the apparent affinity values of dicarboxylates to *E. coli* QFR. * ref. in (17).

The structure of QFR in complex with glutarate shows a torsioned conformation of the glutarate (Fig. 2D). The angle between the dicarboxylates is 87°, larger than in the fumarate co-structure. In this binding mode, the torsion is distributed along a greater number of bonds, and the C2 atom bends away from the rest of the ligand, causing the C2-C3 and C3-C4 bonds to buckle outward from the FAD. As a result, none of the carbon-carbon bonds of glutarate lie along the C(4a)-N5 of the FAD isoalloxazine ring. Glutarate does not induce changes in the FAD optical difference spectrum (Fig. 30), which supports the hypothesis that the alignment of a bond along the C(4a)-N5 bond of FAD underlies these spectral changes. Stabilizing glutarate in this conformation are 5 putative hydrogen-bonding contacts (Fig. 33).

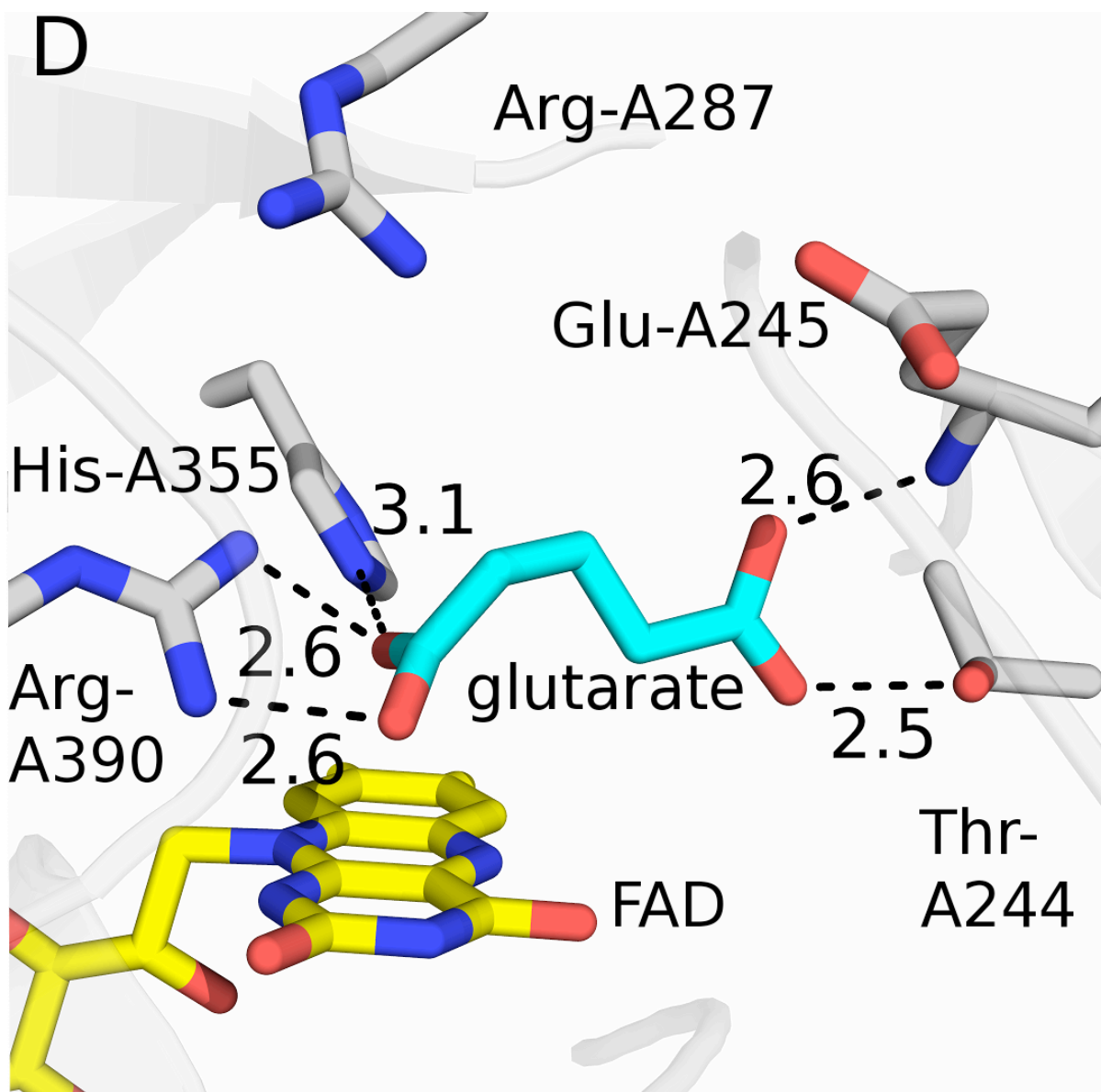Figure 33. Glutarate binding to the active site. The active site of QFR is shown with nitrogen atoms colored *blue*, oxygen atoms colored *red,* carbons from the protein colored *grey*, carbons from the FAD colored *yellow*, and carbons from each bound ligand colored *cyan*. Relevant inter-atomic distances, including potential hydrogen bonds, are indicated along a dashed line. A. Active site of QFR co-crystallized with fumarate.

Docking calculations– Ligand docking calculations in Glide resulted in ligand poses consistent with the experimentally observed binding conformations. From these binding poses, an overall binding score was calculated with energetic contributions from internally calculated coulombic interactions, hydrogen bonding interactions, and van der Waals interactions (Table 6).

Ligand	Total Score	H-bonding	Coulombic	Van der Waals
Fumarate	-2.39	-3.9	-24.1	-7.4
Oxaloacetate	-4.37	-3.9	-21.8	-12.1
Glutarate	-10.6	-4.3	-23.6	-12.7
Citrate	-8.49	-2.8	-16.3	-11.1

Table 6. Binding scores of ligands to the *E. coli* QFR as calculated in Glide XP

Surprisingly, these simulations predict that fumarate binds with the least favorable coulombic interactions of all ligands tested and the second least favorable electrostatic interactions. However, the calculated van der Waals interactions of fumarate were more favorable than all other ligands tested. The opposite was true in the case of the larger molecule glutarate, which was calculated to have the most favorable electrostatic and hydrogen bonding interactions but the least favorable calculated van der Waals interactions. Citrate binding was also predicted to show unfavorable van der Waals contacts, likely leading to the lowest experimentally-determined apparent affinity of all the ligands tested (Table 6). Oxaloacetate binding

energy was not accurately predicted by the Glide algorithm, which does not take charge transfer interactions into account.

Discussion

Complex II enzymes must perform the challenging tasks of activating a kinetically stable bond while discriminating between structurally and electronically similar substrates. To identify the properties of QFR important for binding and catalytic specificity, structural and spectroscopic analyses of QFR in complex with activatable and non-activatable ligands were compared. Our results demonstrate the importance of geometric constraints on ligand positioning relative to the FAD cofactor in both on-pathway and off-pathway catalysis.

On-pathway catalysis in QFR– Previous studies demonstrate that QFR reduces fumarate to succinate in two distinct steps (33). The first is the rate-limiting hydride transfer from FAD to fumarate, and the second is proton transfer from a nearby side chain. It is hypothesized that the hydride transfer step of this α,β-dehydrogenation reaction is kinetically difficult since the relatively short fumarate lacks extensive resonance structures to delocalize developing charges during catalysis. To overcome this kinetic stability and catalyze hydride transfer, QFR has been proposed to combine multiple geometric and electrostatic mechanisms including: substrate polarization (34), active site desolvation, concerted active site rearrangement (35), and substrate torsion (31,32).

Fumarate binds the *E. coli* QFR in a torsioned conformation (Fig. 27) similar to that observed in co-structures with *Wolinella succinogenes* QFR (31), and soluble homologs of the QFR flavoprotein (32,33), with interdomain rotations likely contributing to the torsioning (35). We predict that this torsioning of fumarate may facilitate catalysis by allowing improved delocalization of electrons between the C2 and the carbonyl to narrow the transition state energy barrier.

Fumarate binding induces the appearance of peaks at 390 nm and 500 nm in the FAD optical spectrum. Similar peaks are observed upon the addition of malonate or 3-NP, but are absent with oxaloacetate, citrate, and glutarate addition (Fig. 30). Inspection of the co-structure of QFR with fumarate suggests that alignment of the chemically reactive C2-C3 bond parallel to the C(4a)-N5 bond of FAD (Fig. 34) could be important for this spectroscopic change and may also be critical for catalysis.
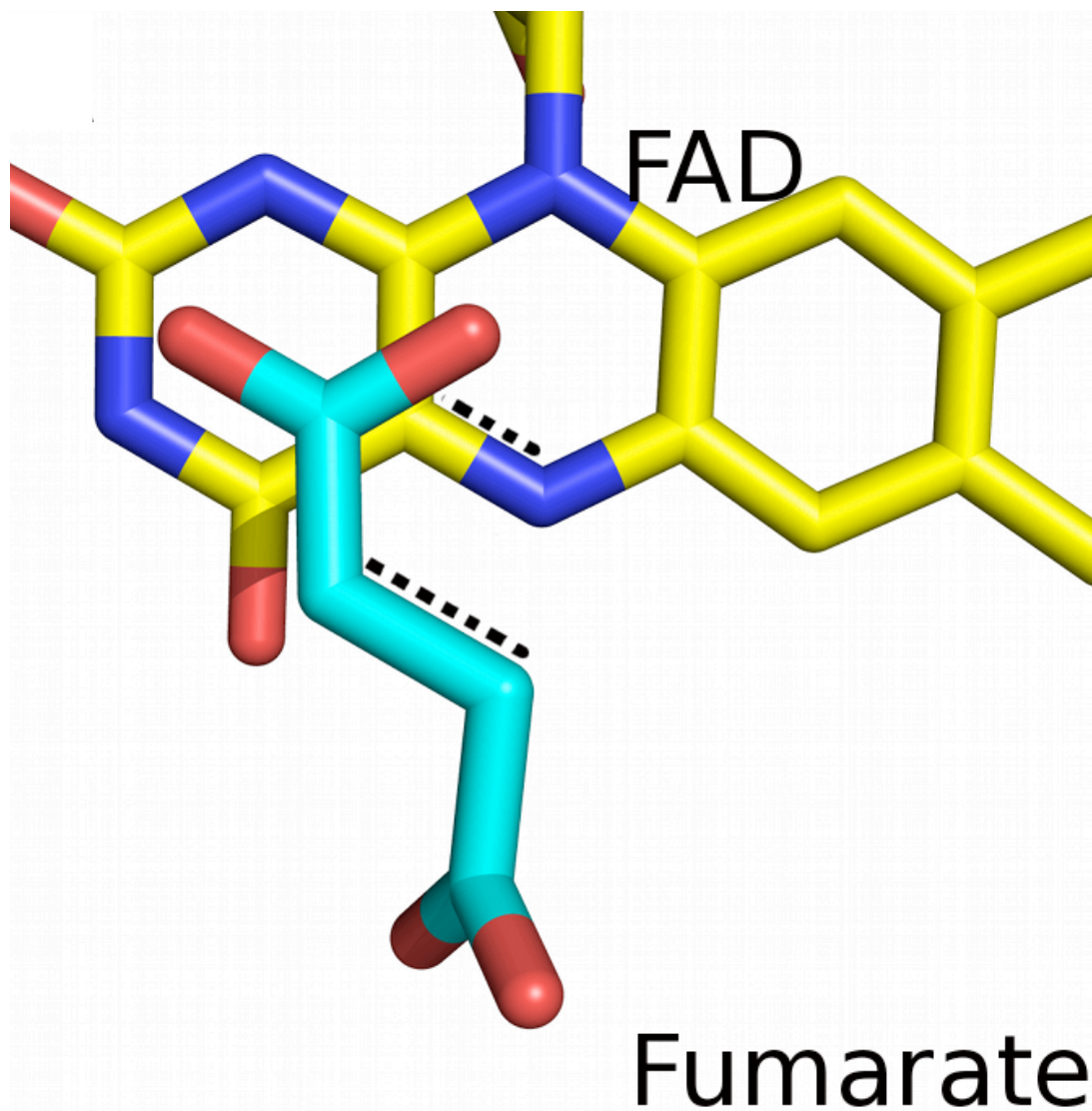
Figure 34. Comparison of substrate binding in flavin-containing enzymes catalyzing a,b-dehydrogenation reactions. Dashes highlight the activated substrate bond and the C(4a)-N5 bond (FAD), which are aligned. In all the figures, nitrogen is colored *blue*, oxygen is colored *red*, FAD carbons are colored *yellow*, and sulfur is colored *tan*. A. The *E. coli* QFR co-crystallized with fumarate. Carbon atoms of the fumarate are colored *cyan*.

While the alignment of the C2-C3 bond of oxaloacetate with the C(4a)-N5 of FAD is also observed in the co-structure (Fig. 37), the additional interaction between the FAD and the carbonyl may modify these spectral features in that case.

A similar alignment of the reactive bond of substrate and FAD is observed in co-complexes of natural substrates with acyl-coA dehydrogenase (PDBID 3MDE; (36)) and D-amino acid oxidase (PDBID 1C0L; (37)), two evolutionarily-unrelated flavoenzymes that similarly house FAD-catalyzed α,β-dehydrogenation reactions (Fig. 35 C,D).
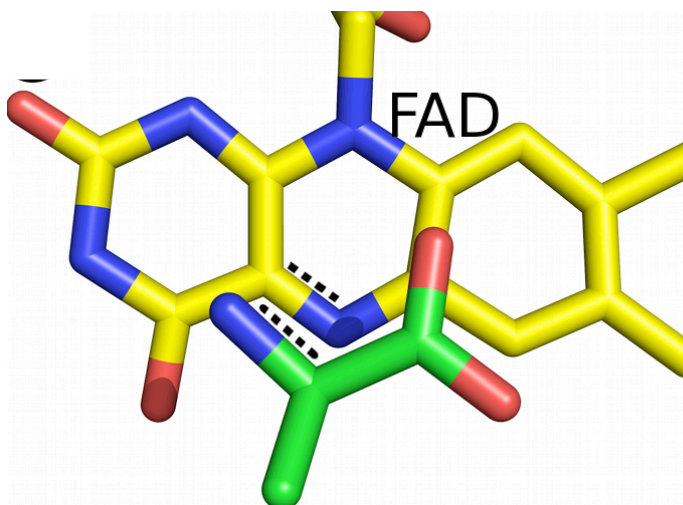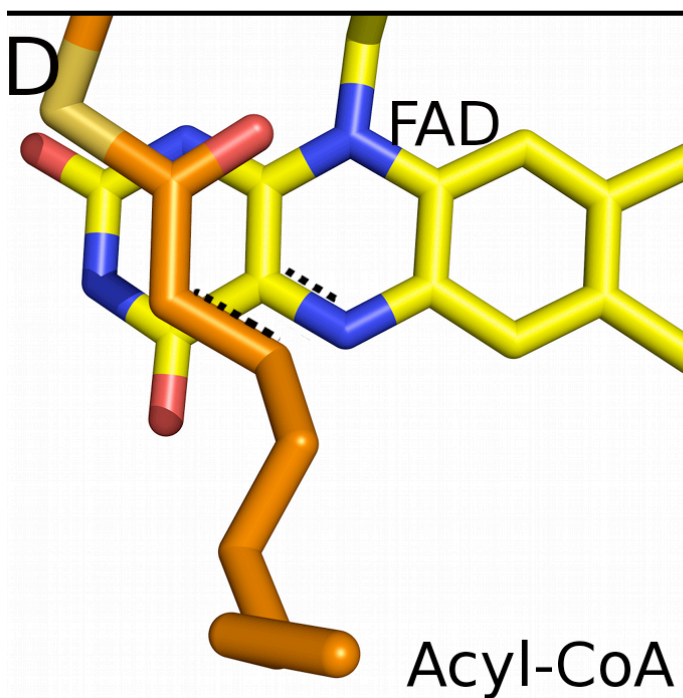
Figure 35. Comparisons of other dehydrogenation ligands. D-amino acid oxidase co-crystallized with D-alanine (PDBID: 1C0L; (33)). Carbon atoms of D-alanine are colored *green* D. Porcine mitochondrial medium-chain acyl-coA dehydrogenase co-crystallized with acyl-CoA (PDBID: 3MDE; (32)). Carbon atoms of acyl-CoA are colored *orange*. E. In all the figures, nitrogen is colored *blue*, oxygen is colored *red*, FAD carbons are colored *yellow*, and sulfur is colored *tan*

This conservation of substrate orientation across the isoalloxazine ring of three unrelated enzymes suggests that it is ideal for catalysis. Calculations show that the FAD HOMO consists largely of a dominant contribution from the N5 and C(4a) atoms in lumiflavin (38). Positioning of fumarate parallel to the C(4a)-N5 axis would be predicted to maximize the HOMO-LUMO overlap of the fumarate π^* anti-bonding orbital and the FAD HOMO (Fig. 36), the likely conduit for hydride transfer from the N5 position of FAD.

Figure 36. A model of the LUMO of fumarate and HOMO of FAD illustrating the predicted orbital overlap. Blue and gold represent different phases of the orbital wavefunction.

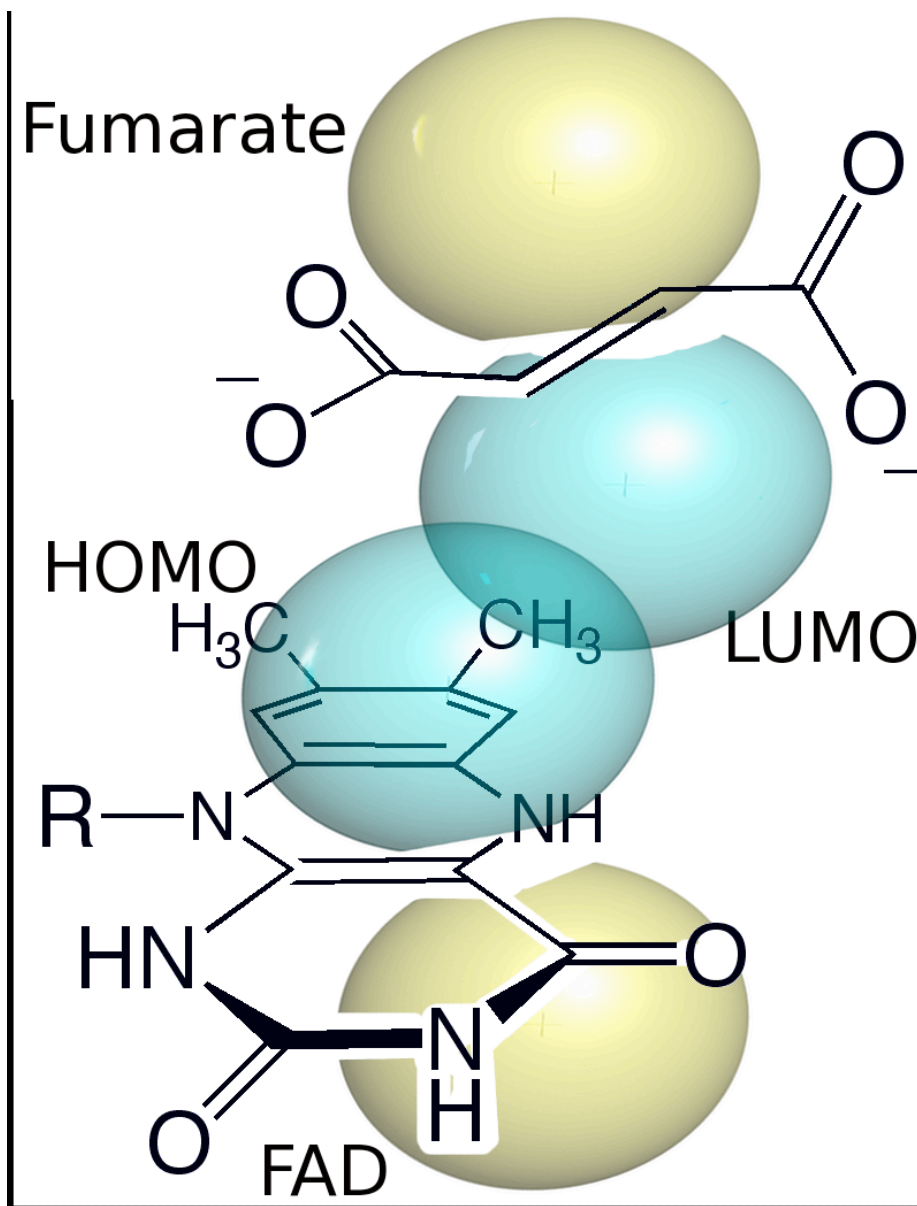A similar orbital overlap was also proposed to be important for inducing spectral changes in FAD of D-amino acid oxidase upon ligand binding to substrate (39). This observation is consistent with an orbital steering mechanism, which holds that optimal substrate orientation contributes to catalytic efficiency by maximizing overlaps of bonding orbitals and minimizing overlaps of non-bonding orbitals (40). Subtle geometric changes were shown to be important for hydride transfer upon subtle perturbations in iso-citrate dehydrogenase, even after controlling for distance changes and electrostatic differences (41), and likely play a role in the catalytic mechanism of QFR.

Following hydride transfer from FAD, a proton is transferred from the side chain of an active site residue. In the *Shewanella frigidimarina* soluble fumarate reductase, an elegant combination of site-directed mutagenesis, X-ray crystallography, and kinetics demonstrated that an active site arginine structurally equivalent to Arg-A287 from the *E. coli* QFR acts as the proton shuttle (34, 42-44). In the *E. coli* QFR co-structure with fumarate, a water molecule mediates the interaction between Arg-A287 and fumarate (Fig. 27). Bound water molecules often act as proton shuttles in enzymes, but no on-pathway water molecule has been proposed as a proton donor in QFR or other complex II homologs. While our crystal structure leaves open the possibility of water-mediated proton transfer in the *E. coli* enzyme, the location of this water molecule may suggest how complex II homologs perform off-pathway catalysis.

Off-pathway catalysis 1: oxaloacetate formation via enzymatic fumarate hydration to malate– Oxaloacetate is a tight-binding inhibitor of QFR (3) and its formation might

be catalytically induced upon fumarate hydration to malate followed by oxidation to oxaloacetate (4). In the structure of oxaloacetate bound to *E. coli* QFR (Fig. 5B), the oxaloacetate carbonyl is oriented parallel to the N5-C(5a) FAD similar to that observed in the oxaloacetate co-structure with avian complex II (PDBID 1YQ4; (13)) and the malate-like intermediate co-structure with a soluble fumarate reductase from *Shewenella frigidimarina* (PDBID 1QJD; (33)).
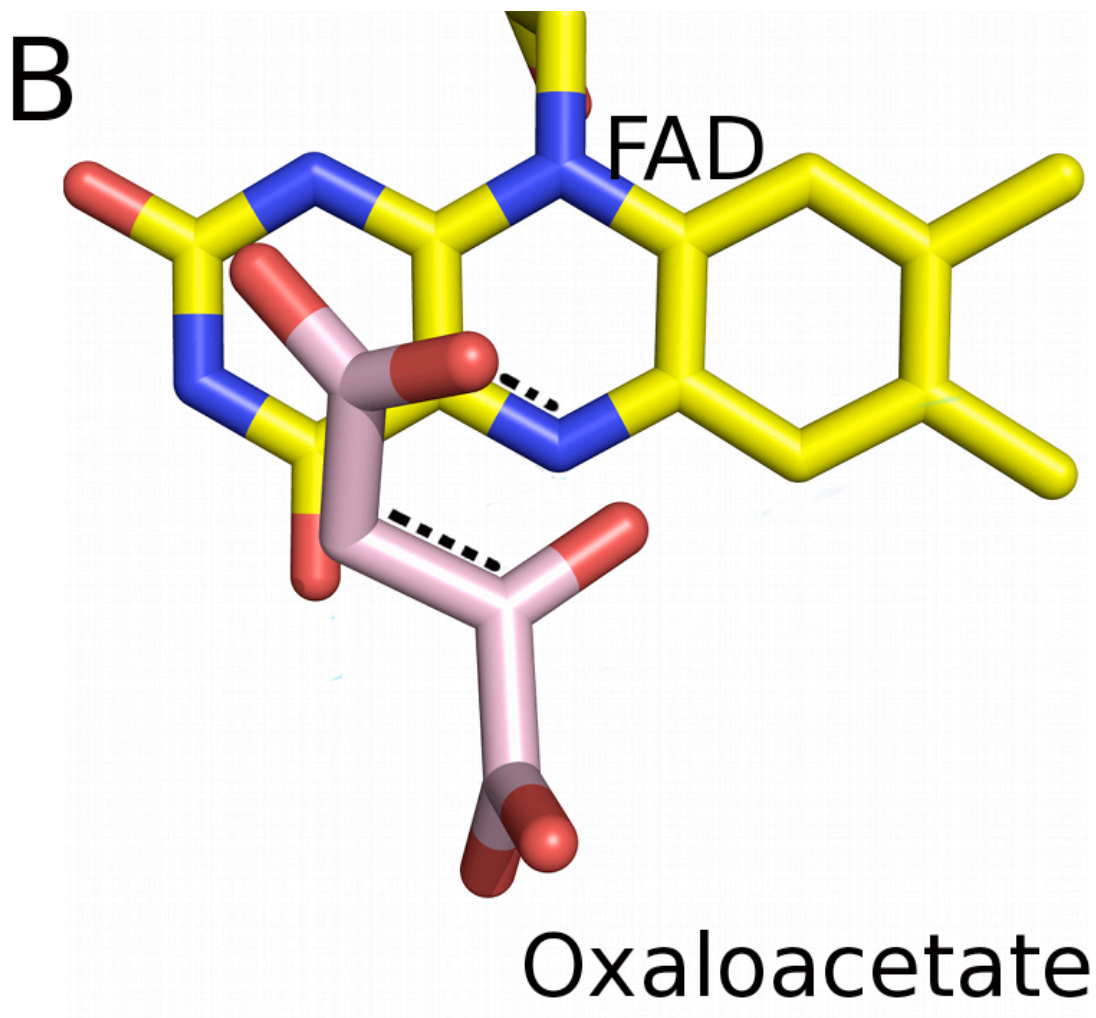
Figure 37. The *E. coli* QFR co-crystallized with oxaloacetate. Carbon atoms of the oxaloacetate are colored *magenta*. In all the figures, nitrogen is colored *blue*, oxygen is colored *red*, FAD carbons are colored *yellow*, and sulfur is colored *tan.*

The planar orientation of oxaloacetate relative to FAD resembles that of fumarate, especially in relation to the similar positioning of the C2-C3 bond in fumarate and oxaloacetate (Fig. 34 and 36). Importantly, spectroscopic characterization in avian complex II has shown that fumarate can undergo a simple hydration reaction along the C2-C3 double bond to yield malate (5). This is

corroborated by previous attempts to crystallize QFR homologs with fumarate, which have yielded active site density more consistent with oxaloacetate or malate than fumarate (33).

Intriguingly, only the electron density within the active site of structures of *Shewanella frigidimarina* fumarate reductase (PDBID 1QJD; (33)) and avian complex II (PDBID 2H88; (5)) co-crystallized with fumarate at pH 7.2 or greater were consistent with the malate-like intermediate. Conversely, both the *E. coli* QFR and *W. succinogenes* QFR (PDBID 1QLB; (31) were co-crystallized with fumarate at lower pH, and the electron density is consistent with a bound fumarate and a water molecule. This may reflect two separate catalytic states in the complex II homologs. Under high pH conditions, the proton shuttle may be ionized and the active site is shifted into a state that allows for water addition, while lower pH leads to a deionized proton shuttle, trapping the water molecule near substrate. While speculative, the water molecule bound between fumarate and Arg-A287 in the *E. coli* QFR (Fig. 2A) may identify the location of this attacking group during off-pathway malate formation from fumarate. When present, malate can be transformed to oxaloacetate via hydride transfer from FAD (4). The orientation of oxaloacetate lends support to a model where malate is first oriented correctly along the FAD ring and then activated for catalysis in a manner analogous to fumarate activation. It is easy to speculate a physiological role for this off-pathway catalysis, since the formation of a tightly binding inhibitor could regulate the activity of QFR and other complex II homologs.

The higher apparent affinity of oxaloacetate compared to fumarate may potentially be rationalized by interactions with the FAD ring. The expected HOMO-

LUMO overlap of the π-bonding orbital from the C2-C3=O conjugate of the enol form of oxaloacetate and the LUMO of oxidized FAD could underlie the formation of the charge-transfer interaction (Fig. 5E) reflected in the band centered at 550 nm in the optical spectrum (Fig. 3) (3). This HOMO-LUMO overlap is somewhat analogous to the overlap of the C2-C3 double bond of fumarate with the FAD LUMO, except that the oxaloacetate carbonyl may also contribute to the formation of the conjugated-π system since the almost planar alignment of the C2-C3-O5 atoms of oxaloacetate likely aligns the atomic p_z orbitals of these atoms with those of the isoalloxazine ring (Fig. 5E). A similar delocalized π-conjugated system has been proposed to underlie charge transfer formation during the binding of acetoacetyl-coA in acyl-coA dehydrogenase (45). The Glide calculations do not include a term corresponding to the formation of a conjugated system. That computational modeling only failed to account for binding affinity of oxaloacetate supports a conjugated-π interaction contributing to the affinity of oxaloacetate binding.

Off-pathway catalysis 2: suicide inhibition via covalent adduct formation with 3-NP– X-ray crystallography and mass spectral analysis suggest that 3-NP addition to QFR results in the formation of a 2,3,5-triazole adduct to the likely proton shuttle Arg-A287. The formation of a 2,3,5-triazole raises a number of chemical challenges, including addition to an unreactive carbon atom and reduction of the nitro functional group. The ^{15}N labeled 3-NP experiment (Fig. 32) confirms the presence of nitrogen from 3-NP in the adduct, ruling out loss of the nitro group through elimination, which is a common reaction for activated nitroalkanes. Instead, we considered pathways involving both an overall oxidation of 3-NP and a localized formal reduction and

dehydration of nitrogen. It has previously been demonstrated that that the dehydrogenation product of 3-NP, 3-nitroacrylate, shows faster inhibition kinetics than 3-NP, which suggests that 3-NP is converted to 3-nitroacrylate prior to forming a covalent adduct (12). The most parsimonious mechanism of conversion of 3-NP to 3-nitroacrylate is by the complex II enzyme itself. In a co-crystal structure of 3-NP with porcine complex II, a non-covalent binding mode for 3-NP was identified within the enzyme active site (14). Dehydrogenation of 3-NP to 3-nitroacrylate, a reaction analogous to succinate oxidation to fumarate, can be inferred by the observation that FAD oxidizes upon 3-NP addition (Fig. 31). Furthermore, FAD oxidation exactly matches QFR inactivation, suggesting that 3-nitroacrylate is the active chemical species in adduct formation.

The 3-nitroacrylate intermediate would be expected to be a powerful electrophile that engages arginine in an addition reaction. Furthermore, an induced dipole formed by interactions with the polar active site, along with geometric torsion, may further activate 3-nitroacrylate for addition by arginine in a manner similar to fumarate activation. Optical changes in FAD similar to those seen with fumarate binding are observed upon 3-NP binding, suggesting that nonadducted 3-nitropropionate and 3-nitroacrylate likely produce the same fumarate C2-C3 bond overlap over the FAD C(4a)-N5 to further activate the unreactive C2 atom adjacent to the nitro group. Upon arginine addition, nitro reduction to nitroso releases a molecule of water.
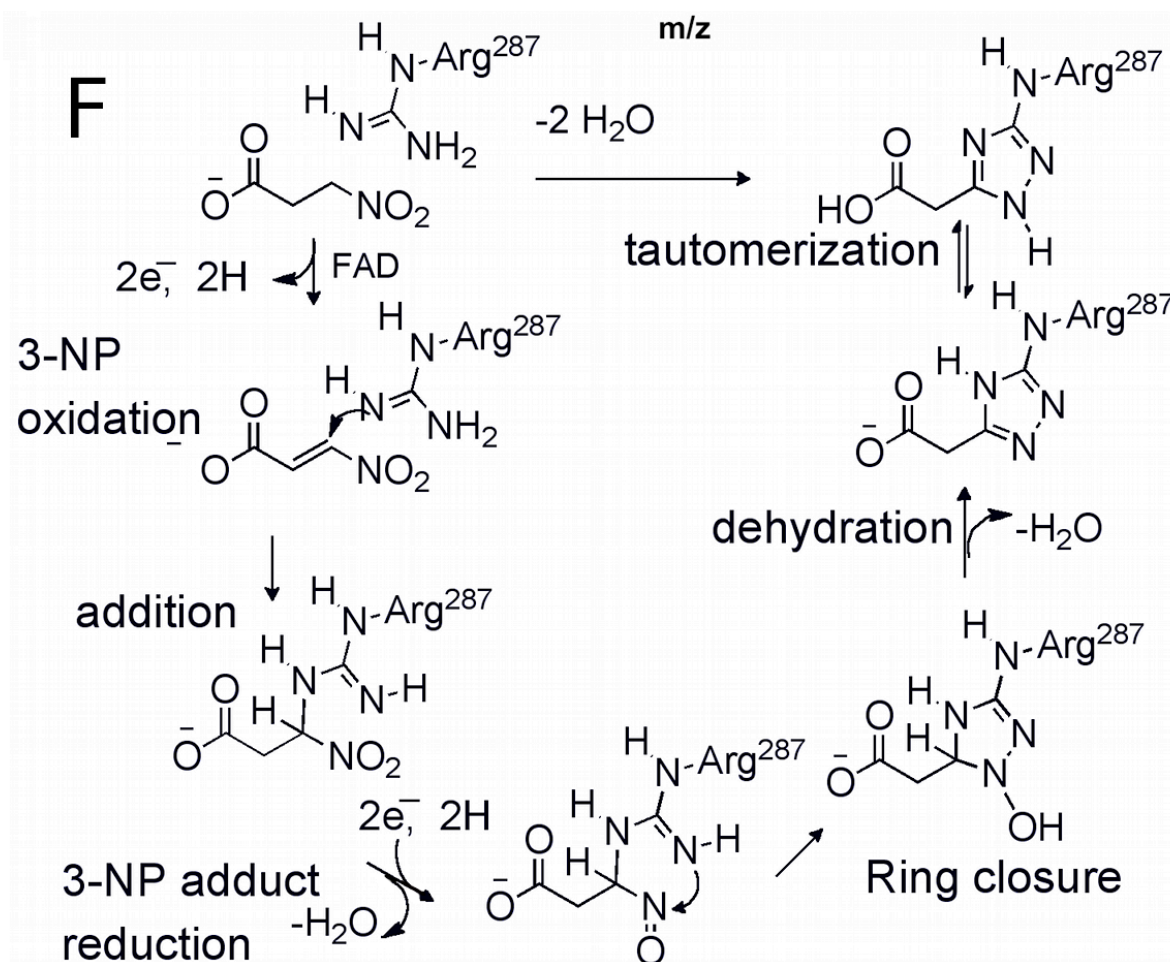
Figure 38. Possible minimal mechanism for formation of the covalent adduct between 3-NP and Arg-A287.

The reactive intermediate prior to nitroso formation could not be characterized; however, it is possible that formation of nitronic acid by resonance from a carbanion could facilitate nitro reduction. Nitroso formation provides an opportunity for N-N bond formation by addition of the arginine nitrogen to the electrophilic nitroso nitrogen. A final dehydration and tautomerization would then provide the observed triazole (Fig. 38).

In cases where nitroalkanes are converted to amide derivatives, the nitroalkane is first transformed to the corresponding ketone or carboxylic acid, resulting in cleavage of the carbon-nitro bond. A very recent exception to this is the reaction of an α-bromo nitroalkane with an electrophilic amine (a halamine, RNHI) (46). However, the carbon-nitro bond is cleaved during this transformation as well. The nitroalkane derivatization to a triazole without carbon-nitro bond cleavage suggests an unprecedented mechanism in the context of known nitroalkane chemistry. A mechanistic hypothesis is advanced (Fig. 38) that is consistent with the experiments described above.

Molecular basis for competitive inhibition– The alignment of an activatable bond along the C(4a)-N5 bond of the FAD, as is reflected in the optical difference spectra, is a clear requirement for either on- or off-pathway catalysis. This suggests that dicarboxylates that do not cause differences in the optical spectrum, such as glutarate and citrate, do not align similarly. This is indeed what is supported by our data. Glutarate does not show an electronic interaction with FAD, but binds within the *E. coli* QFR active site with torsioned carboxylates and at the same location as fumarate (Fig. 2D). However, the increased length and flexibility of glutarate results in a binding mode where the alkane chain buckles outward and does not orient any bond along the C(4a)-N5 bond of FAD. A similar effect is noticed in the published QFR co-structure with citrate (17), where citrate lacks a bond aligned to the FAD ring (Fig. 39).

Additionally, both glutarate and citrate are predicted to have less favorable steric interactions, making them bind less tightly than other QFR ligands (Table 6). That neither glutarate nor citrate show an electronic interaction with FAD in optical spectra (Fig. 30) is consistent with our hypothesis that alignment of an activatable bond parallel to the C(4a)-N5 bond of FAD underlies this spectral change, and offers a possible explanation for the lack of catalytic turnover of glutarate or citrate. This model is consistent with QFR using orbital steering mechanism where geometric constraints of the ligand dictate correct orbital overlap.

Conclusions

The geometric and electronic activation of ligands may be a key factor in determining ligand activation and behavior in flavoenzymes. This geometric activation controls reactivity in QFR, and predicts that potential substrates for QFR and FAD-containing enzymes that catalyze a,b-dehydrogenation reactions may be identified by examination of optical difference spectra, which undergo changes upon orbital interaction with precisely-oriented ligands.

References

1.   Cecchini, G. (2003) *Annu. Rev. Biochem.* **72**, 77-109

2.   Ackrell, B. A. C., Kearney, E. B., and Mayr, M. (1974) *J. Biol. Chem.* **249**, 2021-2027

3. Ackrell, B. A. C., Cochran, B., and Cecchini, G. (1989) *Arch. Biochem. Biophys.* **268**, 26-34

4. Belikova, Y. O., Kotlyar, A. B., and Vinogradov, A. D. (1988) *Biochim. Biophys. Acta* **936**, 1-9

5. Huang, L. S., Shen, J. T., Wang, A. C., and Berry, E. A. (2006) *Biochim. Biophys. Acta.* **1757**, 1073-1083

6. Kölker, S., Koeller, D. M., Sauer, S., Hörster, F., Schwab, M. A., Hoffmann, G. F., Ullrich, K., and Okun, J. G. (2004) *J. Inherit. Metab. Dis.* **27**, 805-812

7. Ullrich, K., Flott-Rahmel, B., Schluff, P., Musshoff, U., Das, A., Lucke, T., Steinfeld, R., Christensen, E., Jakobs, C., Ludolph, A., Neu, A., and Röper, R. (1999) *J. Inherit. Metab. Dis.* **22**(4), 392-403

8. Alston, T. A., Mela, L., and Bright, H. J. (1977) *Proc. Natl. Acad. Sci. U.S.A* **74**, 3767-3771

9. Bush, M. T., Touster, O., and Brockman, J. E (1951) *J. Biol. Chem.* **188**, 685-693

10. Morris, M. P., Pagán, and Warmke, H. E. (1954) *Science* **119**, 322-323

11. Beal, M. F., Brouillet, E., Jenkins, B. G., Ferrante, R. J., Kowall, N. W., Miller, J. M., Storey, E., Srivastava, R., Rosen, B. R., and Hyman, B. T. (1993) *J. Neurosci.* **13**, 4181-4192

12. Coles, C. J., Edmondson, D. E., and Singer, T. P. (1979) *J. Biol. Chem.* **254**, 5161-5167

13. Huang, L. S., Sun, G., Cobessi, D., Wang, A. C., Shen, J. T., Tung, E. Y., Anderson, V. E., and Berry, E. A. (2006) *J. Biol. Chem.* **281**, 5965-5972

14.   Sun, F., Huo, X., Zhai, Y. J., Wang, A. J., Xu, J. X., Su, D., Bartlam, M., and Rao, Z. H. (2005) *Cell* **121**, 1043-1057

15.   Luna-Chávez, C., Iverson, T. M., Rees, D. C., and Cecchini, G. (2000). *Protein Expression Purif.* **19** 188-196

16.   Maklashina, E., Hellwig, P., Rothery, R. A., Kotlyar, V., Sher, Y., Weiner, J. H., and Cecchini, G. (2006) *J. Biol. Chem.* **281**, 26655-26664

17.   Maklashina, E., Iverson, T. M., Sher, Y., Kotlyar, V., Andrell, J., Mirza, O., Hudson, J. M., Armstrong, F. A., Rothery, R. A., Weiner, J. H., and Cecchini, G. (2006) *J. Biol. Chem.* **281**, 11357-11365

18.   Yates, J. R., Eng, J. K., McCormack, A. L., and Schieltz, D. (1995) *Anal. Chem.* **67**, 1426-1436

19.   Iverson, T. M., Luna-Chavez, C., Cecchini, G., and Rees, D. C. (1999) *Science* **284**, 1961-1966

20.   Otwinowski, Z. (1993) *In CCP4 Study Weekend Data Collection and Processing;* (Sawyer, L., Isaacs, N., and Bailey S., eds) pp. 56 – 62, *SERC Daresbury Labortatory, United Kingdom*

21.   Otwinowski, Z., and Minor, W. (1997) Processing of X-ray diffraction data collected in oscillation mode. In *Meth. Enz. Macromolecular Crystallography*, *Pt A,* (C.W. Carter, Jr. & R. M. Sweet) Academic Press Inc, San Diego

22.   Bailey, S. (1994) *Acta Crystallographica Section D-Biological Crystallography* **50**, 760-763

23.   Brunger, A. T., Adams, P. D., Clore, G. M., DeLano, W. L., Gros, P., Grosse-Kunstleve, R. W., Jiang, J. S., Kuszewski, J., Nilges, M., Pannu, N. S., Read,

R. J., Rice, L. M., Simonson, T., and Warren, G. L. (1998) *Acta Crystallogr. Sect.* **D54**, 905-921

24.   Iverson, T. M., Luna-Chávez, C., Croal, L. R., Cecchini, G., and Rees, D. C. (2002) *J. Biol. Chem.* **277**, 16124-16130

25.   Jones, T. A., Zou, J. Y., Cowan, S. W., and Kjeldgaard, M. (1991) *Acta Crystallogr. Sect.* **A47**, 110-119

26.   Emsley P. and Cowtan, K. (2004) *Acta Crystallogr. Sect.* **D60**, 2126-2132

27.   Murshudov, G. N., Vagin, A. A., and Dodson, E. J. (1997) *Acta Crystallogr. Sect.* **D53**, 240-255

28.   Painter, J., and Merritt, E. A. (2006) *Acta Crystallogr. Sect.* **D62**, 439-450

29.   Painter, J., and Merritt, E. A. (2006) *J. App. Crystallogr.* **39**, 109-111

30.   Friesner, R. A., Murphy, R. B., Repasky, M. P., Frye, L. L., Greenwood, J. R., Halgren, T. A., Sanschagrin, P. C., and Mainz, D. T. (2006) *J. Med. Chem.* **49**, 6177-6196

31.   Lancaster, C. R. D., Kroger, A., Auer, M., and Michel, H. (1999) *Nature* **402**, 377-385

32.   Leys, D., Tsapin, A. S., Nealson, K. H., Meyer, T. E., Cusanovich, M. A., and Van Beeumen, J. J. (1999) *Nat. Struct. Biol.* **6**, 1113-1117

33.   Taylor, P., Pealing, S. L., Reid, G. A., Chapman, S. K., and Walkinshaw, M. D. (1999) *Nat. Struct. Biol.* **6**, 1108-1112

34.   Reid, G. A., Miles, C. S., Moysey, R. K., Pankhurst, K. L., and Chapman, S. K. (2000) *Biochim. Biophys. Acta* **1459**, 310-315

35. Tomasiak, T. M., Maklashina, E., Cecchini, G., and Iverson, T. M. (2008) *J. Biol. Chem.* **283**, 15460-15468

36. Kim, J. J. P., Wang, M., and Paschke, R. (1993) *Proc. Natl. Acad. Sci. U. S. A.* **90**, 7523-7527

37. Umhau, S., Pollegioni, L., Molla, G., Diederichs, K., Welte, W., Pilone, M. S., and Ghisla, S. (2000) *Proc. Natl. Acad. Sci. U. S. A.* **97**, 12463-12468

38. Hall, L. H., Bowers, M. L., and Durfor, C. N. (1987) *Biochemistry* **26**, 7401-7409

39. Nishina, Y., Sato, K., Miura, R., and Shiga, K. (1995) *J. Biochem.* **118**, 614-620

40. Dafforn, A., and Koshland, D. E. (1971) *Proc. Natl. Acad. Sci. U.S.A* **68**, 2463-2467

41. Mesecar, A. D., Stoddard, B. L., and Koshland, D. E. (1997) *Science* **277**, 202-206

42. Doherty, M. K., Pealing, S. L., Miles, C. S., Moysey, R., Taylor, P., Walkinshaw, M. D., Reid, G. A., and Chapman, S. K. (2000) *Biochem.* **39**, 10695-10701

43. Mowat, C. G., Moysey, R., Miles, C. S., Leys, D., Doherty, M. K., Taylor, P., Walkinshaw, M. D., Reid, G. A., and Chapman, S. K. (2001) *Biochem.* **40**, 12292-12298

44. Pankhurst, K. L., Mowat, C. G., Rothery, E. L., Hudson, J. M., Jones, A. K., Miles, C. S., Walkinshaw, M. D., Armstrong, F. A., Reid, G. A., and Chapman, S. K. (2006) *J. Biol. Chem.* **281**, 20589-20597

45.   Miura, R., Nishina, Y., Fujii, S., and Shiga, K. (1996) *J. Biochem.* **119**, 512-519

46.   Shen, B., Makley, D. M., and Johnston, J. N. (2010) *Nature* **465**, 1027-1032

Acknowledgements

CHAPTER IV

PRELIMINARY STRUCTURAL INVESTIGATION OF A MENAQUINOL:FUMARATE REDUCTASE MUTANT THAT STABILIZES A SEMIQUINONE RADICAL INTERMEDIATE

Abstract

In *Escherichia coli* menaquinol:fumarate reductase (QFR) catalyzes conversion of menaquinol to menaquinone to support anaerobic respiration with fumarate as the terminal electron acceptor. QFR can also catalyze ubiquinone reduction to support aerobic respiration when expressed under aerobic conditions. In order to study the details of the menaquinone reaction and of ubiquinone binding, the co-structures of menaquinone and ubiquinone were determined with a mutant variant of QFR, FrdC E29L, which stabilizes the semiquinone intermediate of menaquinone. The co-structures of substrate analogs heptyl-quinoline N-oxide (HQNO) and atpenin A5 were also determined with the FrdC E29L variant of QFR. A comparison of the menaquinone binding sites and HQNO reveal a possible rearrangement with menaquinone binding with menaquinone shifting away from the position of the E29L mutation. The ubiquinone co-structure and the atpenin A5 co-structure reveals electron density in new binding pocket termed Q_M. Although the physiological relevance of this site awaits verification, a series of ionizable residues lining the cavity may provide a possible proton pathway.

Introduction

Menaquinol:fumarate reductase (QFR) catalyzes the concomitant interconversion of fumarate to succinate and menaquinol to menaquinone. QFR couples the two reactions to catalyze the exchange of electrons between two distinct environments: the water-soluble environment of the cytoplasm and the lipid soluble environment of the plasma membrane (1). Fumarate reduction takes place at the soluble flavoprotein subunit frdA. Menaquinol interconversion takes place in the membrane area at the intersection of three domains: the iron protein subunit (frdB in QFR) and two integral membrane subunits (frdC and frdD in QFR). Along with menaquinol oxidation, QFR can also support ubiquinol reduction (2) when genetically manipulated for expression during aerobic conditions, functionally replacing the activity of succinate:ubiquinone oxidoreductase (SQR).

Structural analysis of QFR has revealed that menaquinol binds in two distinct pockets termed the Q_P and Q_D sites (3). The Q_P and Q_D sites are ~27Å away from each other, too far for efficient electron transfer, leaving unclear any significant biological role for the Q_D site. An unidentified region of electron density was observed between the Q_P and Q_D sites, dubbed the Q_M site, although its activity and physiological relevance remain unknown (4). Numerous lines of evidence support the Q_P site as the site of menaquinol oxidation. EPR experiments support that the Q_P site is located proximally to the [3Fe:4S] cluster on the iron protein subunit (5), and it is proposed that electron transfer occurs directly from menaquinol bound at Q_P

and the [3Fe:4S] cluster. Numerous amino acids stabilize menaquinol in the Q_P site, including Lys-B228, Arg-C28, Glu-C29, and Trp-D114.

Identification and verification of quinone binding and active sites has been greatly facilitated with the use of site-specific inhibitors (Fig. 39). In general, two classes of QFR and SQR quinone site inhibitors are available: the ubiquinone site-specific inhibitors atpenin A5 (6,7), carboxin, and 2-thenoyltrifluoroacetone TTFA and the nonspecific (i.e. ubiquinone and menaquinone) active site inhibitors such as heptyl-quinoline n-oxide (HQNO).
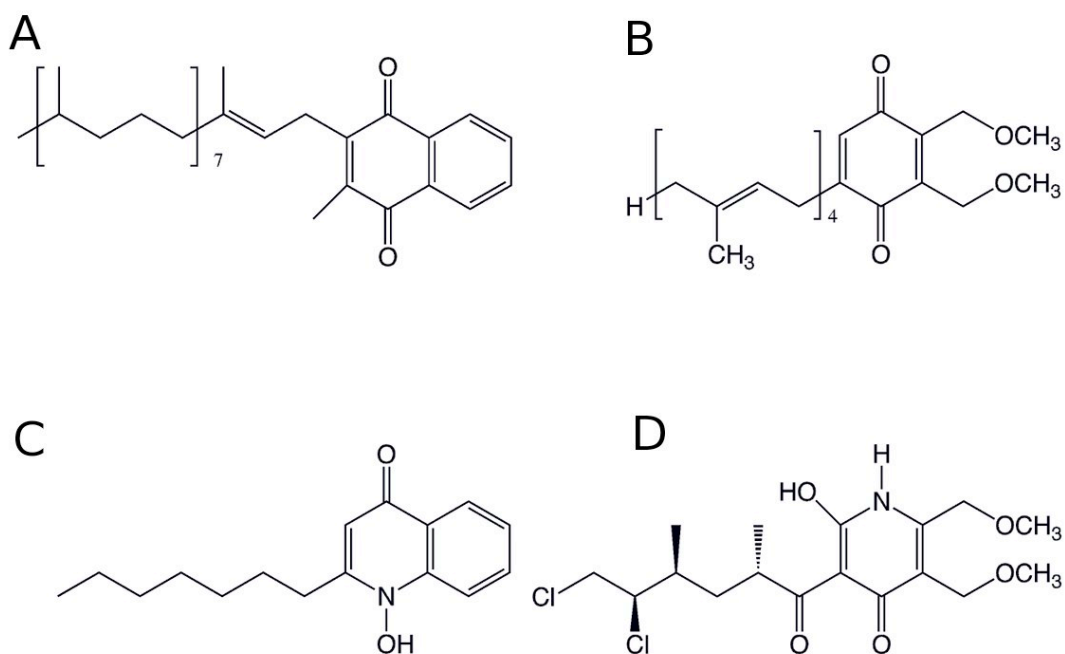

Figure 39. Quinol site ligands. A. Menaquinol B. Ubiquinone (UQ-4) C. Heptyl quinoline N-oxide D. Atpenin A5

Crystallographic studies of the menaquinone site show that HQNO binds in the Q_P site (4), consistent with EPR data showing a close interaction between [Fe3:4S] and HQNO upon binding and spin-relaxation enhancement (8). Crystal structures of SQR bound with AA5 and TTFA find a binding site proximal to the [3Fe:4S] site, analogous to Q_P in QFR but with no sequence identity (7). Although no crystallographic ubiquinone has been found bound to SQR, the location of these inhibitors is consistent with mutagenesis and EPR showing that the site next to the [3Fe:4S] is the likely ubiquinone reduction site (9).

Mutagenesis and EPR experiments have revealed that menaquinol to menaquinone interconversion takes place with formation of a stabilized semiquinone radical intermediate (5). Mutagenesis of Glu-C29 to leucine significantly raises the pKa of menaquinol oxidation, suggesting that Glu-C29 acts as the likely proton acceptor in the first step of the semiquinone formation. The E29L mutation has also been shown to stabilize the life-time of the semiquinone radical intermediate by 100 fold with EPR. In studies of the E29L mutations and menaquinone, a signal was detected at g = 2.04, consistent with the formation of an anionic semiquinone intermediate similar to that observed in bovine complex II. This proposed semiquinone signal was likely at the Q_P site due to a spin-relaxation enhancement from the [3Fe:4S] cluster (5).

QFR can also support ubiquinone oxidation *in vitro* to support aerobic succinate oxidation, though *in vivo* it is not expressed under aerobic conditions (2). Although QFR can catalyze ubiquinone oxidation *in vitro*, a binding site or mechanism has not been identified for ubiquinone binding. The E29L mutation did

not show a decrease in ubiquinone reduction, suggesting either a separate binding interaction at the Q_P site or a separate binding position (5).

To study the effects of the QFR E29L mutation on the structure of the Q_P active site and on the binding of menaquinone, ubiquinone-4 (UQ-4), and inhibitors, we structurally characterized the binding of these ligands with QFR E29L as well as wild-type QFR with atpenin A5 as a comparison. The mechanistic implications for semimenaquinone stabilization and ubiquinone binding and catalysis are explored.

Materials and Methods

QFR purification –The FrdC E29L variant of the *E. coli* QFR was produced in *E. coli* strain DW35 (*ΔfrdABCD, sdhC::kan*) cells containing the pH3 plasmid grown under microaerophilic conditions in Terrific Broth medium as previously described. Isolated membranes, obtained as described in (10), were suspended in a solution of 20 mM Tris, 0.1 mM EDTA (pH 7.4) followed by solubilization with $C_{12}E_9$ detergent (Anatrace) to a final concentration of 2%. Purification of QFR was performed using a three-step chromatography protocol beginning with Q-sepharose anion exchange (GE Healthcare), then with POROS anion exchange (Applied Biosystems), followed by size exclusion chromatography on a superdex S-200 column (GE Healthcare) as described previously (10). Slight modifications were made to the protocol to account for the increased instability of the E29L mutant, namely that the second anion exchange step was lengthened from an elution gradient of 7 column volumes to 14 column volumes.   Protein concentration was measured by the bicinchoninic acid

method (Pierce) with bovine serum albumin as standard in the presence of 0.05% (w/v) $C_{12}E_9$ detergent.

Crystallization of the E29L mutant QFR with inhibitors- E29L QFR and menaquinone co-crystals were grown in polyethylene glycol 5000, mM magnesium acetate, 100 mM citric acid pH 5.8, 0.1% DTT, 0.1mM EDTA at room temperature. The E29L QFR and atpenin A5 co-crystals were grown in 13.5% polyethylene glycol (PEG) 5000 mono-methyl ether (MME), 80 mM magnesium acetate, 100 mM citric acid pH 5.8, 0.1% DTT, and 0.1 mM EDTA at room temperature, and 360 nM Atpenin A5. Wt QFR and atpenin A5 co-crystals were grown in 13% polyethylene glycol 8000, 25 mM magnesium acetate, 100 mM citric acid pH 5.8, 0.1% DTT, 0.1 mM EDTA, and 120 nM of atpenin A5 at 22°C. E29L QFR and UQ-4 co-crystals were grown with QFR co-purified with 25 μM of UQ-4 in 16.5% polyethylene glycol 8000, 40 mM magnesium acetate, 100 mM citric acid pH 5.8, 0.1% DTT, 0.1 mM EDTA. E29L QFR and HQNO co-crystals were grown with QFR co-purified with 10 mM of HQNO in 13.5% polyethylene glycol 5000 monomethyl ether, 100 mM magnesium acetate, 100 mM citric acid pH 5.8, 0.1% DTT, 0.1 mM EDTA.

Crystals were grown using the hanging drop vapor diffusion method. QFR crystals formed in the orthorhombic space group $P2_12_12_1$ with unit cell dimensions shown in Table 6. Data collection statistics are shown in Table 6

.

Table 7: Data collection and refinement statistics for crystal structures of QFR

	E29L MQ	E29L AA5	WT AA5	E29L HQNO	E29L UQ-4
Wavelength	1.0 Å	1.1 Å	1.1 Å	1.2 Å	1.0 Å
Beamline	SSRL 9-2	APS ID-21	SSRL 9-2	APS ID-21	SSRL 9-2
Resolution	3.3 Å	3.40 Å	3.10 Å	3.35 Å	3.1 Å
Completeness	80.2% (73.8%)	92.4% (81.2%)	81.1% (72.1%)	90.0% (84.1%)	92.7% (63.0%)
I/s	12.8 (2.3)	10.1 (2.5)	10.7 (1.9)	16.1 (4.9)	12.4 (2.0)
$R_{sym}{}^a$	0.097 (0.392)	0.096 (0.333)	0.153 (0.515)	0.100 (0.272)	0.098 (0.389)
Refinement					
$R_{cryst}{}^b$	0.240	0.224	--	0.228	0.240
R_{free}	0.305	0.262	--	0.280	0.281
RMSD bonds	0.023	0.026	--	0.025	0.034
RMSD angles	2.304	2.393	--	2.602	2.831

Values in parenthesis indicate statistics for the highest shell.

A: R_{sym} = S $|I_i - <I>|/SI_i$ where I is intensity, "I" is the ith measurement, and <I> is the weighted mean of I.

b: R_{cryst} = S $||F_{obs}| - |F_{calc}||/SF_{pbs}$. R_{free} is the same as R_{cryst} for a set of data omitted from the refinement.

Data collection and processing – Data reduction was performed using the programs DENZO (11), SCALEPACK, HKL2000 (12), and the CCP4 suite of programs. Since crystals were isomorphous with crystals from known structures of QFR (13), rigid body refinement was performed with refmac to obtain an initial model and initial phases (14). Wild-type QFR with oxaloacetate bound (later deposited as PDBID: 3PQR) was used as a starting model for QFR co-complexed with MQ. The already published structure 1KF6 (4) was used for the HQNO, UQ-4, and atpenin-A5 co-structures with FrdC E29L QFR. Model rebuilding was performed in the molecular graphics program COOT (15) while refinement and map calculations were performed with Refmac5 in CCP4 and Phenix (16). Molecular representations used were created in the program PyMOL (17).

Results

The FrdC E29L variant of QFR was co-crystallized with substrates menaquinone, ubiquinone and inhibitors HQNO, and atpenin A5. Preliminary electron density allowed for tentative assignment of ligand binding in each co-crystal structure and compared to wild-type QFR co-structures.

Alterations and rearrangements of menaquinone in the FrdC E29L QFR Q_P site – The QFR co-structure with co-purified menaquinone bound showed clear density for a menaquinone molecule only at the Q_P site, and was absent at Q_D (Fig. 40).
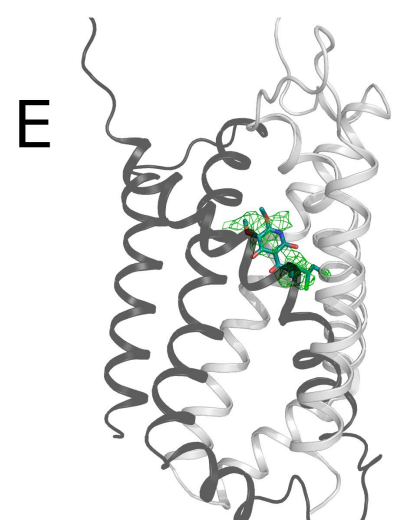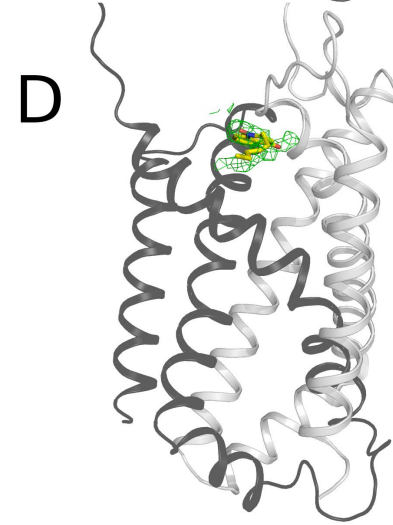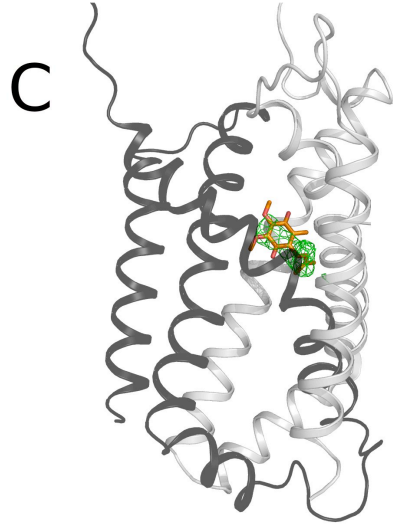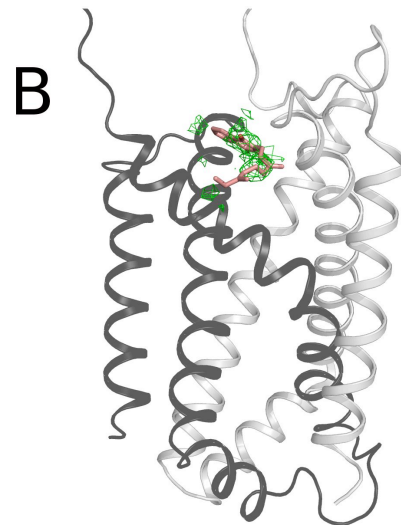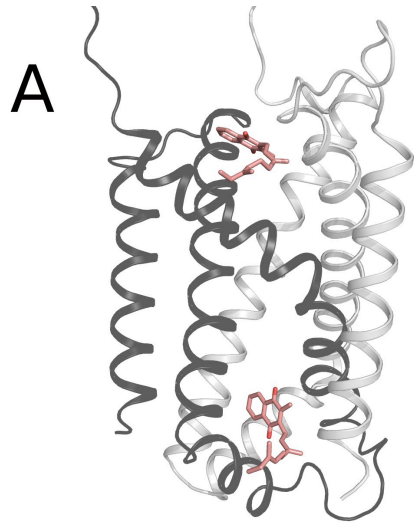
Figure 40. Comparison of electron density of QFR-ligand complexes. The C subunit is colored grey and the D subunit colored black. Oxygen atoms are colored red, nitrogen atoms are colored blue, and carbon atoms are colored salmon for menaquinone, orange for ubiquinone, yellow for HQNO, and teal for atpenin A5. Electron density is countered as a green mesh at 2σ for all structures except for menaquinol, where it is contoured at 1.5σ. A. The published structure of wild-type QFR with menaquinol (PDBID:1LOV; (3)) B. The co-structure of frdC E29L QFR with menaquinol in the Q_P active site. B. The co-structure of frdC E29L QFR with ubiquinol modeled in the Q_M site. B. The frdC E29L QFR co-struc ture with HQNO modeled in the Q_P active site. B. The co-structure of frdC E29L QFR with atpenin A5 modeled in the Q_M site.

In the Q_P site, menaquinone makes multiple putative hydrogen bonding contacts, including from O4 of the menaquinone to Nε1 of Trp-D14 and to of Nζ of Lys-B228 (Fig. 41).
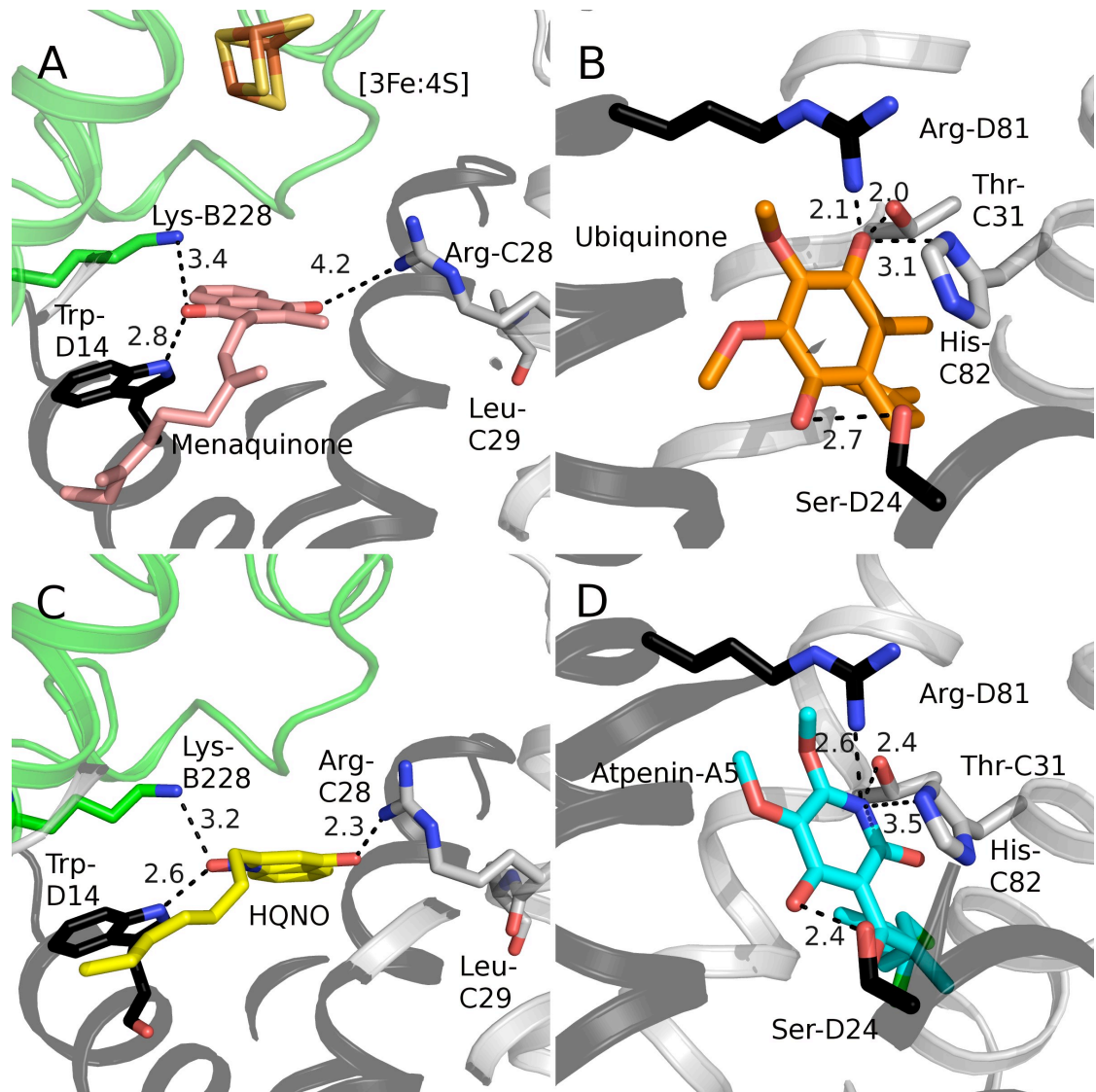
Figure 41. Ligand binding in the E29L QFR co-structures. The C subunit is colored grey and the D subunit colored black. Oxygen atoms are colored red, nitrogen atoms are colored blue, and carbon atoms are colored salmon for menaquinone, orange for ubiquinone, yellow for HQNO, teal for atpenin A5, and either grey or black for side chains depending on which subunit they are from. Dashes represent distances between atoms in angstroms. A. Menaquinol bound in the Q_P site. B. Ubiquinone (UQ-4) bound in the Q_M site. C. HQNO bound in the Q_P site. D. Atpenin-A5 bound in the Q_M site.
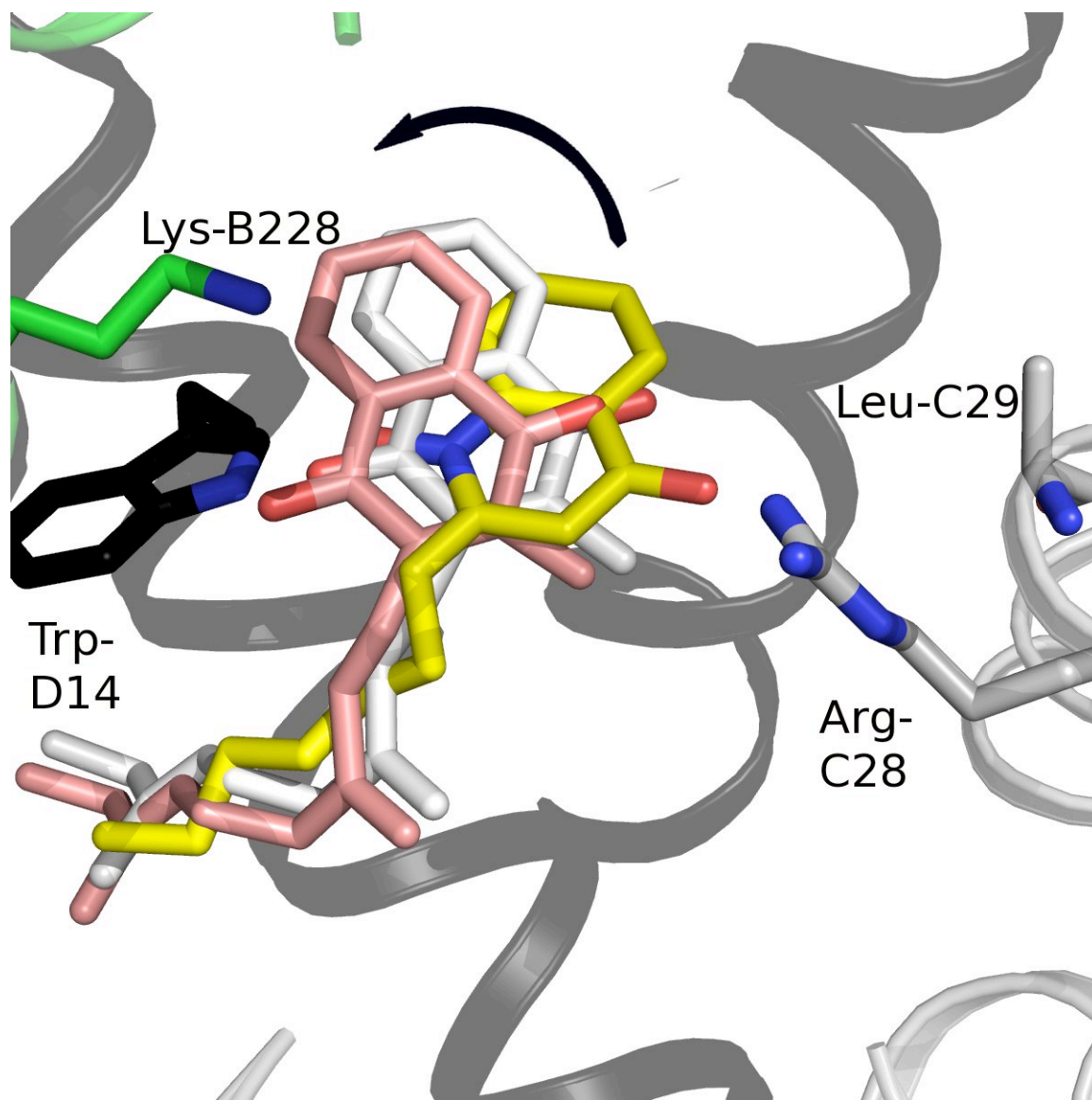
Figure 42. Superimposition of the altered position of menaquinol binding in E29L binding compared to menaquinol bound to wild-type QFR and HQNO bound to wild-type QFR. The B subunit is colored green, C subunit is colored grey and the D subunit colored black. Oxygen atoms are colored red, nitrogen atoms are colored blue, and carbon atoms are colored salmon for menaquinone bound to E29L QFR, yellow for HQNO bound to wild-type, and white for menaquinol bound to wild-type QFR. The side chains are colored either grey or black for side chains depending on which subunit they correspond to.

Menaquinone exhibits a shifted position in the active site, shifting 1.1 Å away from its position in wt QFR when measured at the distal part of the ring (Fig. 42).

A 1.0 Å shift is exhibited at the O1 oxygen, away from the Ala-C29. The shift is towards Lys-B228, and away from Ala-C29; however, this change does not significantly alter the distance to the [3Fe:4S] iron sulfur cluster compared to the MQ position in wild-type. The shift is consistent with a model proposed where menaquinol binds, and then swings around an axis while maintaining hydrogen bonds with Trp-D14 and Lys-B228.

Possible identification of the ubiquinone binding site – The structure of E29L QFR co-complexed with UQ-4 exhibited strong density in a pocket located near the center of the membrane in the integral membrane subunits (Fig. 40C). This observation is consistent with the presence of previously unidentified electrons density observed in co-structures of HQNO with wild-type QFR. The binding pocket is made by the intersection of two helices each from subunit C and subunit D. Further experiments have to be performed to identify this as a true ubiquinone binding site. A cautious interpretation of the electron density allowed for the preliminary modeling of UQ-4 into the active site. UQ-4 was tentatively modeled in the density, and exhibits a distance of 8.6 Å from the Q_P site and 14.5 Å from the Q_D site, both within the expected 15Å limit for biologically relevant electron transfer (Fig. 43).
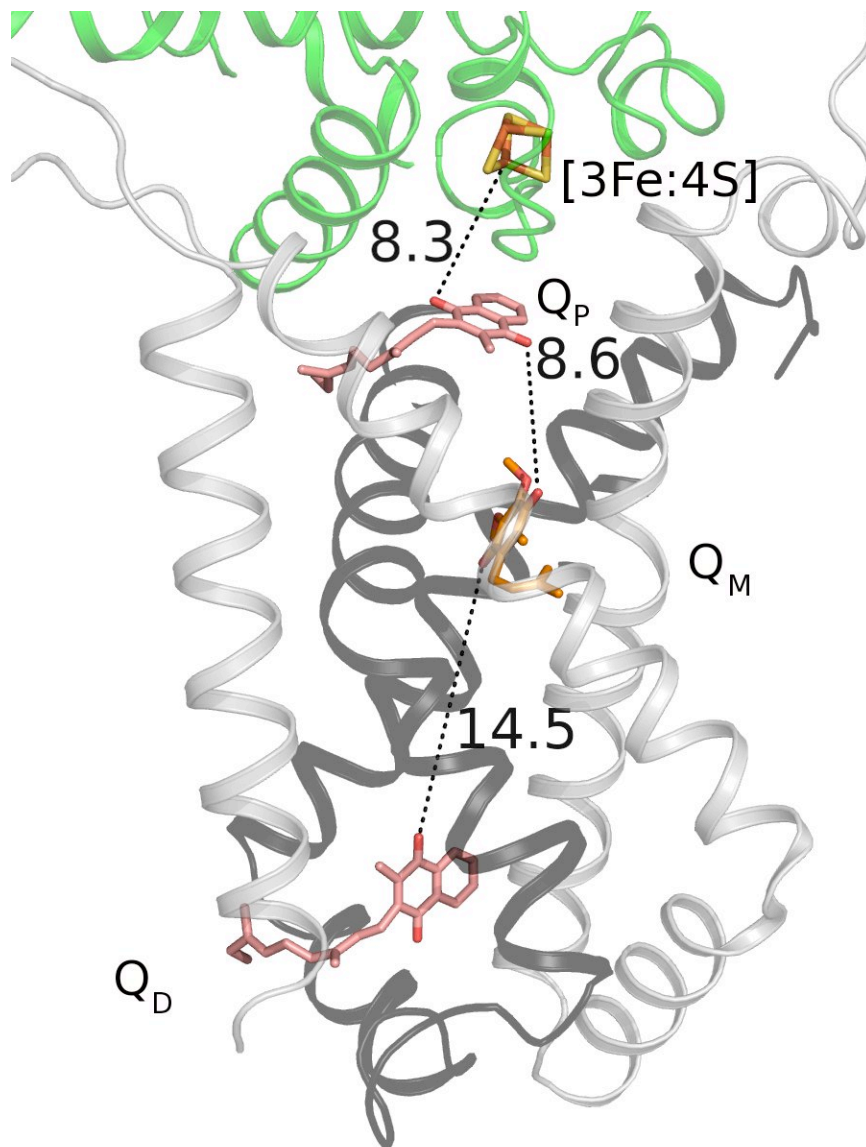
Figure 43. Relationship of the [3Fe:4S] iron-sulfur cluster, Q_P, Q_M, and Q_D sites to one another. The B subunit is colored green, C subunit is colored grey and the D subunit colored black. Oxygen atoms are colored red, nitrogen atoms are colored blue, iron colored brown, sulfur atoms colored tan, and carbon atoms are colored salmon for menaquinone bound to E29L QFR, and orange for ubiquinone.

The UQ-4 model makes several contacts in the highly polar pocket. These

include putative hydrogen bonds from O1 of UQ4 to the γ-hydroxyl of Ser D24 and
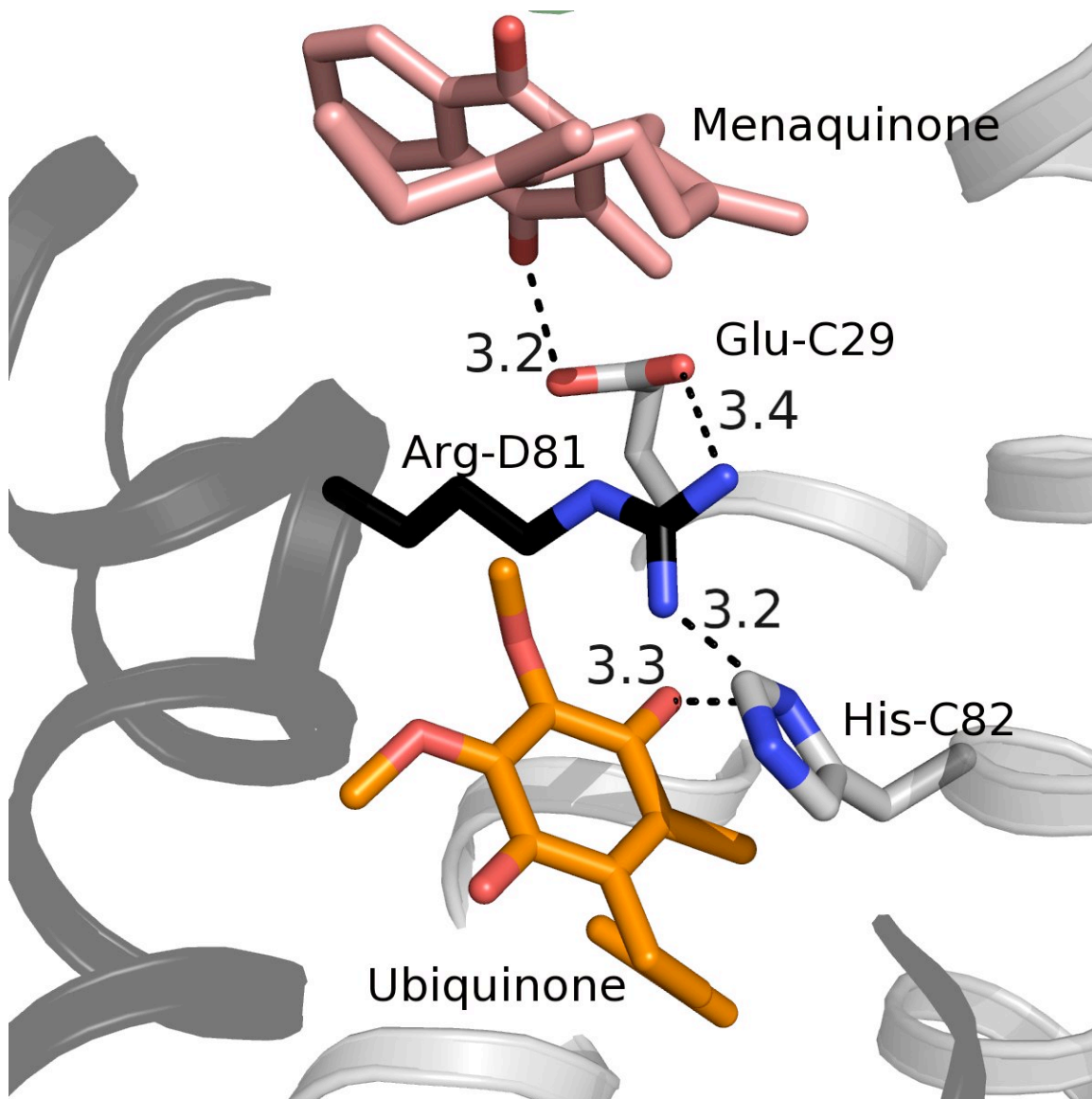
Figure 44. Hypothetical proton pathway between the Q_D and Q_M sites. The C subunit is colored grey and the D subunit colored black. Oxygen atoms are colored red, nitrogen atoms are colored blue, and carbon atoms are colored salmon for menaquinone bound to E29L QFR and orange for ubiquinone. The side chains are colored either grey or black for side chains depending on which subunit they correspond to. Dashes represent distances between atoms in angstroms.

From the O4 oxygen of UQ-4 to the γ-carbonyl of Thr-C31, the η1 of Arg-D81 and the Nδ1 of His-D82 (Fig. 41C). Interestingly, His-D82, when mutated, leads to decreased QFR reduction of ubiquinol, supporting a role for this residue in the

ubiquinol reduction mechanism (2) . A series of protonatable residues extends from the Q_M site to the Q_P, including His-D82, Arg-D81, and Glu-C29, suggesting a possible route for proton transfer between the two sites (Fig. 44). Numerous pathways for UQ entry into the Q_M site are possible, including entry from the Q_P site, entry from the Q_D site, or entry laterally from the membrane. The later seems unlikely, since it would require lateral movement of two helices. The most likely pathway is from the Q_P site, which would require the movement of Arg-D83. This hypothetical movement would make an internal cavity that then would provide a binding site for UQ.

HQNO binding is shifted slightly in the E29L QFR variant – The co-structure of HQNO with E29L shows a slight 0.9Å difference in position compared to HQNO in the wild-type enzyme. In the E29L QFR co-structure, HQNO moves towards Lys-B228 and away from Leu-C29, similar to the change observed in the comparison of menaquinone complexed with QFR E29L and wt. The ring of HQNO moves laterally sideways, with little change of distance to the iron sulfur cluster. The movement is consistent with that proposed and may be on-pathway to position the menasemiquinone into an additional binding pocket for catalysis.

Atpenin A5 binds in the Q_M site – The co-structure of E29L QFR and atpenin A5 reveals electron density in the Q_M region. Atpenin A5 makes similar putative hydrogen bonding contacts as UQ (Fig. 41D). Notably, there is a minor shift in the binding position of atpenin-A5, towards the Thr-C31 by 1.2Å.

Conclusions and Future Directions

The examined co-crystal structures of the QFR ligands with E29L QFR allowed for tentative assignments of the electron density. More work remains to positively confirm the location of these ligands. Future directions for this work include further refinement of the co-complexes, and mutation of residues along the Q_M pocket to test the effects of UQ-4 binding and turnover. Future work will aim to discover what the importance of menaquinone rearrangements is, the significance of the Q_M pocket, and what the proton pathway is to the Q_M site.

References

1.   Cecchini, G. (2003) *Annu. Rev. Biochem.* **72**, 77-109

2.   Westenberg, D. J., Gunsalus, R. P., Ackrell, B. A. C., Sices, H., and Cecchini, G. (1993) *J. Biol. Chem.* **268**, 815-822

3.   Iverson, T. M., Luna-Chavez, C., Cecchini, G., and Rees, D. C. (1999) *Science* **284**, 1961-1966

4.   Iverson, T. M., Luna-Chavez, C., Croal, L. R., Cecchini, G., and Rees, D. C. (2002) *J. Biol. Chem.* **277**, 16124-16130

5.   Hagerhall, C., Magnitsky, S., Sled, V. D., Schroder, I., Gunsalus, R. P., Cecchini, G., and Ohnishi, T. (1999) *J. Biol. Chem.* **274**, 26157-26164

6.   Miyadera, H., Shiomi, K., Ui, H., Yamaguchi, Y., Masuma, R., Tomoda, H., Miyoshi, H., Osanai, A., Kita, K., and Omura, S. (2003) *Proc. Natl. Acad. Sci. of the U.S.A.* **100**, 473-477

7.   Horsefield, R., Yankovskaya, V., Sexton, G., Whittingham, W., Shiomi, K., Omura, S., Byrne, B., Cecchini, G., and Iwata, S. (2006) *J. Biol. Chem.* **281**, 7309-7316

8.   Smirnova, I. A., Hagerhall, C., Konstantinov, A. A., and Hederstedt, L. (1995) *FEBS Lett.* **359**, 23-26

9.   Ruzicka, F. J., Beinert, H., Schepler, K. L., Dunham, W. R., and Sands, R. H. (1975) *Proc. Natl. Acad. Sci. of the U.S.A.* **72**, 2886-2890

10.   Luna-Chavez, C., Iverson, T. M., Rees, D. C., and Cecchini, G. (2000) Overexpression, purification, and crystallization of the membrane-bound fumarate reductase from Escherichia coli. In. *Protein Expression and Purification*

11.   Otwinowski, Z. (1993) *In CCP4 Study Weekend Data Collection and Processing; SERC Daresbury Labortatory, UK*

12.   Otwinowski, Z., and Minor, W. (1997) Processing of X-ray diffraction data collected in oscillation mode. In. *Macromolecular Crystallography, Pt A*, Academic Press Inc, San Diego

13.   Bailey, S. (1994) *Acta Crystallographica Section D-Biological Crystallography* **50**, 760-763

14.   Murshudov, G. N., Vagin, A. A., and Dodson, E. J. (1997) *Acta Crystallogr. Sect. D* **53**, 240-255

15. Cowtan, P. E. a. K. (2004) *Acta Crystallogr. Sect. D* **60**, 2126-2132

16. Adams, P. D., Grosse-Kunstleve, R. W., Hung, L. W., Ioerger, T. R., McCoy, A. J., Moriarty, N. W., Read, R. J., Sacchettini, J. C., Sauter, N. K., and Terwilliger, T. C. (2002) *Acta Crystallographica Section D-Biological Crystallography* **58**, 1948-1954

17. DeLano, W. L. (2002) *DeLano Scientific, San Carlos, CA, USA*

Acknowledgements

CHAPTER V

PURIFICATION OF A STABILIZED MENAQUINOL:FUMARATE

OXIDOREDUCTASE AND FLIG CO-COMPLEX

Introduction

Locomotive bacteria such as *Escherichia coli* can sense their external environments and respond by moving away or towards a stimulus. This is accomplished by modulation of the activity of the flagellar motor, a large megadalton complex with a tail-like appendage called a flagellum (1). External and internal signaling cues bias the direction of flagellar spin to either clockwise or counterclockwise. Counterclockwise rotation propels the bacterium forward while clockwise rotation results in a tumbling behavior, which leads to a random reorientation of the cell. Alternating series of "runs" and "tumbles" biased by signaling cues allow for a mechanism to control the overall direction of travel.

The direction of bacterial spin is controlled through the activity of the switch complex, a series of three proteins – FliG, FliM, and FliN – that, through an unknown mechanism, respond to a signal and switch direction of rotation. It has been proposed that this switching occurs through a conformational change in FliG, causing a synchronized alteration of the alignment of positively and negatively charged residues (2-4). Many of the signals biasing flagellar spin are sensed extracellularly, by receptors such as CheA (5). Upon activation, these receptors activate histidine kinase cascades, activating signaling proteins such as CheY (6).

For a number of years, the dicarboxylates fumarate and oxaloacetate have been understood to alter the rotation of the flagellar motor, biasing it towards clockwise rotation (7). The effect of fumarate binding on flagellar spin was discovered to be mediated by a direct interaction between quinol:fumarate reductase (QFR) and FliG (8). This signaling event was found to be separate from the activity of QFR in its bioenergetic capacity, and may be mediated directly by conformational changes that are thought to occur in QFR upon ligand binding (9).

To study the interaction between QFR and FliG, we have attempted to co-crystallize a complex between QFR and FliG. Initial attempts to obtain the QFR-FliG complex structure began with an attempt to identify conditions that would maximally stabilize the complex on size-exclusion chromatography. Following purification, numerous crystal conditions were screened.

Materials and Methods

Full length *E. coli* FliG in the pEWG1 vector (8) was grown from a starter culture for ~8hrs in 5ml LB with 0.1mg/ml ampicillan and 0.034 mg/ml chloramphenicol, which is used to inoculate 500ml LB overnight with appropriate antibiotics. The inoculum is then distributed among 6 1L flasks of LB media with an inoculum size of 50-80ml culture per 1 L LB with 0.1mg/ml ampicillan and 0.034 mg/ml chloramphenicol. The cells are grown at 37C° until the OD_{600} is ~0.5 (~2 hrs). The cells are then induced with 1mM IPTG and grown until the OD_{600} reaches ~2.0 (~2-3 hrs) and harvested by centrifugation at 5000g for 15 min.

Cells were lysed using sonication in lysis buffer containing 50mM NaH_2PO_4, 300mM NaCl, and 10mM imidazole + 3 inhibitor tablets/50ml buffer + DNase + RNase. The lysate was then cleared with an ultracentrifuge at 45000rpm in a Ti70 rotor for 40min at 4C°. Next, the supernatant is filtered and applied to Talon resin or to Ni Hitrap column. The lysate and resin mixture is incubated at 4C° for 45min while rotating. To isolate the protein, the resin is washed with 50-100 bed volumes of buffer A. FliG is then eluted with buffer B and immediately diluted into buffer A without imidazole and concentrated in a 10 kDa cutoff Amicon filter at 2500-3000g (Fig. 45).
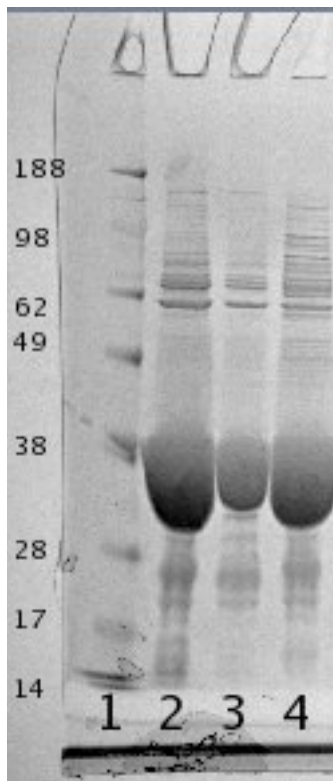

Figure 45. SDS-PAGE gel of purified FliG. Lane 1: Ladder. Lanes 2-4: successive elution of Ni^{2+} affinity resin.

To isolate the QFR/FliG complex, FliG is added to QFR (purified as in (10)) in a 1:9 molar ratio of QFR/FliG with 20mM tris pH 7.4, 0.02% do-decyl maltoside added to a total volume of 5ml. The mixture is then dialyzed against ~150 ml buffer D for 2-3 hrs. The QFR/FliG mixture is concentrated to ~500ul on a 50kDa cutoff Amicon filter and loaded on a superdex gel filtration column (Fig. 46).
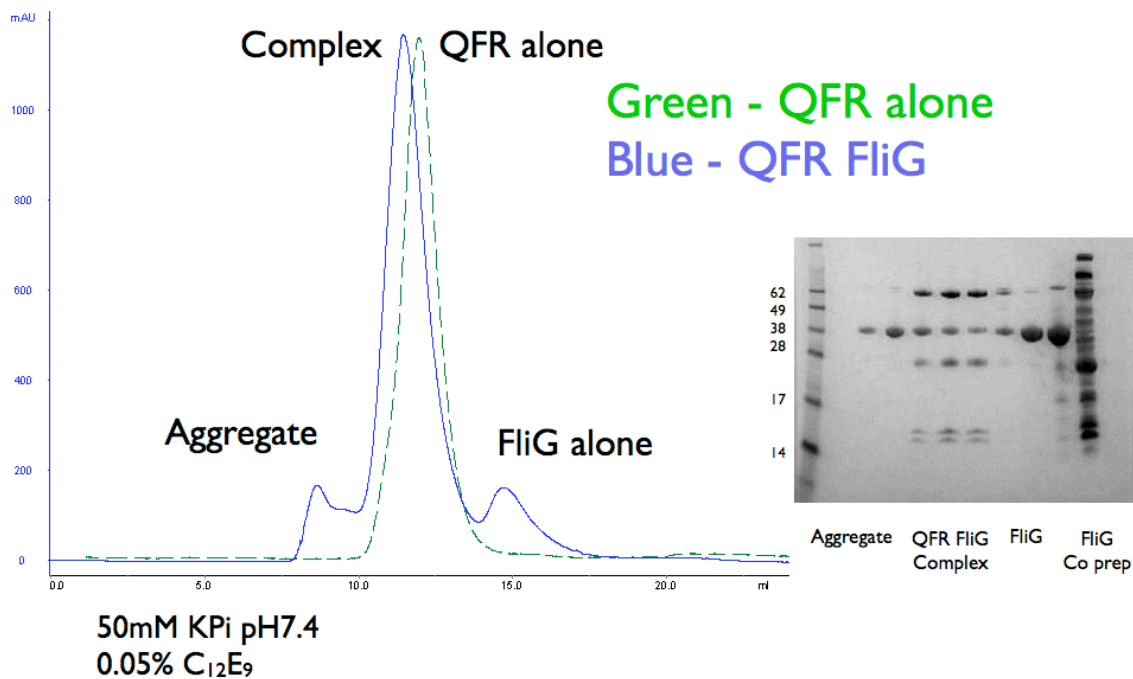

Figure 46. Gel filtration chromatogram of QFR/FliG run and corresponding SDS-PAGE gel.

Results and future directions

The QFR/FliG complex was applied to several crystallographic screens in 0.05% Thesit, 0.02% DDM, and 5mM DM. A total of ~3600 crystallization conditions were

167

tested. Initial attempts to purify and crystallize the complex resulted in crystals that diffracted to ~3.4 Å resolution (Fig. 47).
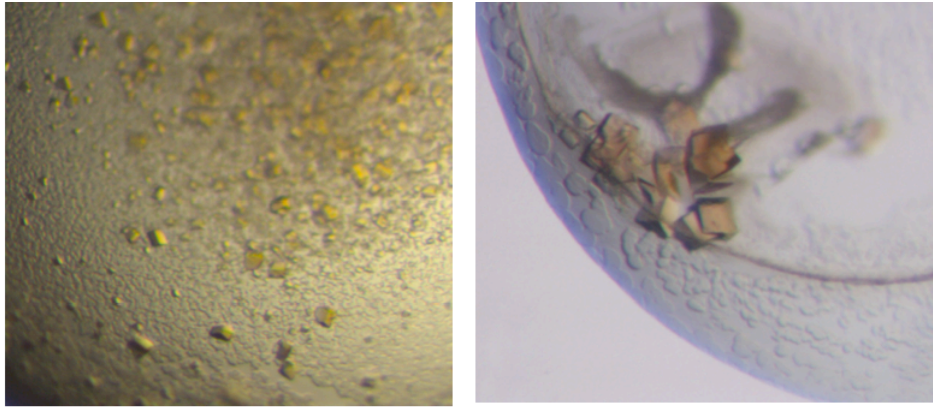
M36
-30% PEG 600
-200mM Mg(OAc)$_2$
- 50mM HEPES pH 7.5

Index 54
-15% PEG MME 550
-25mM CaCl$_2$
- 50mM Bis-Tris pH 6.5

Figure 47. Preliminary crystals obtained from QFR/FliG mixture.

However, although QFR was identified in the crystallographic electron density, FliG was unable to be located. Attempts to verify the incorporation of FliG into the crystals with mass spectrometry were unsuccessful. Size exclusion chromatography to verify the stability of the QFR/FliG complex showed that the complex started to break down ~1hr after formation. (Fig. 48). Further attempts were made to determine the optimal purification conditions for both FliG alone and in complex with QFR when isolated with size-exclusion chromatography (Table 8). Though it was difficult to obtain a quantitative measure of stability, high pH, dicarboxylate additives, and
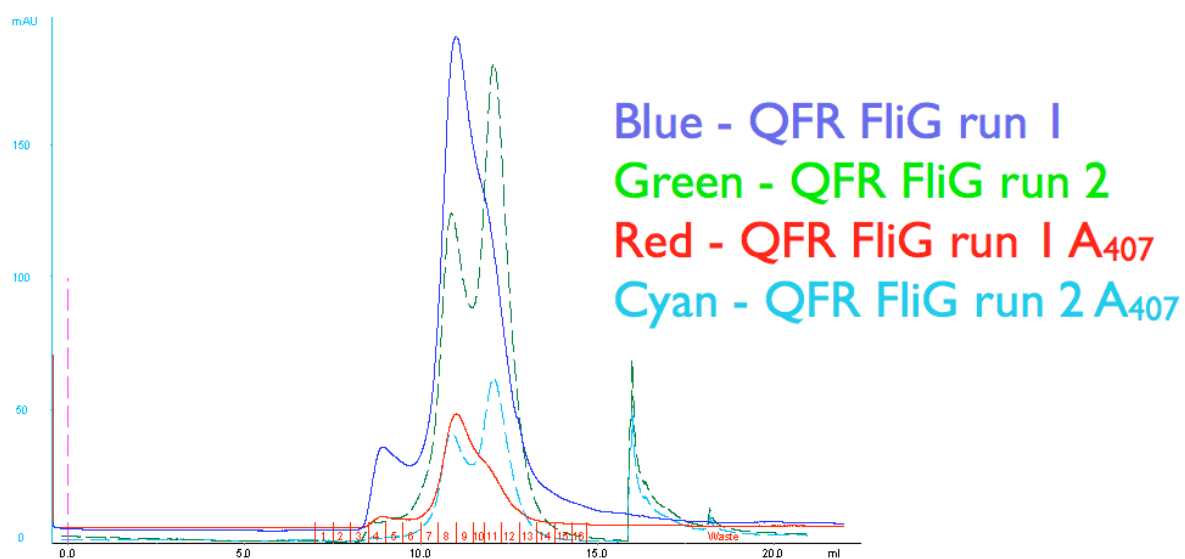
Figure 48. Size exclusion chromatograms of QFR/FliG complex immediately after dialysis (run 1) and of run 1 reapplied to the gel-filtration column (run 2). A_{407} measures the absorbance from the covalently linked FAD cofactor.

Buffer	Detergent	Additive	FliG alone	QFR/FliG complex
20mM Tris pH 7.4	0.05% Thesit	-	Unstable	Stable
20mM Tris pH 7.4	0.02% DDM	-	-	Stable
20mM Tris pH 7.4	5mM DM	-	-	Stable
20mM Bis-Tris pH 6.0	0.02% DDM	-	-	Unstable
20mM Tris pH 9.0	0.02% DDM	-	-	Stable
20mM KPi pH 7.4	0.02% DDM	-	Unstable	Stable
20mM Tris pH 7.4	0.02% DDM	100mM NaCl	Stable	Stable
20mM Tris pH 7.4	0.02% DDM	300mM NaCl	Stable	Stable
20mM Tris pH 7.4	0.02% DDM	10mM MgSO$_4$	-	Stable *
20mM Tris pH 7.4	0.02% DDM	10mM Oxaloacetate	-	Stable *
20mM Tris pH 7.4	0.02% DDM	10mM fumarate	-	Stable

Table 8. Assessment of FliG or FliG/QFR stability with gel-filtration chromatography. DDM=B-Dodecyl maltoside DM=Decyl maltoside KPi = potassium phosphate *= especially stable condition

169

MgSO$_4$ seemed to stabilize the complex. QFR addition to FliG seemed to greatly stabilize FliG in solution.

Conclusions

Since the stability of QFR alone has been well characterized, new conditions to stabilize both FliG alone and FliG bound to QFR have been sought. The complex was seemingly formed and stabilized equally well with all the detergents tested and buffers tested, except for Bis-Tris pH 6.0 (Table 8). The keys for stability seem to be ultracentrifugation of the lysate (the lack of which resulted in extremely dirty preps – data not shown), removal of imidazole, dialysis, and saturation of QFR with FliG. Future work has been planned to try a multifaceted approach to stabilize the QFR/FliG complex, including screening with a virial coefficient stability screen (11), using lipid bicelles (12), and attempting crystallization with shortened or mutant FliG constructs (3,4,13).

References

1. Berg, H. C. (2003) *Annu. Rev. Biochem.* **72**, 19-54

2. Lee, L. K., Ginsburg, M. A., Crovace, C., Donohoe, M., and Stock, D. (2010) *Nature* **466**, 996-U129

3. Lloyd, S. A., Whitby, F. G., Blair, D. F., and Hill, C. P. (1999) *Nature* **400**, 472-475

4. Brown, P. N., Hill, C. P., and Blair, D. F. (2002) *Embo J.* **21**, 3225-3234

5. Hess, J. F., Oosawa, K., Kaplan, N., and Simon, M. I. (1988) *Cell* **53**, 79-87

6.   Hess, J. F., Bourret, R. B., and Simon, M. I. (1988) *Nature* **336**, 139-143

7.   Marwan, W., Schafer, W., and Oesterhelt, D. (1990) *Embo J.* **9**, 355-362

8.   Cohen-Ben-Lulu, G. N., Francis, N. R., Shimoni, E., Noy, D., Davidov, Y., Prasad, K., Sagi, Y., Cecchini, G., Johnstone, R. M., and Eisenbach, M. (2008) *Embo J.* **27**, 1134-1144

9.   Tomasiak, T. M., Maklashina, E., Cecchini, G., and Iverson, T. M. (2008) *J. Biol. Chem.* **283**, 15460-15468

10.   Luna-Chavez, C., Iverson, T. M., Rees, D. C., and Cecchini, G. (2000) Overexpression, purification, and crystallization of the membrane-bound fumarate reductase from Escherichia coli. In. *Protein Expression and Purification*

11.   Gabrielsen, M., Nagy, L. A., DeLucas, L. J., and Cogdell, R. J. (2010) *Acta Crystallogr. Sect. D-Biol. Crystallogr.* **66**, 44-50

12.   Sanders, C. R., and Prosser, R. S. (1998) *Struct. Fold. Des.* **6**, 1227-1234

13.   Van Way, S. M., Millas, S. G., Lee, A. H., and Manson, M. D. (2004) *J. Bacteriol.* **186**, 3173-3181

CHAPTER VI

SUMMARY AND SYNOPSIS

Summary

The development of methods to probe integral membrane protein structure (1) has allowed the chemical probing of function of many key enzymes. The initial structures of the respiratory complexes (2-7) provided a foundation to ask detailed mechanistic questions of how these key enzymes function and provide answers satisfying on a physical chemical level, helping to bridge the study of membrane protein biology with the realm of chemistry. With the initial QFR (2,8), SQR (9), and eukaryotic complex II structures (10,11) in hand, the opportunity arose to learn crucial details about flavin chemistry, electron transfer, quinol interconversion, reactive oxygen species formation, and toxin inhibition. It is difficult to overstate the value of these questions, since they can lead to insight into such diverse processes as tumor formation (12), neurotoxicity (13), and aging (14) – all areas where alterations of complex II function has been shown to contribute. The work presented in this dissertation adds to the body of knowledge concerning complex II function in general and *Escherichia coli* QFR function in particular by examining four distinct areas: dicarboxylate catalysis, inhibition and off-pathway catalysis, quinone interconversion, and signaling.

In chapter one of this work, we investigated the relevance of an active site loop for formation of the fumarate to succinate transition state (15). Fumarate

172

hydrogenation presents a challenge for QFR due to the relative kinetic stability of hydride transfer owing to the small size of fumarate and succinate. To overcome this challenge, the QFR dicarboxylate active site stabilizes fumarate in a torsioned, partially charged conformation (8,16). Chapter one presents evidence that this conformation comes about in part due to the concerted activity of two threonine residues, Thr-A234 and Thr-A244. Thr-A234 interacts with the active site proton shuttle, altering its pKa and possibly linking its protonation state to the conformational state of the dicarboxylate active site. Difference absorbance spectroscopy showed that a Thr-A234 mutation to alanine abrogated proper positioning of ligand, which corroborated loss of enzyme activity and which was recapitulated with a shift of solution pH. Mutation of Thr-A244 to alanine similarly resulted in a loss of activity; however, this was the first mutation to result in a decrease of the second order rate constant (k_{cat}/K_M). This was rationalized by the position of Thr-A244, which donates a hydrogen bond to fumarate in a position ideal for attainment of the stabilized, twisted intermediate. Taken together, these two mutations allowed the proposal of a model where domain movements torsion the substrate upon binding to 1) facilitate attainment of the transition state and 2) to act as a control mechanism that only brings in necessary catalytic residues for catalysis upon formation of a fully closed and aligned active site.

The second chapter further investigated the result of the twisting mechanism on the ligand and its potential implication for inhibition and side-product formation. A trend was observed between structures of non-activatable and activatable QFR ligands. Those ligands that were potential targets of a QFR reaction, such as

173

fumarate or oxaloacetate, all were torsioned in such a way that an activatable bond was aligned almost exactly parallel with the C(4a)-N5 bond of FAD. Those that were not activated, the inhibitors glutarate and oxaloacetate, lacked this positioning, probably due their inherent geometry. The activatable ligands further shared the characteristic of an electronic interaction with FAD that shifts its optical properties, while the non-activated ligands did not. We proposed that this was possibly due to an orbital-steering mechanism, where two frontier orbitals have to be positioned almost exactly to maximize their overlap. The orbital-steering theory holds that enzymes are evolutionarily tuned to maximize HOMO-LUMO overlap and that slight structural perturbations can have dramatic effects on enzyme activity (20,21). It was proposed that the orbital steering mechanism may also contribute to formation of a covalent adduct with 3-nitropropionate, and optical spectroscopy and mass spectrometry were used to propose a suicide inactivation mechanism. The reaction is, as far as is evident, unique in nature and adds another dimension to arginine chemistry.

The third chapter examined the activity of an entirely distinct active site, the quinol interconversion site. Here, we examined the structural details of interaction between a mutant, QFR FrdC E29L, with the substrates menaquinone and ubiquinone as well as the inhibitors heptyl quinoline n-oxide (HQNO) and atpenin A5. The FrdC E29L mutation was shown with EPR to stabilize a semiquinone radical intermediate of menaquinone in the active site (17). Although the structures are still preliminary, a very cautious initial interpretation revealed a number of interesting features. First, menaquinone and its analog, HQNO, bind in slightly altered positions

form those seen in the wild-type co-structures (2,18). The altered binding may reveal a reaction mechanism were menaquinol binds two or more conformations *en route* to menaquinone formation. Investigation of ubiquinone binding revealed the unexpected increase of electron density in a region called the Q_M region, as did the ubiquinone analog atpenin A5. In the Q_M site, the preliminarily modeled ubiquinone would make multiple stabilizing interactions, as well as interactions with possible catalytic residues that could be linked by a proton shuttle to the Q_P site. Although this is highly speculative, it would be interesting to test the possibility of linked menaquinone and ubiquinone catalysis. A great deal of work remains to be done to refine the co-structures, to verify the ligand positions, and to mutate residues possibly important to catalysis. This will help clarify the significance of the menaquinone rearrangement, the validity of the Q_M ubiquinone site, and any physiological relevance of the interplay between the Q_M and Q_P sites.

Finally, very preliminary work was undertaken to study the role of QFR not in its bioenergetic capacity, but instead as a signaling molecule. Previous work has shown that QFR can directly mediate changes in the direction of flagellar spin upon fumarate binding through a direct interaction with the flagellar protein FliG (19). To investigate the structural rearrangements that might underlie this signaling, especially given that enzyme dynamics may be important for fumarate catalysis, the stabilization and crystallization of the QFR/FliG complex was performed. Initial success with purification of a 1:1 QFR/FliG complex led to a series of crystallization attempts. Upon screening ~3600 crystallization conditions, two crystallization conditions were found, one of which yielded diffraction quality crystals. Despite

obtainment of a quality dataset, a molecular replacement solution with FliG was elusive. Attempts with mass-spectrometry to reveal the nature of the crystals were inconclusive, due to the small size of the crystals. Further characterization revealed that, although the QFR/FliG complex can be formed, it is unstable. Further work will focus on stabilizing FliG alone, then FliG with QFR.

In these studies, the capacity of QFR to perform multiple tasks was explored. In all, the structural details of catalysis of five types of chemical reactions were investigated at two known and one possible active sites. Additionally, preliminary work was performed to study the role of QFR not as an enzyme but as a receptor. Taken together, this speaks to the remarkable flexibility and utility of this evolutionarily ancient class of enzymes.

References

1.   Deisenhofer, J., Epp, O., Miki, K., Huber, R., and Michel, H. (1985) *Nature* **318**, 618-624

2.   Iverson, T. M., Luna-Chavez, C., Cecchini, G., and Rees, D. C. (1999) *Science* **284**, 1961-1966

3.   Abrahams, J. P., Leslie, A. G. W., Lutter, R., and Walker, J. E. (1994) *Nature* **370**, 621-628

4.   Xia, D., Yu, C. A., Kim, H., Xian, J. Z., Kachurin, A. M., Zhang, L., Yu, L., and Deisenhofer, J. (1997) *Science* **277**, 60-66

5.   Iwata, S., Ostermeier, C., Ludwig, B., and Michel, H. (1995) *Nature* **376**, 660-669

6.   Sazanov, L. A., Efremov, R. G., Baradaran, R., and Berrisford, J. M. *Biochimica Et Biophysica Acta-Bioenergetics* **1797**, 10-10

7.   Hunte, C., Zickermann, V., and Brandt, U. *Science* **329**(5990), 448-451

8.   Lancaster, C. R. D., Kroger, A., Auer, M., and Michel, H. (1999) *Nature* **402**, 377-385

9.   Yankovskaya, V., Horsefield, R., Tornroth, S., Luna-Chavez, C., Miyoshi, H., Leger, C., Byrne, B., Cecchini, G., and Iwata, S. (2003) *Science* **299**, 700-704

10.   Huang, L. S., Sun, G., Cobessi, D., Wang, A. C., Shen, J. T., Tung, E. Y., Anderson, V. E., and Berry, E. A. (2006) *J. Biol. Chem.* **281**, 5965-5972

11.   Sun, F., Huo, X., Zhai, Y. J., Wang, A. J., Xu, J. X., Su, D., Bartlam, M., and Rao, Z. H. (2005) *Cell* **121**, 1043-1057

12.   Baysal, B. E., Ferrell, R. E., Willett-Brozick, J. E., Lawrence, E. C., Myssiorek, D., Bosch, A., van der Mey, A., Taschner, P. E. M., Rubinstein, W. S., Myers, E. N., Richard, C. W., Cornelisse, C. J., Devilee, P., and Devlin, B. (2000) *Science* **287**, 848-851

13.   Beal, M. F., Brouillet, E., Jenkins, B. G., Ferrante, R. J., Kowall, N. W., Miller, J. M., Storey, E., Srivastava, R., Rosen, B. R., and Hyman, B. T. (1993) *J. Neurosci.* **13**, 4181-4192

14.   Ishii, N., Fujii, M., Hartman, P. S., Tsuda, M., Yasuda, K., Senoo-Matsuda, N., Yanase, S., Ayusawa, D., and Suzuki, K. (1998) *Nature* **394**, 694-697

15. Tomasiak, T. M., Maklashina, E., Cecchini, G., and Iverson, T. M. (2008) *J. Biol. Chem.* **283**, 15460-15468

16. Leys, D., Tsapin, A. S., Nealson, K. H., Meyer, T. E., Cusanovich, M. A., and Van Beeumen, J. J. (1999) *Nat. Struct. Biol.* **6**, 1113-1117

17. Hagerhall, C., Magnitsky, S., Sled, V. D., Schroder, I., Gunsalus, R. P., Cecchini, G., and Ohnishi, T. (1999) *J. Biol. Chem* **274**, 26157-26164

18. Iverson, T. M., Luna-Chavez, C., Croal, L. R., Cecchini, G., and Rees, D. C. (2002) *J. Biol. Chem.* **277**, 16124-16130

19. Cohen-Ben-Lulu, G. N., Francis, N. R., Shimoni, E., Noy, D., Davidov, Y., Prasad, K., Sagi, Y., Cecchini, G., Johnstone, R. M., and Eisenbach, M. (2008) *Embo J.* **27**, 1134-1144

20. Dafforn, A., and Koshland, D. E. (1971) *Proc. Natl. Acad. Sci. U.S.A* **68**, 2463-2467

21. Mesecar, A. D., Stoddard, B. L., and Koshland, D. E. (1997) *Science* **277**, 202-206